Aalto University
School of Engineering
Degree Programme in Mechanical Engineering

Martin Porkholm

Structural Response in Arc Flash Event

Master's Thesis
Espoo, October 19, 2015

Supervisor: Professor Jukka Tuhkuri, Aalto University
Advisors: Pirkka Myllykoski Ph.D. (Tech.)
Jorma Manninen M.Sc. (Tech.)

Aalto University
School of Engineering

Aalto University, P.O. BOX 11000, 00076
AALTO
www.aalto.fi

Abstract of master's thesis

Author Martin Porkholm		
Title of thesis Structural Response in Arc Flash Event		
Degree programme Degree Programme in Mechanical Engineering		
Major/minor Mechanics of Materials/Fluid Mechanics		**Code** K3006
Thesis supervisor Prof. Jukka Tuhkuri		
Thesis advisor(s) Ph.D. Pirkka Myllykoski/M.Sc. Jorma Manninen		
Date 19.10.2015	**Number of pages** 80	**Language** English

Abstract

Hazardous arc flash events generally occur in high-voltage electrical equipment due to malfunctioning apparatus or human error. Although considerable effort has been put into describing the physics of arc generation and the resulting blast load, analysis of the structural response has only received little attention despite its apparent importance. Personnel injury or death are likely if the enclosure fails to contain the unintentional blast appropriately.

Developing the correct approach for analyzing the structural response is of high interest to the electric industry, and should be considered the main motivation behind this study. In the future, expensive arc flash tests currently used to assess the safety of designs are hopefully replaced by extensively validated and verified simulation tools.

The results from a thorough literary review are first presented to give the reader insight into the current state of knowledge. Two approaches customarily used to estimate the resulting blast load are next described along with the energy balance of an arc flash event. Principles governing the structural response are then introduced. The violent nature of the arc flash event suggests that the strain rate dependency of the material might play an important role. The Cowper-Symonds and Huh-Kang models attempting to capture the behaviour are described and extensively compared in typical arc flash conditions.

The stochastic nature of the phenomenon implies that the arc power can often only be determined via probabilities. Although scarcely investigated in the literature, this thesis attempts to address the issue by introducing a stochastic dimensioning principle for the structure.

In order to gain confidence in the methods, numerical predictions are compared to measured deformations obtained from an arc flash test. The implications of adapting the stochastic dimensioning principle to the enclosure are then investigated. Conclusions and future recommendations are finally presented.

Keywords arc, flash, blast, Cowper-Symonds, Huh-Kang, FEM, CFD, stochastic

Aalto-yliopisto
Insinööritieteiden
korkeakoulu

Aalto-yliopisto, PL 11000, 00076
AALTO
www.aalto.fi

Diplomityön tiivistelmä

Tekijä Martin Porkholm		
Työn nimi Rakenteen Vaste Valokaarioikosulussa		
Koulutusohjelma Konetekniikan koulutusohjelma		
Pää-/sivuaine Lujuusoppi/Virtausmekaniikka		**Koodi** K3006
Työn valvoja Prof. Jukka Tuhkuri		
Työn ohjaaja(t) TkT Pirkka Myllykoski/DI Jorma Manninen		
Päivämäärä 19.10.2015	**Sivumäärä** 80	**Kieli** Englanti

Tiivistelmä

Vaaralliset valokaarivälähdykset voivat syttyä korkeajännitteisissä sähkölaitteissa toimintahäiriön tai inhimmillisen erehyksen vuoksi. Huomattavia ponnistuksia on tehty valokaaren fysiikan kuvaamiseen, sekä syntvän paineaallon mallintamiseen. Rakenteen vasteen oikeaoppinen analysointi on tästä huolimatta kerännyt vain niukasti huomiota alan kirjallisuudessa. Henkilöturvallisuuden varmentaminen ulkoisen rakenteen oikeaoppisella suunnittelulla on kuitenkin välttämätöntä vakavan loukkaantumisriskin takia.

Rakenteen vasteen analysointi on sähköteollisuuden kiinnostuksen kohteena, ja suurin syy tämän työn syntyyn. Tulevaisuudessa kalliit valokaarikokeet pystytään toivon mukaan korvaamaan laajasti varmennetuilla simulointityökaluilla.

Työn alussa esitetään kattavan kirjallisuuskatsauksen keskeisimmät tulokset, jonka jälkeen valokaaren energiatase havainnollistetaan. Kaksi yleisesti käytettyä menetelmää paineaallon mallintamiseen kuvataan lopuksi. Tämän jälkeen keskeisimmät periaateet rakenteen vasteen laskennassa esitetään lukijalle. Valokaaren raju olemus antaa vihiä siitä, että materiaalin venymänopeus on otettava huomioon. Cowper-Symonds ja Huh-Kang venymänopeusmallit esitetään tämän johdosta perusteellisesti, ja mallien ennustuksia vertaillaan tyypillisissä valokaarivälähdyksissä.

Valokaaren epämääräinen olemus johtaa yleisessä oikosulkutapahtumassa siihen, että valokaaren teho voidaan ainoastaan määritellä matemaattisiin todennököisyyksiin perustuen. Joskin kirjallisuudessa aihetta ollaan käsitelty vain niukasti, pyrkii tämä työ edistämään ajattelutapaa esittelemällä stokastisen mitoitusperiaatteen rakenteelle.

Työn lopussa valokaarikokeessa käytetyn kotelon mitattuja muodonmuutoksia verrataan laskennallisiin arvoihin, laskentamenetelmän toimivuuden todentamiseksi. Stokastisen mitoitusoperiaatteen käyttö esimerkkitapauksessa esitetään, jonka jälkeen työn tärkeimmät johtopäätökset sekä suositukset esitetään lukijalle.

Avainsanat valokaari, välähdys, paineaalto, Cowper-Symonds, Huh-Kang, FEM, CFD, stokastinen

Aalto-universitetet
Högskolan för
ingenjörsvetenskaper

Aalto-universitetet, PB 11000, 00076 AALTO
www.aalto.fi

Sammandrag av diplomarbetet

Författare Martin Porkholm		
Titel Strukturell Reaktion i Ljusbågskortslutning		
Utbildningsprogram Utbildningsprogrammet för Maskinteknik		
Huvud-/biämne Hållfasthetslära/Flödesmekanik		**Kod** K3006
Övervakare Prof Jukka Tuhkuri		
Handledare TkD Pirkka Myllykoski/DI Jorma Manninen		
Datum 19.10.2015	**Sidantal** 80	**Språk** Engelska

Sammandrag

Farliga ljusbågskortslutningar kan uppkomma i högspänningsapparater på grund av tekniska fel eller mänskliga misstag. Även om stora akademiska insatser har satts för att beskriva fysiken bakom ljusbågen och den uppkommande tryckvågen, har den strukturella reaktionen endast fått lite uppmärksamhet. En korrekt dimensionering av den yttre strukturen måste anses viktig, eftersom risken för kroppsskador är stor.

En korrekt analyseringsmetod av den strukturella reaktionen är av stort intresse till den elektriska industrin, och den största motivationen till att detta arbetet har gjorts. I framtiden kan dyra ljusbågstest hoppeligen ersättas med trovärdiga simuleringsmetoder.

Resultaten av en omfattande litteraturöversikt presenteras först. Energibalansen av en ljusbågskortslutning presenteras sedan. De två vanligaste metoderna för att uppskatta den resulterande tryckvågen presenteras till näst. Grundläggande principerna bakom den strukturella reaktionen redogörs för läsaren. Ljusbågens våldsamma natur innebär att materialets uttöjningshastighet har en inverkan på resultaten. Cowper-Symonds och Huh-Kang modellerna presenteras därmed och jämförs i typiska ljusbågskortslutningar.

Ljusbågens stokastiska natur innebär att energimängden som frigörs under kortslutningen endast kan bestämmas med hjälp av sannolikheter. Även om företeelsen inte har fått mycket uppmärksamhet bland forskare, försöker detta arbete befrämja tankesättet genom att presentera en stokastisk dimensioneringsprincip för strukturen.

De resulterande deformationerna mätta från en struktur som använts i ett ljusbågsexperiment jämförs med simuleringar, för att påvisa metodens trovärdighet. Implikationerna av den stokastiska dimensioneringsprincipen presenteras sedan. Till slut redogörs arbetets viktigaste slutsatser för läsaren.

Nyckelord ljusbåge, tryckvåg, Cowper-Symonds, Huh-Kang, FEM, CFD, stokastisk

Acknowledgements

First and foremost I wish to thank Dr Jörg Ostrowski, Dr Pirkka Myllykoski, Mr Jorma Manninen, Mr Risto Laurila and Mr Ismo Talka for providing me with direction and support. Without their help this work would have been inadequate.

From the university I wish to thank Dr Kari Santaoja and Professor Jukka Tuhkuri, who have given me important insights during the years of study and this thesis.

Without the motivation from my parents and sister this work I would probably never have been completed. For that I am forever in debt. I also wish to express my gratitude to Oliver Lundqvist, who has supported me during this project and our years at the university. It has truly been a fruitful journey.

Finally, thank you Henrika, for keeping me sane.

Espoo, August 15, 2015

Martin Porkholm

Table of Contents

Symbols

C	Cowper-Symonds strain rate model material parameter
C_1	Huh-Kang strain rate model material parameter
C_2	Huh-Kang strain rate model material parameter
P	Cowper-Symonds strain rate model material parameter
P_{el}	Arc power
S_{E}	Heat source term
S_{M}	Mass source term
W_{chem}	Energy describing chemical reactions in an arcing event
$W_{\mathrm{e,a}}$ / $W_{\mathrm{e,c}}$	Energy absorbed by the electrodes in an arcing event
W_{el}	Energy released by the arc
W_{mv}	Energy describing the melting and vaporization of electrodes
W_{rad}	Energy describing radiation losses from the arc
W_{therm}	Energy transferred to the surrounding gas from the arc

c_{p}	Specific heat capacity of fluid at constant pressure
c_{v}	Specific heat capacity of fluid at constant volume
h	Specific fluid enthalpy
k_{p}	Thermal transfer coefficient
u	Specific internal energy of fluid

$\boldsymbol{C}$	Damping matrix
$\boldsymbol{K}^{\mathrm{Ta}}(\boldsymbol{u})$	Tangential stiffness matrix
$\boldsymbol{M}$	Mass matrix
$\boldsymbol{S}_{\mathrm{F}}$	Momentum source term

$\boldsymbol{F}^{\mathrm{i}}$	Stiffness vector
$\boldsymbol{F}^{\mathrm{a}}$	Load vector
$\boldsymbol{v}$	Fluid velocity vector
$\boldsymbol{u}$	Structural displacement vector
$\dot{\boldsymbol{u}}$	Structural velocity vector
$\ddot{\boldsymbol{u}}$	Structural acceleration vector

α	Discharge coefficient
α_{R}	Rayleigh mass-proportional damping coefficient
β_{R}	Rayleigh stiffness-proportional damping coefficient
ε_{f}	Fracture strain
$\bar{\varepsilon}_{\mathrm{p}}$	Equivalent plastic strain
κ	Adiabatic coefficient of the enclosure gas
ζ_{i}	i:th damping ratio
ρ	Fluid density
σ_{VM}	Von Mises stress
σ_{yield}	Quasi-static yield stress
$\dot{\sigma}_{\mathrm{yield}}$	Dynamic yield stress

1 Introduction

The first chapter serves as an introduction to the problem at hand, and establishes the research question which this thesis tries to answer. Results of a thorough literature review are presented to give the reader insight into the most notable discoveries made so far.

1.1 Problem description

Internal arc flash events generally occur as the result of malfunctioning apparatus or human error in high-voltage electrical equipment. The rapid discharge of electric potential forms an undesired arc, which transfers heat to the surroundings and causes the gas inside the enclosure to expand. The rapidly expanding gas puts the structure under tremendous stress. (Anantavanich 2010, p. 1) Personnel injury and death are likely if the structure fails to contain the blast. The most well-known arc flash accident occurred in Atlanta in 1989, when a fumbling electrician caused an electric arc to form in a cabinet. The resulting blast and fire caused five fatalities. (Babrauskas 2010) Reliable tools for predicting cabinet response in arc flash events are therefore of great interest to the industry sector. Figure 1 shows the resulting deformations of a cabinet after an arc flash event.

Figure 1. Resulting deformations after an arc flash event (Uzelac et al. 2010, p. 76).

The arc event frequency in high-voltage electrical equipment is fortunately low. According to Franz (2005) only one switchgear per 10 000 experiences an arc fault every year. Although failure is rare, increasingly demanding safety regulations require manufacturers to prove the safe operation of their products in adverse conditions. From a business perspective, a convincingly designed product adds to the customer value proposition. In a highly competitive world this can potentially be the determining factor when several companies fight for market share.

1.2 Goal and motivation behind thesis

The aim of this thesis is to create a sensible methodology for analyzing the structural response in an arc flash event. The work is motivated by requirements of the high power electric industry. No in-depth study on the matter was found in the literature. A thorough understanding of how cabinets and enclosures react in arcing events is ultimately reflected in safer products, with added value for customers.

Experimental arc flash tests are expensive and time-consuming to conduct, hence tests are ideally passed without repetition. A failed test could also delay the time to market of a product significantly, thus lowering a possible competitive edge of the manufacturer. The only realistic way to reduce experimental arc tests is to develop a reliable simulation methodology, which is capable of addressing possible concerns beforehand.

Estimating the energy released by the arc is difficult due to uncertainty in the arc length and –voltage. Secondary and tertiary arcs are often found to ignite in the wake of the initial flash event. The process is inherently stochastic, and estimating the effects on the pressure rise is difficult. One can certainly question the validity of results obtained from a single arc flash safety rating test. Repeating the experiment might have a completely different outcome. The random nature of the phenomenon is ultimately reflected as uncertainty in the structural response. Embracing, and addressing the uncertainty correctly is vital and one of the focal points in this thesis.

Computational tools for estimating the system response in arc flash scenarios are most useful if they are deeply imbedded in the product development methodology of a company. Designs are then swiftly updated as simulation results shed light on arc flash overpressures. This level of simulation integration is called concept verification according to Adams (2008). It is reasonable to require that a simulation tool embedded on that level yields results with acceptable computational effort. A tool which unreasonably heavy to use, will most likely only be used as a design verification tool. The implication being that computational simulations are not done until last minute, if at all. Correcting designs is then impractical and costly. Determining an approach which works both on paper and in practice should be considered one important research question of this thesis, albeit not of pure scientific nature.

The underlying uncertainty motivated the comparison of two approaches when estimating the resulting pressure load. The first approach describes the pressure load with less precision as the effects of pressure waves are neglected. On the other hand, the approach requires little computational effort which makes it feasible to implement statistical tools to combat the uncertainty. The second approach is capable of predicting the effects of pressure waves, and should therefore be considered more accurate. Substantial computational and modelling time is required, however, which makes the implementation of statistical tools unrealistic.

In the future, expensive arc flash tests are perhaps no longer needed. Instead, a credible and extensively validated simulation methodology might be sufficient to convince authorities and customers. This thesis should be seen as laying a part of the foundation for the ultimate goal.

1.3 Previous research

A great deal of research has been conducted on the subject of arc flashes. Scientific papers on the matter have focused almost entirely on describing the physics behind arc generation and the corresponding pressure rise, however. For a comprehensive and systematic review of the most important findings, the reader is encouraged to familiarize with Babrauskas (2010) work.

Only some researchers have published work regarding the structural response. Singh and Summer (2011) performed a simplified structural analysis, but failed to compare their results with measurements. Uzelac et al. (2011, p. 83) managed to predict the resulting deformations of an enclosure used in an arc flash test with great accuracy, although the results should be criticized as several aspects shown in this thesis to be of importance were neglected. The conducted structural analyses should therefore be considered superficial and lacking in many respects. Attempts at addressing the issue of uncertainty have not been made previously to the best knowledge of the author.

The first attempts at describing the pressure loading were motivated by real life accidents. Drouet and Nadeau (1979) tried to find an empirical relation behind the pressure variation and the arcing current, after a wall collapsed due to an arcing fault. The results were not applicable to arbitrary setups, however. Lee (1987) presented one of the first summaries on the matter, and gave some recommendations for improving the safety of personnel working in the vicinity of switchgears.

The first theoretical overpressure predictions were based on the ideal gas law and the energy conservation equation. The method produced the averaged pressure rise in the fluid volume as a function of time, and was later extended to compartments with openings. The method has since been coined the Standard Calculation Method or the 0D method, and corresponds to one of the methods used for estimating the pressure load in this thesis. (Anantavanich 2010, pp. 3-27) Although computationally fast, the method has some drawbacks. The assumption of a spatially similar pressure distribution is not necessary valid for compartments with complex inner structures as shown by Besnard (2009). On the other hand, the issue can be addressed at least partially as will be shown in Section 2.2.3.

Only a portion of the arc power heats the surrounding gas, and determining the fraction is challenging. The first mathematical formulations of the Standard Calculation Method relied on estimates for the fraction, commonly denoted by k_p in the literature. Initially k_p was determined exclusively from arc experiments. Based on the findings by Friberg (1998) the k_p fraction generally decreases as the gas density declines, provided that chemical reactions and ablation of metal are insignificant. For cupper electrodes at standard conditions the fraction is typically 0.40-0.65 according to Anantavanich (2010, p. 13). Attempts at estimating the fraction from first principles were made with promising results by Zhang et al. (2006).

Attempts at obtaining spatial pressure differences were initially done using the Ray Tracing Technique. The idea was based on considering the arc as source emitting pressure particles stochastically. The local pressure was then obtained by counting the number of particles in a specific time interval. (Dasbach et al. 1990) The method has not seen

extensive support from academia, and only little research on its applicability has been conducted.

In recent years Computational Fluid Dynamics seems to have become the tool of choice when estimating the pressure wave propagation in complex geometries, and corresponds to the second approach used in this thesis for estimating the pressure load. The drawback is the large modeling and computational effort, although benefits can be found in the obtained spatial accuracy. Generally the approach is applied to enclosures with large fluid volumes, as convergence in small volumes is difficult to obtain. Current research is focused on taking into account radiation losses from the arc, and metal ablation at the arc root. These additions make the use of a k_p fraction redundant. (Besnard 2009) In order to lower the computational effort the fluid volume inside the cabinet is often simplified greatly. (Uzelac et al. 2014, pp. 55-56) Asanuma et al. (2014) claim that the viscous terms could be dropped from the fluid simulation in order to lower the computational time without losing significant accuracy.

In the future sophisticated models would possibly be based on modeling the arc using the fundamental hydromagnetic equations describing the plasma and arc root. The energy transfer from the arc to the fluid would then be a boundary condition for the heating of the gas, which would yield the boundary condition for the structural analysis. The simulation approach has not been attempted yet to the best knowledge of the author due to the extreme computational time involved. There are some benefits to modeling the arc itself, since this would possibly allow the accurate prediction of the arc movement inside the structure. Arcs are sometimes found to jump to the enclosure walls, immediately puncturing the structure. (Uzelac et al. 2014, pp. 56-115) According to Wilson (1955) electric arcs comprise one of the hottest regions on earth, with arc temperatures reaching up to 15 000 K. No realistic enclosure thickness can therefore mitigate the effect of arc burn through. Some general design recommendations for lowering the probability of arcs jumping are given in Section 6.

The structural response to the pressure load is computed using a one-way fluid-structure interaction analysis, where the deformations of the structure do not alter the boundary conditions in the fluid simulation. This is a generally a reasonable estimate, since cabinet deformations do not alter the fluid flow significantly. A more time consuming and accurate approach would be to model the phenomenon using a full two-way fluid structure interaction analysis. This type of analysis was not found documented in the literature at the time of writing this work. The extreme computational times involved make the approach unfeasible for realistic cabinet designs. Furthermore, the large uncertainty present makes attempts at obtaining highly accurate results unappealing. A one-way analysis yields a more conservative approximation for the pressure load with significant savings in computational time, which advocates its use in industry applications.

Besnard (2009) estimated that an arc can release up to 20 MJ of energy in a time period of one second, which corresponds to the energy released by roughly 5 kg of TNT explosives. The energy release rate in arc flash events is much lower compared to conventional explosions, however. According to Nettleton (1976) the influence of shock waves can therefore generally be neglected in the analysis. Usually the averaged overpressure inside a switchgear due to an arc blast event is in the order of multiple bars according to Babrauskas (2010).

Several design principles have been employed by the industry in order to mitigate the effects of arc blasts. Relief discs are customarily fitted to switchgear panels. The discs are designed to open before the pressure in the structure grows too high, ensuring that the rapidly expanding pressure front is directed in a safe direction. Aside from relief discs, insulating gases and arc energy absorbers are often used. The most common insulating gas is SF_6, which acts as an electric insulator and results in a more unlikely arc formation compared to air.

Arc energy absorbers are made of multiple parallel channels of expanded metal, which absorb energy from the arc and cause pressure loss. Usually the absorber is placed inside the cabinet in front of the relief disc. (Anantavanich 2010, p. 2) Two arc energy absorbers are shown in Figure 2.

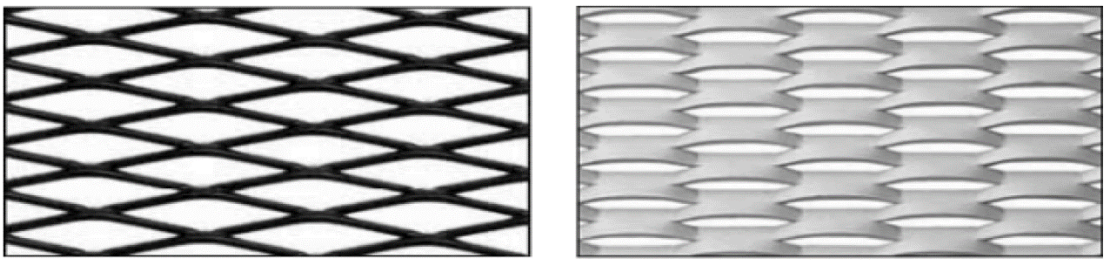

Figure 2. Frontal view of two different arc energy absorbers (Anantavanich 2010, p. 36).

Standards applicable for arc resistance tests are presented in Table 1. Apart from these standards, technical guides such as IEC/TR 61641 have been created in order to support arc testing of enclosed structures. No standards applicable to relief disc or cabinet dimensioning were found in the literature.

Table 1. Applicable standards in arc flash tests.

Standard	Applicability
IEC 62271-200	Medium voltage metal-enclosed switchgear and controlgear
IEC 62271-202	High/low voltage prefabricated substation
IEC 62271-203	High voltage gas-insulated metal-enclosed switchgear

2 Energy balance and pressure buildup

The energy balance of an arc flash event is presented, along with two methods for determining the pressure load acting on the cabinet. The conversion of a pressure load to a structural response is finally investigated.

2.1 Energy balance of an arc flash event

An electric arc transfers energy to the surroundings through diverse mechanisms. A complete energy balance was presented by Anantavanich (2010, p. 11), and the result is visualized in Figure 3.

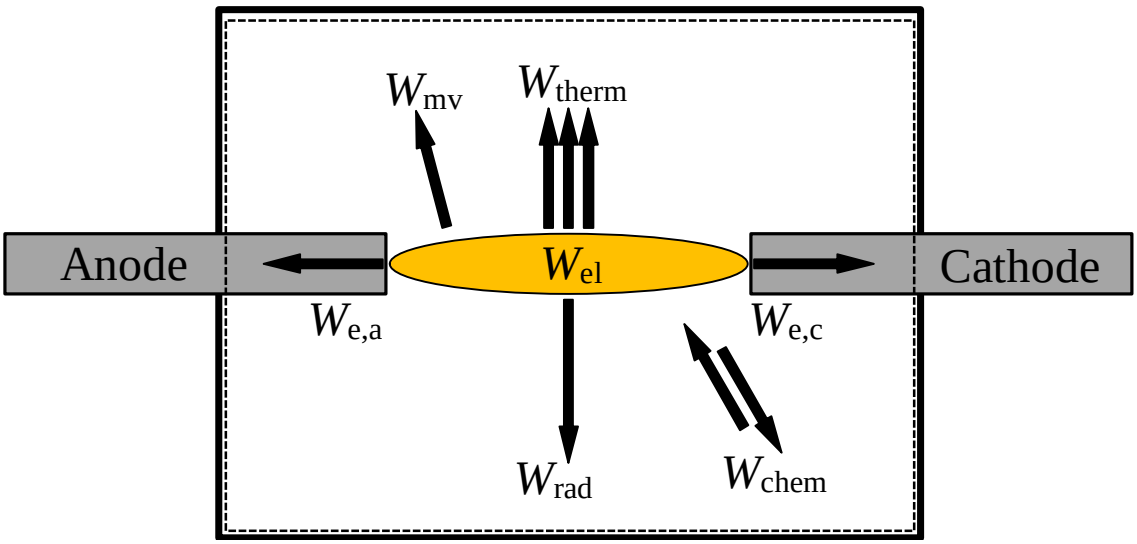

Figure 3. Energy balance of an arc flash event.

Mathematically the energy balance can be formulated as

$$W_{el} \pm W_{chem} = W_{e,a} + W_{e,c} + W_{mv} + W_{therm} + W_{rad}. \tag{2.1}$$

The energy released by the arc is denoted by W_{el} and is computed from

$$W_{el} = \int_{\Delta t} P_{el}(t)\,\mathrm{d}t, \tag{2.2}$$

where $P_{el}(t)$ is the arc power. A portion of the arc energy heats up the electrodes, accounted for by $W_{e,a}$ and $W_{e,c}$ respectively. If the arc current exceeds the order of a few kiloamperes, the electrodes will heat up to the point where significant melting occurs (Iwata et al. 2008). Most of the molten material forms droplets which splash around the cabinet. Only a fraction of the molten electrode material will vaporize further. (Øyvang et al. 2011) The energy required to melt and vaporize part of the electrodes is denoted by W_{mv}.

The vaporized electrode material can react with the gas in the enclosure, releasing energy further as discussed by Iwata et al. (2008). For copper electrodes in air the following reactions occur

$$\begin{aligned} \mathrm{Cu} + \frac{1}{2}\mathrm{O_2} \quad &\Rightarrow \quad \mathrm{CuO} \quad +155\ \mathrm{kJ/mol} \\ \mathrm{Cu} + \mathrm{O_2} \quad &\Rightarrow \quad \mathrm{CuO_2} \quad +168\ \mathrm{kJ/mol.} \end{aligned} \tag{2.3}$$

Predicting which reaction dominates is difficult. Fortunately the released energy is of the same order in both reactions. Sufficiently accurate approximations are therefore feasible.

Chemical reactions between the vaporized electrode material and the gas is included as a positive term in W_{chem}. Endothermic chemical reactions such as the ionization of molecules requires energy, and contribute to the W_{chem} term negatively. The ionized gas is capable of carrying electric charge, which can result if the formation of multiple new arcs after the initial flash.

A part of the energy is transferred to the enclosure and inner structures in the form of radiation, denoted in Figure 3 by W_{rad}. The term can be approximated using the Elenbaas-Heller energy balance equation as proposed by Singh and Summer (2011). Alternatively, the P-1 radiation model can be used (Melot et al. 2011).

The energy used to heating up the gas inside the cabinet is denoted by W_{therm}, and is of most interest in the blast analysis. The ability to predict the term accurately is crucial if correct overpressures are desired. A thermal transfer coefficient k_{p} has customarily been adopted in the past in order to describe the amount of arc energy contributing to pressure rise. It is defined as

$$k_{\mathrm{p}} = \frac{W_{\mathrm{therm}}}{W_{\mathrm{el}}}. \tag{2.4}$$

Estimating the thermal transfer coefficient has been an area of great research. The factor depends on the gas under consideration, its density, the volume of the compartment, and the electrode material. The k_{p} factor has been found to range between 0.4-0.65 for air at standard conditions with copper electrodes Anantavanich (2010, pp. 12-13). It is evident that uncertainty in W_{therm} is ultimately reflected as uncertainty in the structural response.

When the relief disc has opened and gas escapes the enclosure, the thermal transfer coefficient decreases. Should the fraction remain constant, the gas temperatures would quickly reach unrealistic values (Uzelac et al. 2014, pp. 135-136).

The definition of the thermal transfer coefficient in Eq. (2.4) follows the normal convention in the literature, in the sense that the definition is made in terms of energy relations and not power relations. The implication is then that k_{p} is in fact the averaged transfer coefficient corresponding to the time period Δt in Eq. (2.1). In practice, the time period has to approach zero to allow for variation in k_{p}, although this is never explicitly mentioned in the literature.

Pressure loads computed using the Standard Calculation Method in this thesis do not rely on the k_{p} fraction. Instead, a more sophisticated approach is used for the energy balance as developed by Becerra and Ostrowski (2014), which is based on enthalpy relations. It is not in the scope of this thesis to present the energy balance.

2.2 Pressure load using the Standard Calculation Method

The Standard Calculation Method, or SCM, offers a straightforward approach for estimating the pressure rise in an enclosed volume due to an internal arcing event. The differential equation governing the pressure rise in a closed volume is first presented, after which the more general equations applicable to cabinets with outlets are introduced.

2.2.1 Sealed enclosures

By applying the ideal gas law and the energy conservation equation to the cabinet gas, a differential equation for the spatially averaged pressure rise is obtained. The result is

$$\frac{\mathrm{d}p}{\mathrm{d}t} = \frac{(\kappa - 1) P_{\mathrm{therm}}(t)}{V}, \tag{2.5}$$

where dp is the differential increase in pressure over the time dt, κ is the adiabatic coefficient of the gas with a volume V, and P_{therm} is the power relating to the thermal energy W_{therm} in Eq. (2.1). More accurate results are obtained if a real gas law is used. Anantavanich (2010, p. 3)

The differential equation is readily solved numerically using for instance the Runge-Kutta method. The strength of the method is its simplicity. Solving the spatially averaged pressure distribution takes little time, although it may yield unsatisfactory results for complex cabinets. Eq. (2.5) does not take into account pressure waves, relief discs or flow leaking through possible openings.

2.2.2 Enclosures with openings

The SCM can be extended to cabinets with openings. The approach is beneficial for example when estimating the effects of relief discs on the overpressure. The disc is modeled as a fluid outlet, which appears after the averaged pressure reaches a critical value.

In reality, the opening of the relief disc does not only depend on the local overpressure, but also on how quickly the pressure rises. The SCM neglects the effects of the rise time on the operation of the relief disc, as the disc is considered to have opened when the pressure exceeds a predefined value. Depending on how the disc is designed, the error is either negligible or possibly large. By performing a separate structural analysis on the relief disc with several pressure rise times, it is possible to determine if the simplification used by the SCM is reasonable.

Furthermore, since the pressure is assumed to rise instantaneously at every location in the arc volume, the relief disc may erroneously be predicted open before the actual overpressure front has reached the relief disc. This is especially true for cabinets with complex inner structures, which contain obstacles hindering the pressure front from advancing. Generally the results are not affected greatly by the simplification, however. The large advancing velocity of the overpressure front ensures that the assumptions made in the SCM are often reasonable. The pressure peak is commonly observed several magnitudes in time after the overpressure wave has reached the relief disc.

On the other hand, if the arc ignites close to the relief disc in a large fluid volume, the SCM might produce conservative results as the averaged pressure rise would be much slower compared to the local overpressure rise at the relief disc.

The differential equations which are to be solved for cabinets with outlets are derived by Friberg (1998) and summarized below. The index AR refers to the arc volume, and RR to the relief room where the exhaust gas flows.

The pressure rise in the volumes can be solved once the escaped gas mass is known, along with the change in gas temperature. The incremental change in gas mass is computed from

$$\mathrm{d}m_{\text{AR-RR}} = \alpha A \rho_{\text{e}} v_{\text{e}} \mathrm{d}t, \tag{2.6}$$

where α is a discharge coefficient describing the friction loss and shape associated with the opening. The value of α is typically between 0.59-0.75 according to findings by Oberthür (1986) and Friberg (1998). Experiments or a steady-state CFD computation is required to obtain the value of the discharge coefficient. A is the cross-sectional area of the opening, which should not be larger than 10 % of the corresponding surface area for reliable results (Uzelac et al. 2014, p. 24). Finally, ρ_{e} is the gas density at the opening, v_{e} is the flow velocity at the opening and dt is the increment in time. Uzelac et al. (2014, 131) have presented equations for estimating ρ_{e} and v_{e}. The change in temperature in the arc volume is then

$$\mathrm{d}T_{\text{AR}} = \frac{P_{\text{therm}}(t)\mathrm{d}t - \mathrm{d}m_{\text{AR-RR}}\left[h(T_{\text{AR}}) - u(T_{\text{AR}})\right]}{m_{\text{AR}} c_{\text{v}}(T_{\text{AR}})}, \tag{2.7}$$

where $u(T_{\text{AR}})$ and $h(T_{\text{AR}})$ relate to the internal energy and enthalpy of the gas in the arc room, and $c_{\text{v}}(T_{\text{AR}})$ is the specific heat capacity at constant volume of the gas. Once the change in mass and temperature are known, the spatially averaged pressure inside the cabinet is solved using the ideal gas law as

$$p_{\text{AR}} + \mathrm{d}p_{\text{AR}} = \frac{(m_{\text{AR}} - \mathrm{d}m_{\text{AR}})R(T_{\text{AR}} + \mathrm{d}T_{\text{AR}})}{M_{\text{AR}}(T_{\text{AR}})V_{\text{AR}}}, \tag{2.8}$$

where R is the ideal gas constant, V_{AR} is the arc volume, and M_{AR} is the molar mass of the gas in the arc room. Since electrode evaporation may increase the gas mass significantly, the molar mass is assumed to depend on the temperature. The same reasoning can be used to obtain the temperature and pressure in the relief room.

Figure 4 shows a typical pressure load obtained using the SCM. Contrary to intuition, the pressure peak is commonly observed after the relief disc has opened. The situation occurs if the pressure increases faster than what can be compensated by the volumetric outflow through the opening.

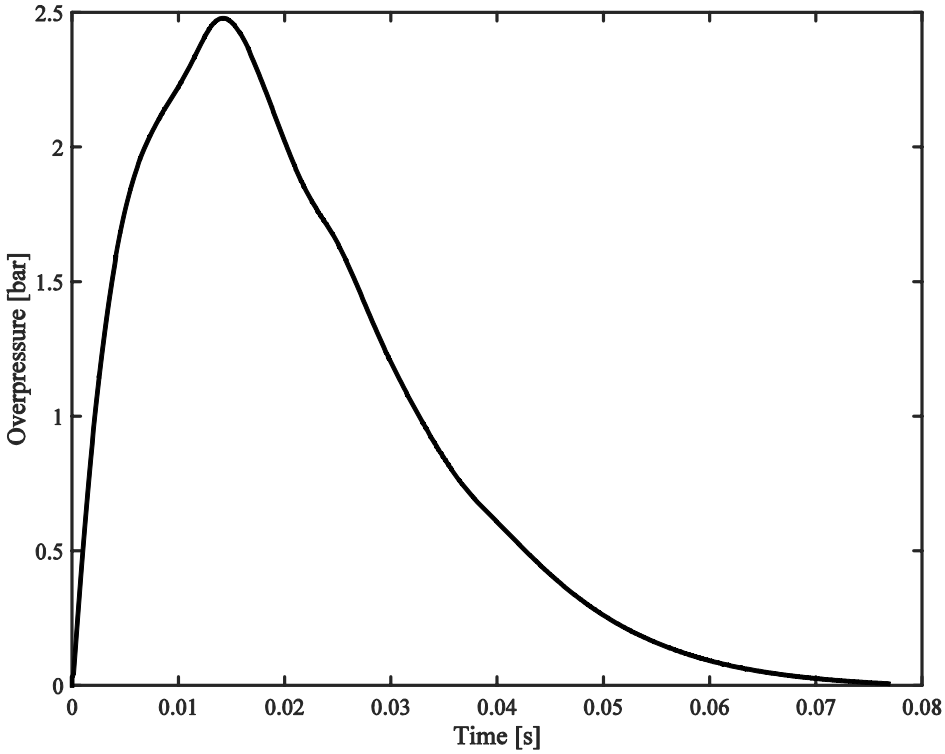

Figure 4. Example pressure load obtained using the SCM.

Considering the structural response, the highest stress state is observed slightly after the pressure peak has occurred, assuming the cabinet is still intact. This is explained by the inertia of the structure, which causes the structure to continue deforming despite the fact that the pressure has begun to decrease.

2.2.3 Chaining multiple volumes

In cases where the gas volume can be thought of as divided into smaller subsections, the SCM can be modified to yield pressure variation within each subvolume. The subvolumes are connected to each other using the principle of openings presented in Section 2.2.2, which are considered open from the start of the analysis. Several openings can be connected each subvolume if desired. The principle is demonstrated in Figure 5.

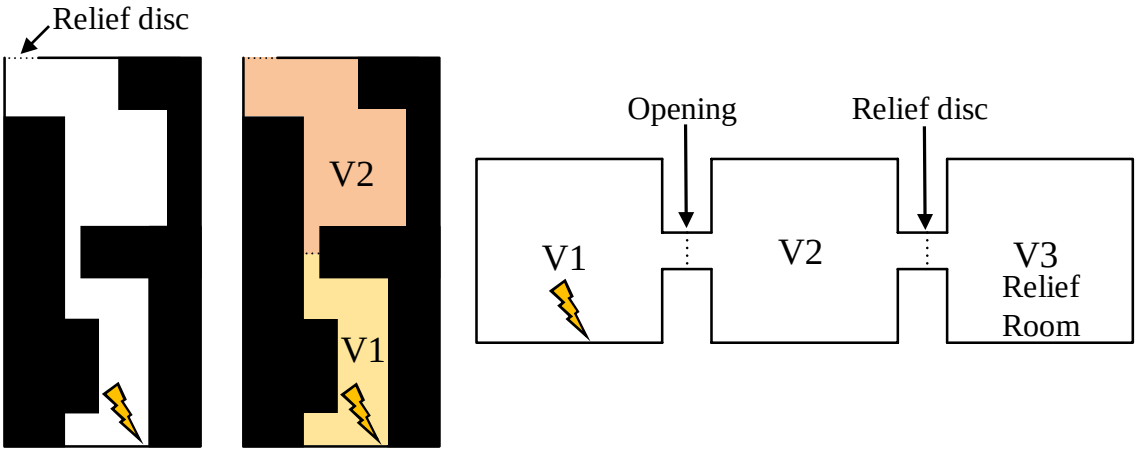

Figure 5. Division of fluid volume into smaller subvolumes.

Unfortunately the chaining of volumes does not work in cases where the opening area between connected volumes is large, since the gas flow velocity increases too much (Anantavanich 2010, p. 25). On the other hand, large openings make the assumption of one fluid volume with similar pressure distribution everywhere more feasible.

Since the SCM yields the spatially averaged pressure load, the estimated netload on structural components completely surrounded by the gas is zero. It is therefore not possible to estimate the stress state of components inside the structure in a general case. Luckily this is not a major drawback of the method, as the only desire is for the outer portions of the cabinet to withstand the blast.

2.3 Pressure load using Computational Fluid Mechanics

Computational fluid dynamics, or CFD, is currently the most accurate and established way of modeling the spatial pressure rise in arc flash events. The theory behind CFD is based on the numerical solution of the fundamental equations derived in theoretical fluid mechanics. Introductions to the topic are presented for instance by Fletcher (1991) and Patankar (1980).

In order to predict the transient pressure distribution the conservation of mass, momentum and energy –equations have to be modified and solved. The derivations of the equations presented in this chapter can be found from any standard textbook on fluid dynamics, for instance White (2005).The focus is therefore on presenting the necessary modifications of the fundamental equations relating specifically to arc flashes.

2.3.1 Conservation of mass

The equation for conservation of mass can be written in differential form as

$$\frac{\partial \rho}{\partial t} + \nabla \cdot (\rho \boldsymbol{v}) = S_{\mathrm{M}}, \tag{2.9}$$

where ρ refers to fluid density and $\boldsymbol{v}$ is the fluid velocity vector. In arc flash events the vaporization of electrode material increases the mass of the fluid, which can be taken into account by adding a mass source term denoted by S_{M} (Besnard 2009). Øyvang et al. (2011) propose that only a small portion of the electrode mass loss can be associated with vaporization, which in turn can react with the cabinet gas. Instead, the splashing of molten electrode material accounts for most of the mass change.

2.3.2 Conservation of momentum

The equations for conservation of momentum have the following form for viscous, compressible flow

$$\frac{\partial (\rho \boldsymbol{v})}{\partial t} + \nabla \cdot (\rho \boldsymbol{v}\boldsymbol{v}) = -\nabla p + \nabla \cdot (\eta \nabla \boldsymbol{v}) + \boldsymbol{S}_{\mathrm{F}}, \tag{2.10}$$

where p is the fluid pressure and η the dynamic viscosity of the fluid. $\boldsymbol{S}_{\mathrm{F}}$ is the momentum source term which is modified to suit arc flash events (Singh and Summer, 2011). It is worth emphasizing that Eq. (2.10) consists of three separate equations, as the momentum

has to be conserved in each of the three spatial directions. The system of equations are generally known as the Navier-Stokes equations.

2.3.3 The energy equation

The compressible nature of the fluid suggests that the pressure is highly coupled with the temperature and density, implying that the energy equation must be solved. Mathematically the equation can be written as

$$\frac{\partial(\rho h_0)}{\partial t} + \nabla \cdot (\rho h_0 \boldsymbol{v}) = \nabla \cdot (\lambda \nabla T) + \frac{\partial p}{\partial t} + \nabla \cdot (\boldsymbol{\tau} \boldsymbol{v}) + S_{\mathrm{E}}, \tag{2.11}$$

where $h_0 = h+(\boldsymbol{v}\cdot\boldsymbol{v})/2$ is the total specific enthalpy measured in m^2/s^2, λ is the thermal conductivity coefficient, p is the pressure and $\boldsymbol{\tau}$ is the viscous stress tensor. S_{E} is the heat source term, which is modified to take into account the energy released by the arc.

2.3.4 Fluid enthalpy and equation of state

Five equations and seven unknowns are present in Eq. (2.9)-(2.11), namely ρ, p, h, T and $\boldsymbol{v}$, where the velocity vector consists of three components. Two more equations are required to ensure that the problem is well-posed. This is done by implementing an equation of state for the density and enthalpy as follows

$$\rho = f(p,T) \tag{2.12}$$

and

$$h = g(p,T). \tag{2.13}$$

For accurate results Eq. (2.12) and Eq. (2.13) should be based on the theory of real gases. By adapting the ideal gas law the analysis is simplified greatly because

$$\rho_{\mathrm{ideal}} = \frac{pM}{RT} \tag{2.14}$$

and

$$h_{\mathrm{ideal}} = c_{\mathrm{p}}(T - T_0) \tag{2.15}$$

where c_{p} is the specific heat capacity at constant pressure, computed at the average temperature between T and the reference temperature T_0. The specific heat capacity for an ideal gas is only dependent on the temperature according to Lampinen (2010, p. 58), explaining the counterintuitive result of introducing the c_{p} term in a flow problem where the pressure is not constant.

2.3.5 Turbulence model

According to Anantavanich (2010, 19) a turbulence model is required to predict the fluid flow accurately, due to the low viscosity and high flow velocity of the gas. Many approaches are feasible when modeling the effects of turbulence. In arc blast simulations the standard k-ε model is often applied. The idea behind the k-ε model is to split the fluid flow into a mean flow velocity and a fluctuating component representing turbulence, which then replaces the velocity in the flow equations.

The *k*-ε model introduces two more unknowns, namely the turbulent kinetic energy *k* and the dissipation rate ε (Anantavanich 2010, p. 107). Two additional equations are therefore required, namely

$$\frac{\partial(\rho k)}{\partial t}+\nabla\cdot(\rho \mathbf{v} k)=\nabla\left[\left(\eta+\frac{\eta_{\mathrm{t}}}{\sigma_{\mathrm{k}}}\right)\nabla k\right]+P+G-\rho\varepsilon \tag{2.16}$$

$$\frac{\partial(\rho \varepsilon)}{\partial t}+\nabla\cdot(\rho \mathbf{v} \varepsilon)=\nabla\left[\left(\eta+\frac{\eta_{\mathrm{t}}}{\sigma_{\varepsilon}}\right)\nabla \varepsilon\right]+C_{1}\frac{\varepsilon}{k}P-C_{2}\rho\frac{\varepsilon^{2}}{k}. \tag{2.17}$$

2.3.6 Flow boundary conditions

Boundary conditions are required to ensure that the flow problem is well-posed and solvable. In arc blast simulations boundary conditions are generally required on boundaries in contact with the structure, and at the relief disc when the fluid is able to escape to the surroundings. It is also possible to model the effects of arc energy absorbers using appropriate boundary conditions, but they are neglected in this thesis. Anantavanich (2010, p. 22)

The boundary of the fluid volume in direct contact with the structure requires a no-slip boundary condition, which implies that flow normal and tangential to the boundary is zero. The first requirement is evident from the impermeability of enclosures. The second requirement follows from the fact that fluid parcels at a solid boundary will have zero relative velocity to it.

The fluid boundary in contact with the relief disc is modeled as a no-slip boundary until the average pressure at the disc reaches a critical value. The disc is then subsequently assumed to have opened, implying that the fluid inside the structure is able to escape to the surroundings. The appropriate condition for the disc is then usually an outlet boundary condition, which states that the pressure at the opening is equivalent to the surrounding air pressure, and that conserved quantities are allowed to penetrate the opening. (Anantavanich 2010, p. 22)

2.3.7 Solution method and general remarks

Currently most commercial solvers utilize the finite volume method when solving fluid flow problems. Introductions to the method are presented by Fletcher (1991) and Patankar (1980). The idea is to turn the set or partial differential equations presented in Eq. (2.9)-(2.17) into algebraic equations. Values such as flow velocity, density and temperature are then obtained at discrete locations in the fluid volume as a function of time.

According to Patankar (1980, p. 31) the most appealing property of the finite volume method is that it is conservative by nature, implying that the solution method follows the physics of the problem closely. Moreover, the finite volume method is readily extendable to unstructured meshes, which is essential when estimating pressure propagation in complex cabinet structures.

Utilizing CFD requires substantial computational resources, and creating a sufficiently accurate model which is solvable in a reasonable timeframe is difficult. The benefit of the method is that it follows the physics of the problem closely.

Modeling the pressure wave propagation in a gas is difficult due to high compressibility effects, which implies that a fine discretization has to be used. For small fluid volumes and large arc energies the gas temperature often grows extremely high, increasing the difficulty to obtain a converged solution further.

3 Aspects of pressure computations

Although not in the immediate scope of this thesis, some general remarks regarding dimensioning principles are considered vital and therefore shared. Understanding the limitations of the methods presented so far is essential, if the goal is to obtain reliable results.

3.1 Relief disc dimensioning

The process of relief disc dimensioning is iterative. Initial estimates should therefore be done using the computationally efficient SCM presented in Section 2.2. Once the corresponding overpressures seem reasonable, a more time-consuming CFD computation is recommended to verify the results. Alternatively, a structural simulation on the structural response can be performed directly if the analyst has sufficient confidence in the initial results. The concept of reasonable overpressure is introduced ambiguously on purpose. No general guidelines for the severity of the overpressure can be defined, as it is highly dependent on the cabinet design. Experience is then the best guide when determining if a specific overpressure is too high. Luckily the issue is not critical, since a structural analysis can always be conducted if the severity of the overpressure is uncertain to the analyst. Determining the appropriate size of the relief disc is generally easy.

Once the shape and area of the relief disc are determined, a separate structural analysis is required to verify the correct opening of the disc at the specified opening pressure. The effects of pressure rise time on the opening of the disc should also be investigated. Generally it is reasonable to assume that the pressure across the relief disc surface is constant. The assumption is valid as long as the relief disc is small.

Depending on the design of the relief disc, the structural analysis is either cumbersome or simple. The analysis is simple if the operation of the disc does not depend on material damage and failure. Such is the case if for example a spring-type design is used. Designs which rely on material failure at predefined connections are more troubling to the analyst, as the reliable modeling of material damage and failure is challenging. For instance, the Johnson-Cook dynamic failure model used extensively in solid mechanics is highly mesh sensitive as discussed by Ljustina et al. (2014). Li and Xingwen (2010) have proposed a method to circumvent the mesh density issue when modeling material failure, however.

The design requirements relating to the relief disc dimensioning are unfortunately often conflicting. On one hand the relief disc should be structurally weak, to ensure that overpressures caused by the arc flash do not grow too high. On the other hand, the structure should be able to withstand prolonged vibration in industry use, which demands the relief disc to be fastened appropriately.

The number of possible relief disc designs are almost limitless, and focusing on finding the optimal design would certainly amount to a thesis of its own. The issue represents an engineering challenge more than a scientific pursuit, however. It is therefore not in the scope of this thesis to investigate the matter further. The tools presented in this thesis are applicable to dimensioning the relief disc, and to verify the correct opening of the disc.

3.2 Undesired flow leakage

Cabinet designs are seldom completely airtight, implying that part of the pressure leaks out through diverse openings in the structure. On a quick glance the results are desired. Flow leaking through openings decreases the overpressure inside the cabinet, thus lowering the stress state in the structure. The issue is unfortunately more complex.

For openings which remain constant in size during the arc flash event, the analysis is seemingly straightforward. Both the SCM and the CFD approach can be used by implementing outlets in the models. A great deal of caution has to be used when analyzing the results, however. Droplets of molten electrode material and fire protruding through the openings are extremely dangerous to bystanders, and can result in the failure of an arc flash test. As it is unfeasible to model these effects reliably, one cannot conclude that the design is safe based on structural simulations alone.

For openings which expand during the outflow of the gas, the issue is even more severe. The structural computation cannot necessarily be assumed uncoupled from the pressure simulation, implying that the methods presented in this thesis require modification. At worst, the overpressure escapes completely through the openings, ensuring that the relief disc remains shut. The outcome is clearly undesired.

Simulation tools presented in this thesis do not offer an ultimate solution, and have to be coupled with caution in order to be effective. Problems regarding flow leakage should first and foremost be addressed by employing effective design principles, to ensure that the simulation tools do not have to be applied in uncertain areas at all.

The problem of undesired flow leakage along with a possible design correction is visualized in Figure 6. The front plate of the cabinet on the left is only fastened to the enclosure at the corners. The resulting opening is substantial, and implies that the assumption of uncoupled solutions is possibly invalid. Furthermore, the large deformations hint that dangerous fire and molten droplets of metal can escape the cabinet through the openings. By adding fasteners to the structure as shown on the right in Figure 6, the flow is unable to escape the enclosure through undesired locations. The solutions also become uncoupled, implying that the methods presented in this thesis are applicable.

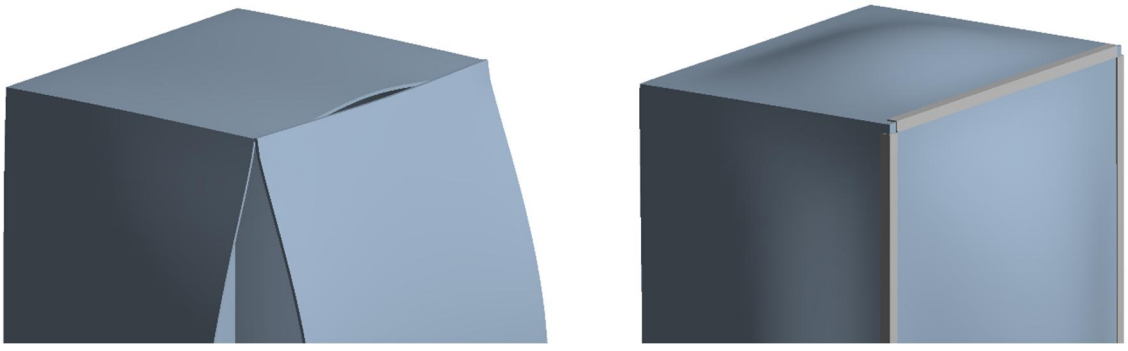

Figure 6. Undesired flow leakage on the left, and an improved design on the right. Both cases were simulated using ANSYS® (2015a).

4 Governing principles of the structural response

The mathematical theory behind structural dynamics is both lengthy and well-documented, hence only the main points referring specifically to arc blasts are reproduced here. Both geometric and material nonlinearities are expected to be present aside from inertial effects, which increases the difficulty of the analysis. An introduction to the topic of structural dynamics is presented by Craig and Kurdila (2006), and a more theoretical approach to nonlinear continuum mechanics by Dimitrienko (2011).

4.1 Discretized equations

For a complete derivation of the equations governing the conservation of linear momentum, the reader is invited to familiarize with the work of Malvern (1969, p. 214). The resulting equations can be simplified to some extent in relation to arc blasts. Body forces generally expressing gravitational pull or electromagnetic relations can readily be neglected. Furthermore, thermal loads caused by the heating of the enclosure account for secondary effects, and are not taken into account.

The governing continuum equations are typically solved numerically using the Finite Element Method. Introductions to the topic are presented for instance by Ottosen and Petersson (1992) and Cook et al. (2001). The semi-discretized form of the equations derived by Malvern (1969, p. 214) can be written according to ANSYS® (2015b, p. 764) as

$$\boldsymbol{M}\ddot{\boldsymbol{u}}+\boldsymbol{C}\dot{\boldsymbol{u}}+\boldsymbol{F}^{\mathrm{i}}\left(t\right)=\boldsymbol{F}^{\mathrm{a}}\left(t\right), \tag{2.18}$$

where the mass matrix $\boldsymbol{M}$ describes the inertia, and $\boldsymbol{C}$ the damping effects of the structure. $\boldsymbol{F}^{\mathrm{i}}(t)$ represents the stiffness of the structure and takes into account both material and geometric nonlinearities. The vector $\boldsymbol{F}^{\mathrm{a}}(t)$ describes the discretized pressure load caused by the arc flash, and is computed either using the SCM or CFD. The nodal displacement vector is denoted by $\boldsymbol{u} = \boldsymbol{u}(t)$, and its time derivatives are expressed using the dot notation.

4.2 Structural damping

One fundamental difficulty in structural dynamics is the correct modeling of damping, which is always present due to friction and resistance by the surrounding air. Its importance in modeling any dynamic phenomenon is apparent. Generally velocity proportional, or viscous damping is used. According to Cook et al. (2001, p. 389) the approach is generally sufficiently accurate if the damping forces are much smaller than the corresponding inertial and stiffness related forces.

Unfortunately, the stiffness matrix in Eq. (2.18) does not arise naturally from the equations governing conservation of momentum. Usually the damping matrix is formulated according to the principle of Rayleigh damping as a linear combination of the mass and stiffness –matrices (Cook et al. 2001, p. 389). For non-linear problems the tangential stiffness matrix is used (ANSYS® 2015b, p. 674). Mathematically the damping matrix can then be expressed as

$$\boldsymbol{C}=\alpha_{\mathrm{R}}\boldsymbol{M}+\beta_{\mathrm{R}}\boldsymbol{K}^{\mathrm{Ta}}\left(\boldsymbol{u}\right), \tag{2.19}$$

where $\boldsymbol{K}^{\mathrm{Ta}}(\boldsymbol{u})$ is the tangential stiffness matrix, and α_{R} and β_{R} represent the Rayleigh coefficients. The tangential stiffness matrix is used in this thesis because material plasticity and large-deflections imply that the stiffness matrix is not constant during the analysis. For severe plastic deformations the formulation in Eq. (2.19) might prove disadvantageous (ANSYS® 2015c, p. 6). The mass proportional part of the damping matrix damps the lower frequencies of the spectrum more efficiently, whereas the stiffness proportional damping contributes to the damping of higher modes more Cook et al. (2001, p. 390).

According to Cook et al. (2001, p. 389) the constants α_{R} and β_{R} are solved from the following system of equations

$$\begin{Bmatrix} \xi_{\mathrm{i}} \\ \xi_{\mathrm{j}} \end{Bmatrix} = \frac{1}{2} \begin{bmatrix} \omega_{\mathrm{i}}^{-1} & \omega_{\mathrm{i}} \\ \omega_{\mathrm{j}}^{-1} & \omega_{\mathrm{j}} \end{bmatrix} \begin{Bmatrix} \alpha_{\mathrm{R}} \\ \beta_{\mathrm{R}} \end{Bmatrix}, \tag{2.20}$$

where ξ_{i} and ξ_{j} refer to the damping ratios, and ω_{i} and ω_{j} correspond to the highest and lowest eigenfrequencies f_{i} and f_{j} of interest according to

$$\omega_{\mathrm{n}} = 2\pi f_{\mathrm{n}}. \tag{2.21}$$

The damping ratios are often unknown, and have to be estimated by the analyst if experimental data is unavailable. Generally the damping ratios are significantly smaller than unity, however.

The effects of altering the damping ratios on the central node total displacement of a generic steel plate under arc blast loading are visualized in Figure 7. For simplicity $\xi_{\mathrm{i}} = \xi_{\mathrm{j}}$. The corresponding values for α_R and β_R are shown in Table 2. The results should only be seen as an example on how adding damping alters the behavior of the cabinet plate, and not as a rigorous investigation on the effects of damping.

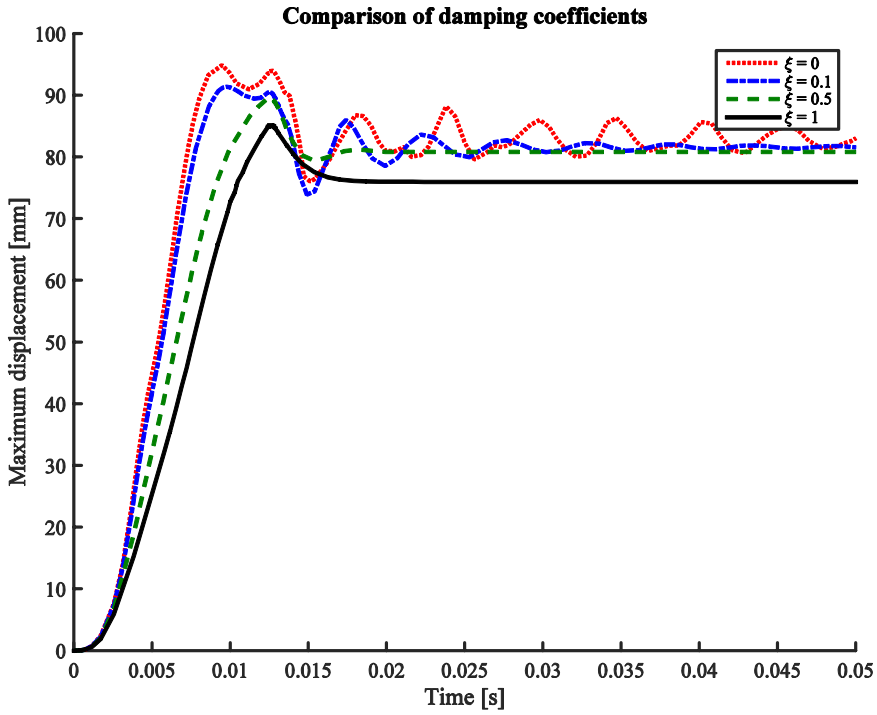

Figure 7. Effects of adding damping on the central node total displacement of a plate.

Table 2. Damping ratios corresponding to Figure 7.

ξ	α_R [1/s]	β_R [s]
0	0	0
0.1	42.6	0.0001
0.5	212.8	0.007
1	298.0	0.01

The vibrations shown in Figure 7 would eventually die out even for the case where no Rayleigh damping is added, since numerical damping is present in the time domain. Plastic deformations expected to occur in arc flash events also absorb a portion of the energy, which lowers the resulting vibration amplitudes of the plate.

One important factor to be aware of is the danger of adding too much damping. As can be seen in Figure 7, the maximum central node displacement for the damped response is slightly lower compared to the undamped response. Adding too much damping might therefore cause the deformations to be under predicted, implying that a dangerous design might erroneously be deemed safe.

Increased damping is also reflected in a lower rate of deformation. Larger damping implies a softer response to the arc blast, which in turn can yield false predictions. A rule of thumb is to first conduct the analysis without damping, and compare the results to the damped response. If the results differ greatly the implication is that too much damping has possibly been added.

4.3 Solution approach in time domain

Eq. (2.18) is solved in the time domain with respect to the displacement vector $\boldsymbol{u} = \boldsymbol{u}(t)$. Quantities such as strains and stresses are then obtained using derivatives of the nodal displacements.

Broadly speaking two types of methods can be employed to progress the solution in the time domain, namely explicit and implicit methods. Explicit methods rely completely on known values to obtain results at the next time step, which makes their implementation straightforward. Implicit methods predict values at the next time step using both known values at the current time step, and unknown values at the next time step. Implicit methods remain stable with larger time steps compared to explicit methods, although their stability should not be confused to imply accuracy. The downside of implicit methods is that they require more computational resources. (Cook et al. 2001, pp. 407-420)

In this thesis an implicit time integration scheme is used unless stated otherwise. Ensuring the correct mapping of the pressure load from the CFD solution to the structural solver advocates the use of equivalent time steps and an implicit solver (ANSYS® 2014, p. 5). The same approach is also used in relation to the SCM to keep the analysis procedure consistent.

In rapid dynamic events such as conventional blasts, explicit solvers are preferred according to Cook et al. (2001, p. 408). The pressure load caused by the arc flash has a much slower rise time compared to conventional explosions, however. According to

Cook et al. (2001, p. 408) implicit solvers are suitable if the rise time and duration of the load exceed the time it takes for a sound wave to travel through the structure by several multiples.

Based on the velocity of sound in steel provided by Aldred (1972), it takes roughly 0.2 ms for a sound wave to travel through a typical cabinet which is one meter tall. On the other hand, the computational rise time of the overpressure is commonly in the order of 20 ms or longer, implying that the problem suited for an implicit solver.

The Newmark implicit scheme used is based on updating the displacement and velocity according to

$$\begin{aligned} \dot{\boldsymbol{u}}_{n+1} &= \dot{\boldsymbol{u}}_n + \left[(1-\delta)\ddot{\boldsymbol{u}}_n + \delta \ddot{\boldsymbol{u}}_{n+1} \right] \Delta t \\ \boldsymbol{u}_{n+1} &= \boldsymbol{u}_n + \dot{\boldsymbol{u}}_n \Delta t + \left[\left(\frac{1}{2} - \alpha \right) \ddot{\boldsymbol{u}}_n + \alpha \ddot{\boldsymbol{u}}_{n+1} \right] \Delta t^2, \end{aligned} \tag{2.22}$$

where $\alpha = 0.3025$ and $\delta = 0.6$ correspond to the standard values used by the solver. The nodal accelerations and velocities at time step t_{n+1} are solved from Eq. (2.22) as a function of $\boldsymbol{u}_{n+1}$, and inserted in the fully discretized residual form of Eq. (2.18), yielding

$$\boldsymbol{R}_{n+1}\left(\boldsymbol{u}_{n+1}\right) = \boldsymbol{F}^{\mathrm{a}}_{n+1} - \boldsymbol{M}\ddot{\boldsymbol{u}}_{n+1} - \boldsymbol{C}\dot{\boldsymbol{u}}_{n+1} - \boldsymbol{F}^{\mathrm{i}}_{n+1}\left(\boldsymbol{u}_{n+1}\right). \tag{2.23}$$

The goal is then to find $\boldsymbol{u}_{n+1}$ iteratively for each time step, such that the norm of the residual vector $\boldsymbol{R}_{n+1}$ becomes sufficiently small. This implies that the balance required by Eq. (2.18) is obtained for each time step.

The updated estimate for the displacement vector at the $k+1$:th iteration for time step $n+1$ is

$$\boldsymbol{u}^{k+1}_{n+1} = \boldsymbol{u}^{k}_{n+1} + \Delta \boldsymbol{u}^{k}_{n+1}, \tag{2.24}$$

where $\Delta \boldsymbol{u}^{k}_{n+1}$ is obtained using the Newton-Raphson method from

$$\left[\left(a_0 \boldsymbol{M} + a_1 \boldsymbol{C} \right) + \left[\boldsymbol{K}^{\mathrm{Ta}}_{n+1}\left(\boldsymbol{u}^{k}_{n+1}\right) \right] \right] \Delta \boldsymbol{u}^{k}_{n+1} = \boldsymbol{R}_{n+1}\left(\boldsymbol{u}^{k}_{n+1}\right). \tag{2.25}$$

Here $\boldsymbol{K}^{\mathrm{Ta}}_{n+1}\left(\boldsymbol{u}^{k}_{n+1}\right)$ represents the tangent stiffness matrix and

$$\begin{aligned} a_0 &= \frac{1}{\alpha \Delta t^2} \\ a_1 &= \frac{\delta}{\alpha \Delta t}, \end{aligned} \tag{2.26}$$

where Δt is the time step. Once displacements are known, nodal velocities and accelerations are solved using Eq. (2.22). (ANSYS® 2015b, pp. 769-770)

To save computational effort, the time step size can automatically be altered by the computer as the solution progresses. The smaller the time step, the smaller the error if the effects of floating-point precision are neglected. Small time steps are not economical,

however, and should only be used when necessary. Error also depends on the rate at which the solution changes. If the displacement gradients are small with respect to time, larger time steps can be used while still keeping the error small. Rapidly fluctuating solutions require smaller time steps to maintain the same order of accuracy. The computer software automatically predicts the time step size to keep the error and computational time reasonable. (ANSYS® 2015b, pp. 686-687) When estimating the pressure load using the CFD approach, automatic time stepping is not a recommended option if the Application Customization Toolkit in ANSYS® is used.

The first time step is not determined by the software if the SCM is used. A good estimate frequently used by analysts is based on the highest eigenfrequency of interest of the structure, and a safety factor combined with the Nyquist sampling theorem. The result is

$$\Delta t_0 = \frac{1}{20 f_{\max}}, \tag{2.27}$$

where Δt_0 is the initial time step size, and $f_{\max}$ is the highest eigenfrequency of the system of interest (ANSYS® 2013, p. 24).

5 Material model

In order to determine the structural response, a constitutive equation taking into account the material stiffness has to be implemented in the model. The material model allows the unknown stresses to be expressed using strains, which in turn can be written using gradients of the displacement vector. The displacement vector is solved for each time step using Eq. (2.23), Strains and stresses are then obtained by reversing the procedure.

The material model has to cover both elastic deformations which are reversible, and plastic deformations which are permanent. Effects of strain rate on the material behavior should be investigated and quantified due to the dynamic nature of the problem.

Cabinets used in the electric industry are made of various materials, and no attempt is made to describe all of them. Commonly the materials are isotropic, however, implying that the material properties are direction independent (Santaoja 2012, p. 61). The focus of this thesis is therefore on investigating such materials. For thin plates the material behavior is generally only isotropic in the elastic range. When plastic strain begins to accumulate, the material behaves in an orthotropic fashion.

Parameters describing high deformation rates of materials are difficult to find in the literature, mainly because their application in the civil industry is limited. One common steel used extensively in the industry for which data is available, is A36 steel. The material was therefore investigated further in Section 5.4 and Section 7.1, when attempting to quantify the effects of including strain rate sensitivity in the material model.

The theory describing the behavior of ductile isotropic materials in the elastic and elastic-plastic region is not covered in this thesis, as the information is readily available from any introductory book in solid mechanics. An interested reader is encouraged to familiarize with either Parnes (2001) or Santaoja (2012) for further information.

The focus is on discussing matters relating specifically to arc flash events. First, the criterion used to determine the onset of yield in a general stress state is briefly described. The plasticity model is then shortly discussed, after which temperature effects on the material behavior are considered. Criterions used for material failure are finally examined, after which two different strain rate models are examined further.

5.1 Yield criterion and material plasticity

In order to generalize the yield criterion determined from a uniaxial tensile test to a general stress state in three dimensions, the concept of von Mises yield criterion is introduced. The criterion is applied due to its suitability to ductile materials commonly used in electrical switchgear. Mathematically the principle can be written as

$$\sigma_{\mathrm{VM}}^2 = \frac{1}{2}\left[\left(\sigma_{\mathrm{xx}} - \sigma_{\mathrm{yy}}\right)^2 + \left(\sigma_{\mathrm{yy}} - \sigma_{\mathrm{zz}}\right)^2 + \left(\sigma_{\mathrm{zz}} - \sigma_{\mathrm{xx}}\right)^2\right] + 3\left(\tau_{\mathrm{xy}}^2 + \tau_{\mathrm{yz}}^2 + \tau_{\mathrm{zx}}^2\right), \quad (2.28)$$

where σ_{VM} is the von Mises stress, and the components on the right-hand side correspond to the elements from the Cauchy stress tensor. In a three-dimensional stress state yielding occurs when the von Mises stress reaches the yield stress obtained in from the uniaxial tensile test. (Santaoja 2012, p. 386) Plotting the solution to Eq. (2.28) generates the von Mises yield surface.

The von Mises yield criterion is associated with the change of shape of a material element as opposed to a change in volume. It is derived by predicting that material yield occurs under arbitrary loading when the amount of absorbed distortional energy reaches a critical value. The conclusion was originally published by Hencky (1924, p. 323).

Once the von Mises stress is exceeded, plastic strain begins to accumulate in the structure. In this thesis the model for isotropic hardening is used as it is suitable for dynamic loading events, where considerable irreversible deformation occurs and the Bauschinger effect becomes distinguishable. Further information regarding plasticity, isotropic hardening and the Bauschinger effect are presented for instance by Rice (1975). Isotropic hardening is related to the uniform expansion of the yield surface as plastic straining occurs.

The von Mises criterion does not provide insight into failure of material elements as such. Damage and ultimate failure can commonly be associated with void nucleation, coalescence and growth in the material.

5.2 Temperature effects on material behavior

Material behavior is commonly temperature dependent, with the yield stress decreasing as the temperature increases (Chen et al. 2006). As mentioned in Section 2.1, the radiative losses from the arc are absorbed by the cabinet panels to some extent. Heat is also transferred from the gas inside the cabinet to the structure through convection. For most arc flash scenarios the temperature increase in the structure can be neglected, however, according to Anantavanich (2010, p. 22) and Zhang et al. (2006).

This thesis focuses on investigating how the structure responds to the blast load. As the peak pressure is commonly observed several magnitudes in time before the arc is extinguished, possible thermal effects have little effect during the blast analysis. The specific heat capacity of the enclosure is generally sufficiently large to ensure that the corresponding temperature rise is small.

If deemed necessary, however, the temperature rise in the structure can be computed if the heat flux entering the enclosure is known. The unknown heat flux can be separated into two parts, convection from the surrounding air, and radiative losses from the arc. When the heat flux entering the enclosure is known, the temperature rise in the enclosure can be solved. The corresponding effect on the yield stress can then be determined using for instance the Johnson-Cook material model if material data is available.

The heat flux entering the enclosure due to radiative losses from the arc can be estimated using the formula presented by Zhang et al. (2006), by approximating the portion of radiative energy absorbed by the enclosure. Depending on the construction, a varying portion of the radiative energy is absorbed by inner structures of the cabinet, which is of little interest when analyzing the temperature rise in the enclosure.

Estimating the heat transferred through convection is problematic if the computationally expensive CFD method is not utilized, as it is difficult to determine the value of the corresponding heat transfer coefficient. Approximate formulas for determining the value of the heat transfer coefficient under different circumstances have been developed. Their

applicability in arc flash events should be questioned, however, due to the extreme temperature and unknown flow velocity of the gas.

5.3 Material failure

For large overpressures and structurally weak constructions the computational stresses can become extremely large. The situation is clearly undesirable, and demands a redimensioning of the enclosure to ensure that the structural integrity is maintained. As mentioned in Section 5.1, the von Mises stress by itself is not an adequate tool for predicting material behavior after yield, which means that some other criterion has to be applied to determine if the structure is able to sustain the blast load without failure.

Several approaches are feasible when modeling the failure of ductile materials. A popular criteria extensively used in the industry is to assume that material failure occurs when the equivalent plastic strain reaches the fracture strain (Bugelli and Driemeier 2010). The criterion can be expressed mathematically as

$$\omega = \sum \frac{\Delta \bar{\varepsilon}_{\mathrm{p}}}{\varepsilon_{\mathrm{f}}}, \tag{2.29}$$

where the equivalent plastic strain is computed from

$$\Delta \bar{\varepsilon}_{\mathrm{p}} = \int_{t}^{t+\Delta t} \sqrt{\tfrac{2}{3}\left(\dot{\varepsilon}_1^2 + \dot{\varepsilon}_2^2 + \dot{\varepsilon}_3^2\right)}\, \mathrm{d}t \tag{2.30}$$

using the principal strain rates, and the fracture strain is denoted by ε_{f}. Failure occurs when the damage parameter $\omega = 1$. The fracture strain is obtained from the tensile test of the material.

Although convenient to compute, the usability of Eq. (2.29) is diminished to some extent by the fact that the fracture strain depends on the stress triaxiality η as

$$\varepsilon_{\mathrm{f}} \propto \exp\left(-\lambda \frac{\overbrace{\sigma_{\mathrm{m}}}^{=\eta}}{\sigma_{\mathrm{VM}}} \right), \tag{2.31}$$

where λ is a material constant, σ_{m} is the average principal stress and σ_{VM} is the von Mises stress (Oh et al. 2011). The strain rate and temperature also have an effect on the fracture strain besides stress triaxiality according to Johnson and Cook (1985). Besides ductile failure, shear failure of the material may also be an important aspect to consider depending on the design of the cabinet. By implementing the dependencies in the fracture strain in Eq. (2.29), a more accurate mathematical model can be created.

It is evident that the computational modelling of failure is challenging, as several parameters play an important role. Considering the discussion in Section 3.1, the mesh sensitivity issue associated with failure models complicates the usage further. The large uncertainty involved in arc flashes advocates the use of large safety factors, by requiring the equivalent plastic strains to remain small under all circumstances.

A theoretical introduction to damage mechanics is provided by Murakami (2012).

5.4 Strain rate effect of material behavior

The plasticity theory presented so far does not take into account the effects of strain rate on the material behaviour. Mansilla et al. (2000) amongst others have shown that an increase in strain rate raises the yield stress. Such effects are possibly visible in arc blasts simulations, which correspond to highly dynamic events. Several attempts have been made to capture the phenomenon. In this thesis the approaches presented by Cowper and Symonds (1958) and the relation introduced by Huh and Kang (2002) are investigated further.

Material parameters for the strain rate models are conventionally obtained by minimizing the sum of squares between predicted dynamic yield stresses, and corresponding measurements. A goodness of fit indicator is therefore the RMS value defined as

$$\mathrm{RMS} = \sqrt{\frac{\sum_{i=1}^{m}\left[Y_i - f\left(x_i\right)\right]^2}{m}}, \tag{2.32}$$

where Y_i is the i:th result of m measurements and $f(x_i)$ is the predicted result by the mathematical model. (Schwer 2007) From Eq. (2.32) it is clear that a better the fit implies a smaller RMS value. On the other hand, if the sample number is limited and the differences in RMS values remains small, is it likely that stochastic noise due to variation in sample yield stress explains the variation.

5.4.1 Cowper-Symonds strain rate dependence

The well-known strain rate dependence introduced by Cowper and Symonds (1958) can be expressed mathematically as

$$\frac{\dot{\sigma}_{\mathrm{yield}}}{\sigma_{\mathrm{yield}}} = 1 + \left(\frac{\dot{\bar{\varepsilon}}_{\mathrm{p}}}{C}\right)^{\frac{1}{P}}, \tag{2.33}$$

where $\dot{\sigma}_{\mathrm{yield}}$ is the predicted dynamic yield stress, σ_{yield} is the experimentally obtained yield stress corresponding to the quasi-static reference strain rate, and $\dot{\bar{\varepsilon}}_{\mathrm{p}}$ is the equivalent plastic strain rate. The constants C and P are material parameters determined by minimizing the residual sum of squares in accordance with Eq. (2.32). The parameters for A36 steel were obtained by Schwer (2007) and are shown in Table 3.

Table 3. Cowper-Symonds parameters for A36 steel obtained by Schwer (2007).

C [1/s]	P	RMS
333500	4.203	2.10

5.4.2 Huh-Kang strain rate dependence

Huh and Kang (2002) presented an improvement to the Johnson-Cook rate dependence model, by adding a term proportional to the square of the logarithmic effective plastic strain rate. The corresponding mathematical expression is

$$\frac{\dot{\sigma}_{\text{yield}}}{\sigma_{\text{yield}}} = 1 + C_1 \ln \dot{\varepsilon} + C_2 \left(\ln \dot{\varepsilon} \right)^2 , \tag{2.34}$$

where

$$\dot{\varepsilon} = \frac{\dot{\bar{\varepsilon}}_{\text{p}}}{\dot{\varepsilon}_0} \tag{2.35}$$

is the relative plastic strain rate, and expresses the relation between the equivalent plastic strain rate and the reference strain rate $\dot{\varepsilon}_0$ used to obtain the reference yield stress σ_{yield}. The constants C_1 and C_2 represent the Huh-Kang material parameters which were obtained by Schwer (2007) for A36 steel, and are shown in Table 4.

Table 4. The Huh-Kang parameters for A36 steel presented by Schwer (2007).

$\dot{\varepsilon}_0$	C_1	C_2	RMS
0.000154	0.002149	0.0009112	1.40

By comparing the RMS values from Table 3 and Table 4 it is clear that the Huh-Kang model provides a better fit. As described in relation with Eq. (2.32), the differences in RMS values is likely only stochastic noise due to variation in sample yield stress, if the number of samples remains small.

Numerical predictions are generally accurate close to the chosen reference strain rate, as indicated by Schwer (2007). In order to improve the results, one might be tempted to choose a reference strain rate close to the expected strain rate in the simulation case of interest. This approach should generally be avoided, however. Plasticity algorithms implemented in commercial solvers might fail to model material response for strain rates lower than the reference strain rate. For example, choosing the reference strain rate as 1 1/s and using the corresponding yield stress as the reference yield stress σ_{yield} in the Huh-Kang relation, produces the same stress-strain relation for lower strain rates as the reference stress-strain curve. In reality the stresses should be lower. This phenomena was shown to exist in the LS-DYNA commercial package by Schwer (2007), but the results were also reproduced in ABAQUS® (2015a) in this thesis. The reference strain rate should therefore always correspond to the quasi-static strain rate. As the reference strain rate is not present in the Cowper-Symonds relation, the problem is characteristic to relations where the concept of reference strain rate is present.

5.4.3 Numerical tensile tests

Numerical tensile tests at four different engineering strain rates were performed in order to compare the models more closely. The results were considered of value for a correct analysis of the results in Section 7.1, where the models were adapted to several typical arc flash scenarios. Furthermore, the results would verify partly that the strain rate models were implemented correctly in the software. All analyses were performed with ABAQUS® (2015a) due to the straightforward implementation of the strain rate models.

The numerical tensile tests were conducted by enforcing an axial displacement to one end of a linear beam element, while keeping the other end fixed. By altering the internal step time of the solver, different engineering strain rates were obtained. The schematic of the model is shown in Figure 8.

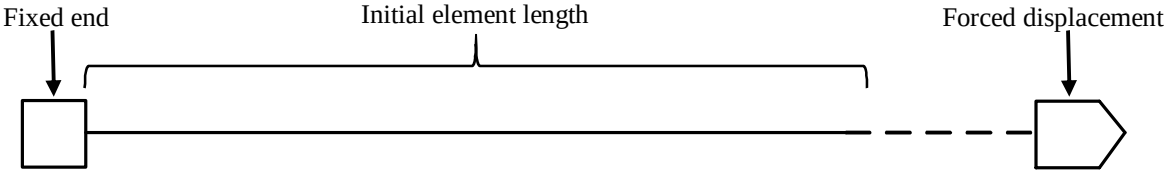

Figure 8. Schematic of numerical tensile test.

Damage or failure criterions were not implemented. Inertial effects were also neglected. True stress and strain values were implemented in the material model to account for the decrease in cross sectional area and variation in reference length during the analyses. Typically numerical tensile tests are conducted using a more accurate representation of the tensile test specimen. As the goal was only to quantify the difference between the strain rate models, a more rudimental representation of the test specimen was considered adequate.

The resulting strain rates were estimated using the engineering strain rate according to

$$\dot{\varepsilon}_{\text{eng}} = \frac{\mathrm{d}\varepsilon_{\text{eng}}}{\mathrm{d}t} = \frac{\mathrm{d}\left(L - L_0\right)/L_0}{\mathrm{d}t} = \frac{1}{L_0}\frac{\mathrm{d}L}{\mathrm{d}t} = \frac{v}{L_0}, \tag{2.36}$$

where L_0 corresponded to the initial reference element length. The velocity v was determined using the enforced axial displacement Δu, and the corresponding internal step time of the solver Δt_{step} according to

$$v = \frac{\Delta u}{\Delta t_{\text{step}}}. \tag{2.37}$$

For more accurate strain rate results, the true strain rate should have been used. It is defined as

$$\dot{\varepsilon}_{\text{true}} = \frac{\mathrm{d}\dot{\varepsilon}_{\text{true}}}{\mathrm{d}t} = \frac{\mathrm{d}\left[\ln\left(L/L_0\right)\right]}{\mathrm{d}t} = \frac{1}{L}\frac{\mathrm{d}L}{\mathrm{d}t} = \frac{v}{L}, \tag{2.38}$$

where L refers to the current length of the element. The implication of a varying L is that the velocity cannot be constant if the goal is to maintain a constant strain rate.
For tensile tests where the axial velocity is constant, the maximum difference between the true strain rate and engineering strain rate can be obtained by dividing Eq. (2.36) with Eq. (2.38). The result is

$$\left(\frac{\dot{\varepsilon}_{\text{eng}}}{\dot{\varepsilon}_{\text{true}}}\right)_{\text{max}} = \frac{L_{\text{max}}}{L_0}, \quad \text{given that } v = \text{constant}. \tag{2.39}$$

The engineering strain rates used in the numerical tests are shown in Table 5, and the resulting stress-strain curves from the numerical tensile tests are shown in Figure 9 to Figure 12.

Table 5. Parameters for the numerical tensile tests, and the corresponding strain rates.

Initial element length L_0 [m]	Size of forced axial displacement Δu [m]	Solver step time Δt_{step} [s]	Engineering strain rate [1/s]
1	0.1	1000	0.0001
1	0.1	0.1	1
1	0.1	0.01	10
1	0.1	0.0001	1000

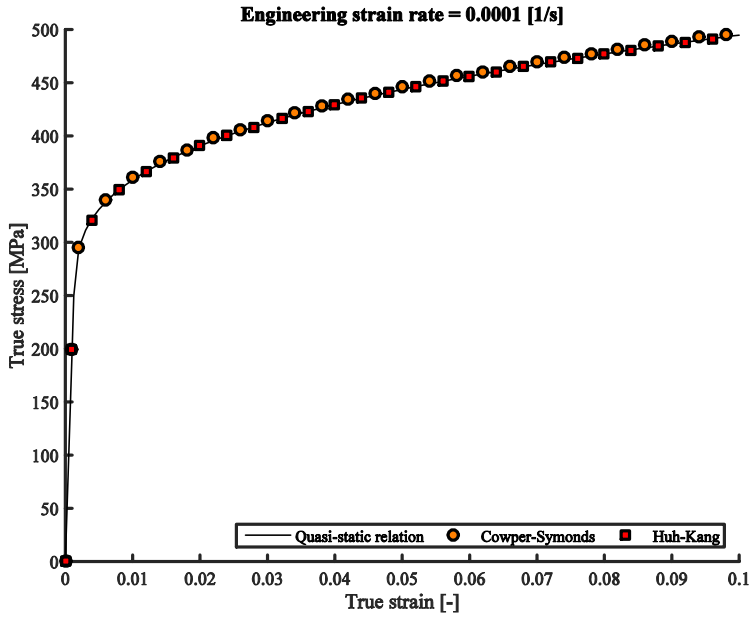

Figure 9. Numerical predictions corresponding to a quasi-static strain rate.

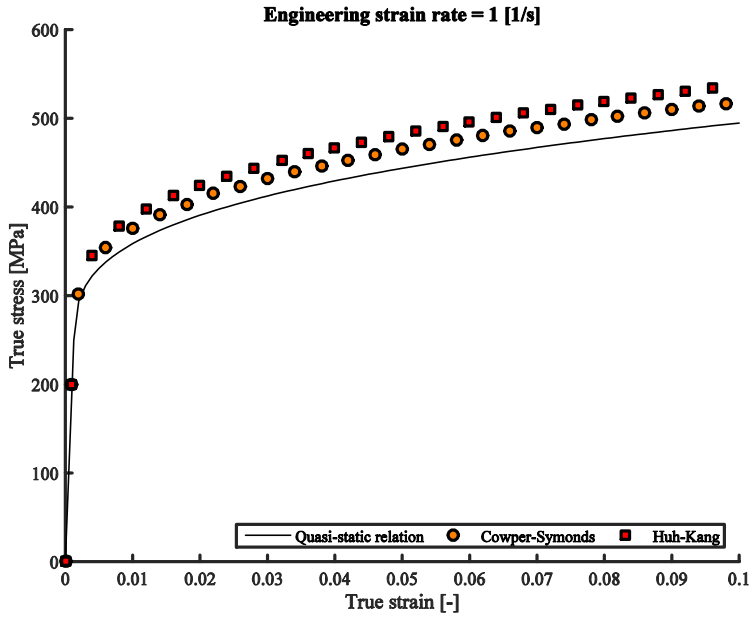

Figure 10. Numerical predictions corresponding to a low strain rate.

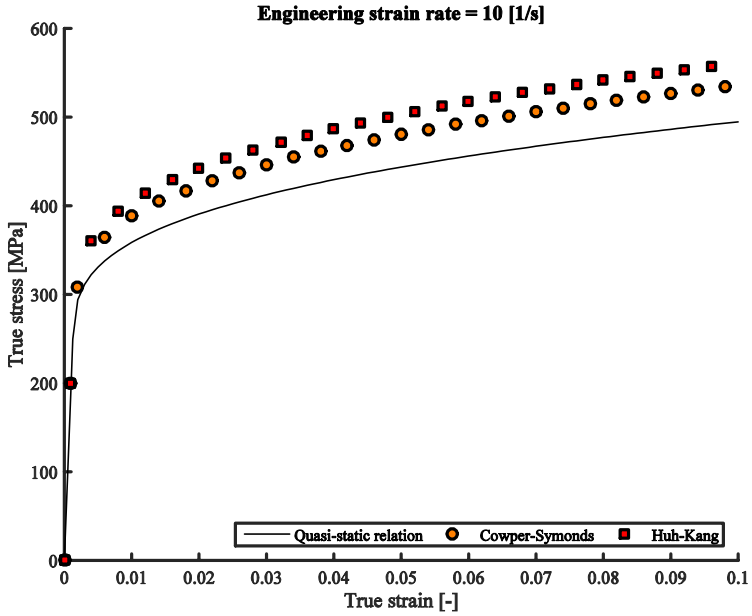

Figure 11. Numerical predictions corresponding to a medium strain rate.

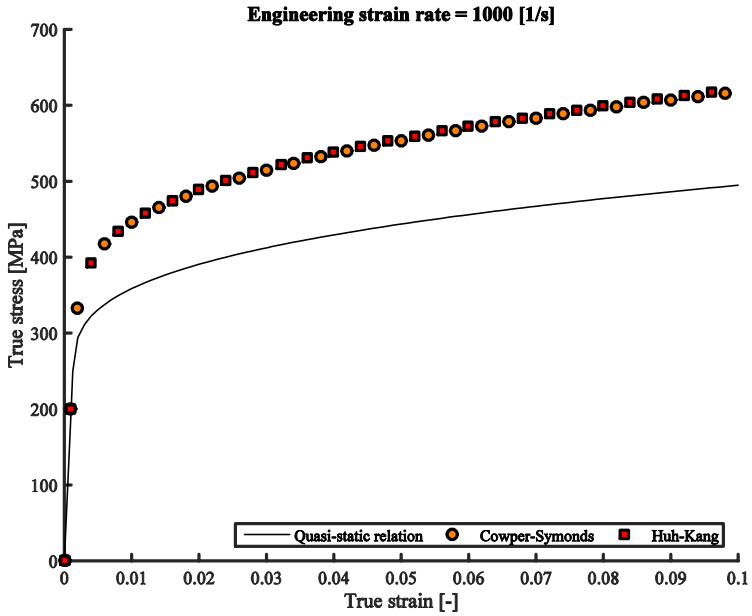

Figure 12. Numerical predictions corresponding to a high strain rate.

Based on the results, both models reproduce the quasi-static stress-strain curve for small strain rates. The result is expected and verifies to some extent that that the parameters are correct. Confidence that the models were implemented correctly in the software was also gained. For low to moderate strain rates, the Huh-Kang model generates larger stress values compared to the Cowper-Symonds relation. As the engineering strain rate increases further, the models converge to predict equivalent results.

High strain-rates are reflected in higher yield stresses compared to quasi-static estimates. In relation to arc blasts, the implication is then that cabinet deformations predicted

without taking into account strain-rate effects remain larger than true deformations, because force balance between internal stresses and external forces requires larger strains to be satisfied. Furthermore, the deformations predicted using the Huh-Kang model should be smaller compared to deformations obtained using the Cowper-Symonds relation.

Strain rate parameters for materials used in electrical switchgears are often unknown. Neglecting the strain rate effects should therefore generally yield more conservative predictions for the deformation. This outcome is desired from a design safety perspective. Strain-rate effects should therefore be disregarded if good data is not available for determining model parameters. Inaccurate parameters might provide a false sense of security in the design.

The validity of the apparent increase in ultimate strength visible in Figure 9 to Figure 12 should be questioned. According to Boyce et al. (2007) the increase in ultimate tensile strength as the strain rate is increased is only minor. Similar results were obtained by Health & Safety Executive (1999), where the ultimate tensile strength was found to be insensitive to the strain rate. The numerical stress-strain curves should therefore be analyzed with extreme caution once the true stress grows beyond the quasi-static ultimate tensile strength.

Although the results in Figure 9 to Figure 12 are not necessarily valid when the stress grows beyond the ultimate strength, the numerical tensile tests still illustrate the relative difference between the Cowper-Symonds and Huh-Kang models successfully. The maximum difference between the engineering strain rate and the true strain rate can be estimated from Eq. (2.39) and Table 5 as 10 %.

6 Addressing uncertainty

Uncertainty is always present due to underlying variation found in nature. Commonly the scatter is not taken into account in computational models however, because the variation is deemed insignificant. Generally then, input parameters are given specific values, which yield deterministic results in terms of stresses and displacements. One can certainly question the validity of these results if considerable scatter is known to be present in the input variables.

Based on findings by Wu et al. (2005), the arc voltage in low-voltage alternating current system varies stochastically as shown in Figure 13, implying that an exact formula for the arc power is unfeasible. The variation in arc power causes variation in the pressure load, which is ultimately reflected as uncertainty in the structural response. An example computation estimating the bounds for the arc power for various arc lengths is shown in Figure 14.

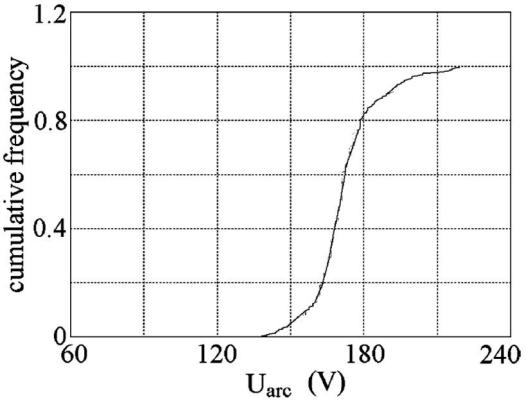

Figure 13. Cumulative frequency of arc voltage determined by Wu et al. (2005).

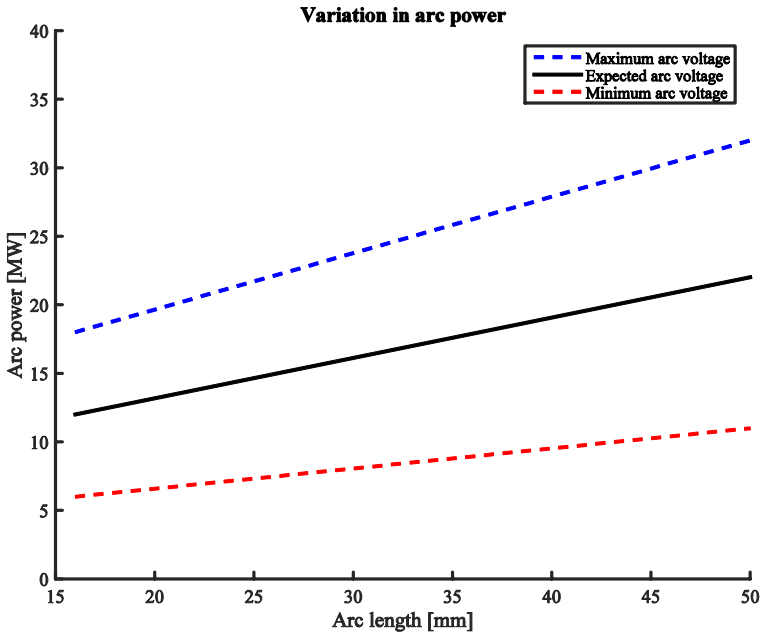

Figure 14. Arc power bounds due to variation in arc voltage, computed for various arc lengths.

In relation to arc flashes the matter is complicated further. The random re-ignition of arcs is difficult to control, and can affect the pressure buildup greatly. Similar issues are present with the issue of uncontrollable arc burn-through presented in Section 1.3. Addressing the matters reliably through predictive simulation is currently unfeasible. Instead, good design principles should be employed to attempt to work around the problems. By minimizing the initial arc length, the released energy decreases as shown in Figure 14. Shorter arcs are also less prone to jump, which aids in preventing the arc burn-through phenomenon. By minimizing the Lorentz force acting on the arc, the problem of undesired arc movement can be addressed to some extent with reasonable computational effort.

The large uncertainty present makes the dimensioning of enclosures difficult. Conventionally worst-case scenarios are used to ensure the safety of designs. The largest estimate for the arc power is then used in combination with a conservative estimate for the amount of energy absorbed by the surrounding gas, to obtain the pressure load. The approach is partly criticized in this thesis, because it does not take into account the likelihood of occurrence of the different events. One can question if it is appropriate to dimension a structure according to a worst-case scenario, if the corresponding likelihood is tiny compared to an event considerably less severe.

The uncertainty in input variables can be accounted for with a concept called probabilistic design, and represents one of the key concepts in this thesis. The approach has seen most success in the aerospace and nuclear sectors, where reliability is of great concern. An introduction to the topic is presented for instance by Sundararajan (1995).

6.1 Monte Carlo simulations

In probabilistic design, input parameters of interest are assumed to follow known probability distributions instead of being assigned deterministic values. A sample design is created by performing draws from each probability distribution, and assigning the values to the corresponding input variables. Usually Random, or Latin hypercube – sampling is used. For an in-depth comparison of the sampling methods, the reader is encouraged to familiarize with the work of McKay et al. (1979). The simulation is then run and the corresponding output values of interest are recorded. In arc flash events the maximum von Mises stress and the failure parameter presented in Section 5.3 are generally most important to the analyst. Results from particular simulations are usually not of importance, as they only represent individual samples. The power in the procedure becomes apparent when the process is repeated rigorously multiple times.

By repeating the procedure numerous times and analyzing the output results, it is possible to understand what the expected system response is, and how large the scatter in the output variables is. The obtained information is more reliable than the output results from a single deterministic analysis, because the likelihood of different scenarios are taken into account.

Figure 15 illustrates the principal result of a Monte Carlo simulation in relation to an arc flash simulation. The red distribution corresponds to the maximum equivalent plastic strain present in a structure due to the pressure load. It is created by fitting a probability

distribution to the histogram obtained from the computations. The histogram is created by recording the maximum equivalent plastic strain present in the structure for each individual sample simulation.

The variation in the pressure load is mainly caused by the variation in arc voltage according to Figure 13. A great amount of scatter is also caused by uncertainty in the thermal transfer coefficient if a more rudimental approach is used for the pressure rise. The probability density function corresponding to the arc voltage in Figure 13 is approximately normal, implying that estimates for the expected value and standard deviation are readily available. Estimates for the variation in the thermal transfer coefficient were not found in the literature, and represents an interesting future research topic. A conservative approach is to assume that the k_p fraction can deviate from the estimate uniformly by 0.2, based on approximations for the k_p value presented by Anantavanich (2010, p. 13). The approach is not strictly speaking valid as the variation stems from various different experiments, not from the repetition of a single setup. In lack of better information it represents the best approximation available, however. If more advanced representations are used for the fraction of arc energy transferred to the gas, the uncertainty decreases to some extent. The structural parameters affecting the maximum equivalent plastic strain the most due to the blast loading were not found in the literature, and represents a research question to be answered by this thesis.

The green distribution in Figure 15 represents the probability density function of the fracture strain of the structure, and is readily available from experimental data obtained from tensile tests. Other definitions for the strength of the structure could naturally be used. For instance, the yield stress could be used if the expected overpressure is very low. The effect of altering the definition for the strength of the cabinet is mainly seen as a shift of the green distribution along the horizontal axis. When altering the definition of the strength, the definition of the load has to be modified accordingly.

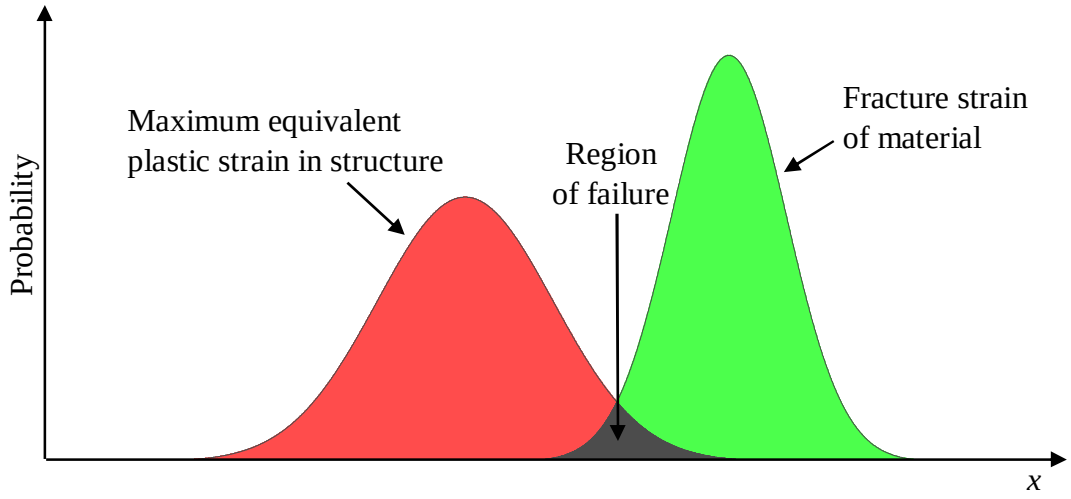

Figure 15. Expected result of a Monte Carlo simulation in an arc flash event. The meaning of the variable x is illustrated in Eq. (2.40).

The region where the two distributions overlap clearly indicates a region of failure. By adapting the definition of probability of failure as defined by Ang and Tang (1984, p. 335) to arc blast events the result is

$$p_{\mathrm{F}} = \int_0^{\infty} \left[1 - F_{\mathrm{Y}}\left(x\right)\right] f_{\mathrm{X}}\left(x\right) \mathrm{d}x, \tag{2.40}$$

where F_{Y} is the cumulative probability distribution of the maximum equivalent plastic strain in the structure, and f_{X} is the probability density function of fracture strain. The definition in Eq. (2.40) offers a direct dimensioning principle for structures under arc blast loading, by requiring that the probability of failure has to be below some predefined threshold value.

7 Results and analysis

In this chapter, computational results relating to the structural response in arc flash events are presented. First, strain rate effects on the material behavior are quantified in typical arc flash events. The computational tools presented in Chapter 2 for estimating the pressure load are then adapted for a compact enclosure, and the structural response is determined. The predicted deformations are compared to measured deformations from a comparable arc flash test to validate the approach. Finally, the implications of adapting the probabilistic approach presented in Section 6.1 is adapted to the enclosure.

7.1 Strain rate effects in typical arc flash events

Section 5.4 provided an in-depth investigation on how strain rate effects can be taken into account in the structural analysis. The Cowper-Symonds and Huh-Kang models were next applied to several benchmark cases, to evaluate the effects in typical arc flash conditions. The focus was on comparing the maximum central node displacement to the rate independent material model in order to determine if the stiffening effect of the material was serious. The material was chosen as A36 steel to be in-line with the previous investigation on strain rate models. All computations were carried out using the explicit solver in ABAQUS® (2015a), as it was straightforward to implement the Huh-Kang strain rate model in the software. The mathematical theory governing the explicit solver in is carefully documented in ABAQUS® (2015b).

Two plate sizes were investigated as shown in Figure 16. The dimensions were chosen based on typical values in the lower and upper end of the switchgear size spectrum. All edges of the plates were fixed, as rotation around the edges is usually prevented. Three plate thicknesses were investigated for each plate size.

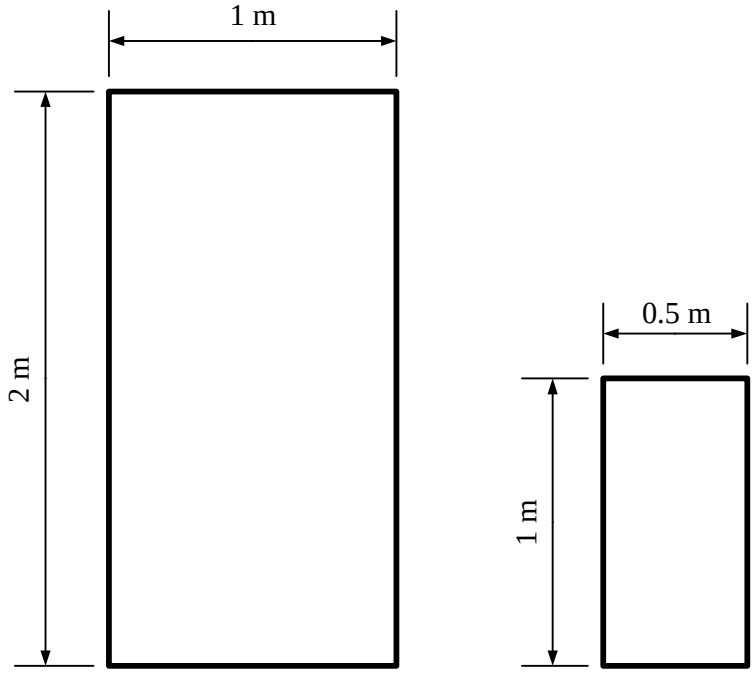

Figure 16. Dimensions of the plates used in the numerical computations.

Damping was neglected in the analysis to produce conservative estimates for the rate-dependent effects. As shown in Figure 7, the addition of damping decreases the rate of deformation to some extent. Rayleigh damping also depends on the eigenfrequencies of the plates according to Eq. (2.20). Comparing the results between different plate thicknesses with added damping then becomes a cumbersome issue, although the numerical implementation itself is straightforward.

All arc blasts were modeled as triangular pressure pulses, which was considered a reasonable simplification based on the pressure load shown in Figure 4. Three pressure rise times corresponding to two peak pressures were investigated based on typical values found in the report by Uzelac et al. (2011). Equivalent load durations were used to ensure that the impulse remained constant for each class of overpressures. The resulting loads are shown in Figure 17.

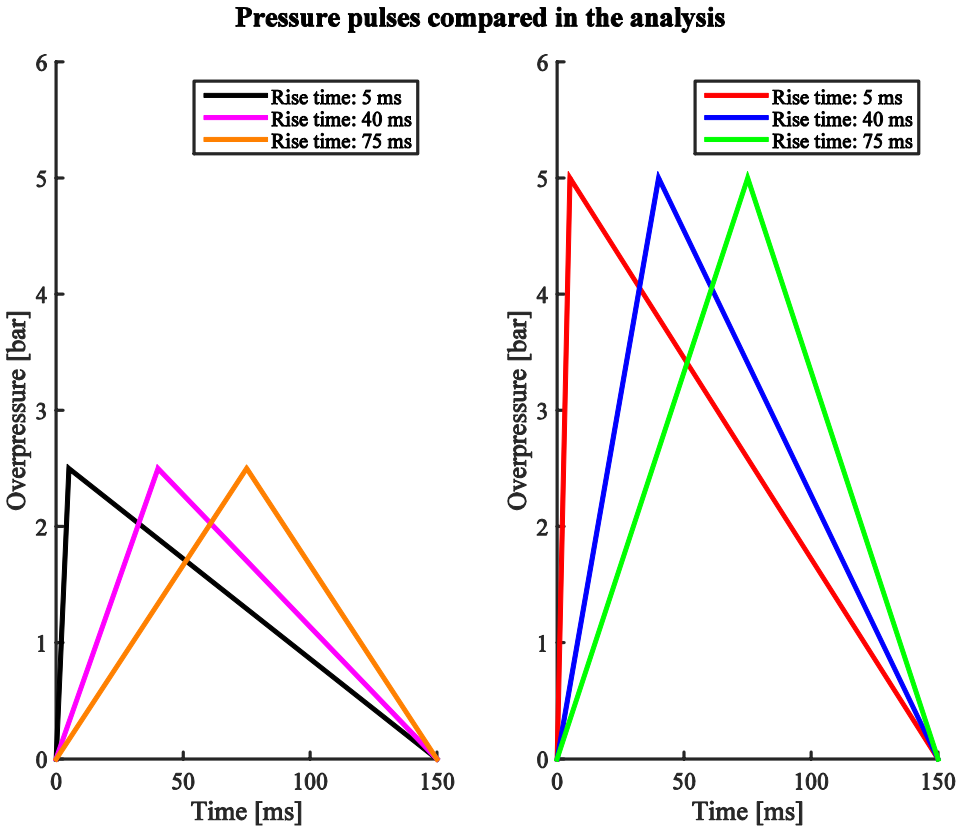

Figure 17. Pressure loads employed in the analysis. The use of an equivalent end time ensured that the impulse remained constant for each class of overpressures.

The results from the computations are shown in Figure 18 to Figure 21, where CS and HK refer to the maximum central node displacement predicted using the Cowper-Symonds and Huh-Kang relations, respectively. RI represents the corresponding rate independent prediction.

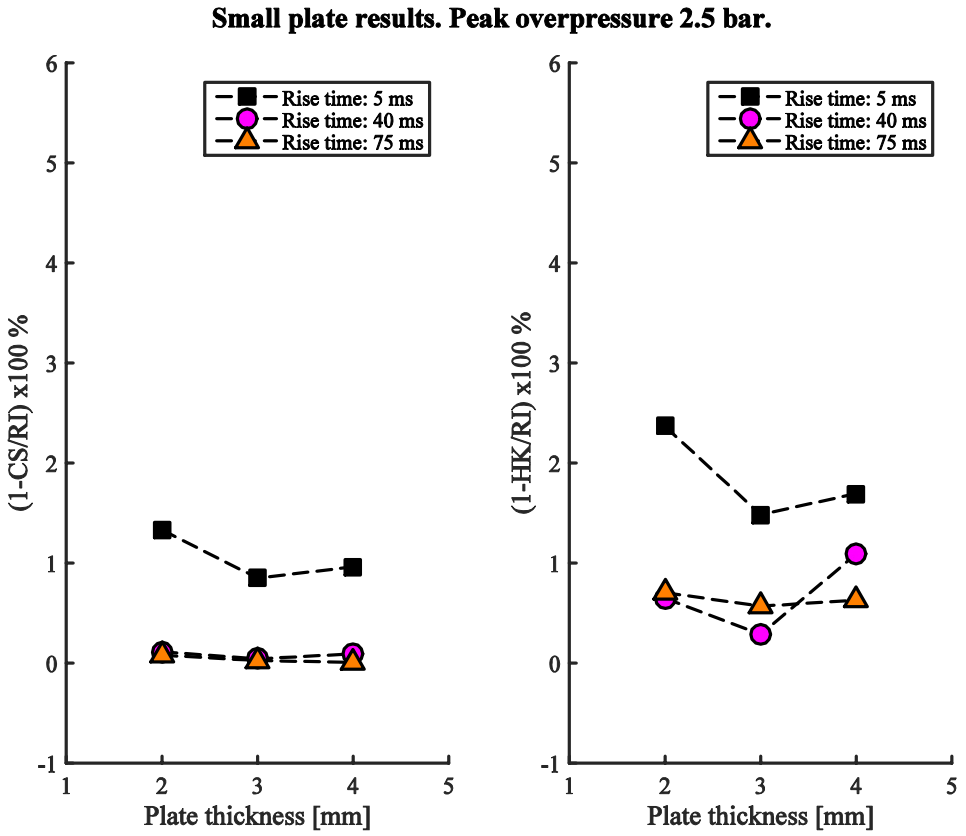

Figure 18. Results corresponding to the smaller plate and lower peak pressure.

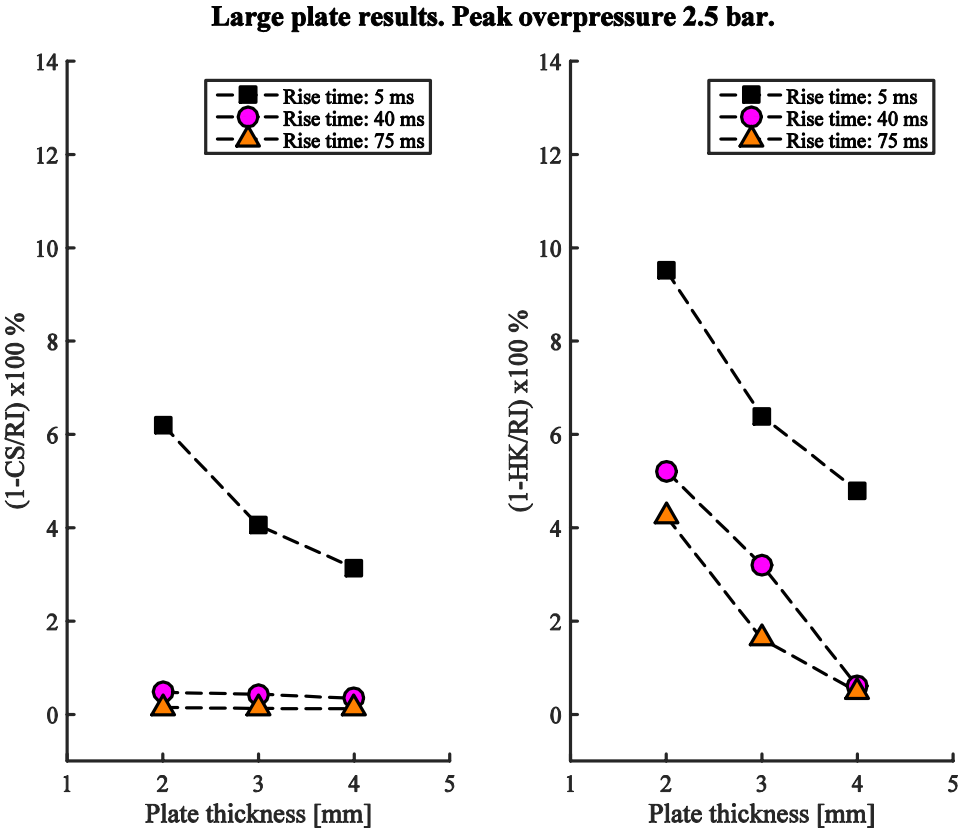

Figure 19. Results corresponding to the larger plate and lower peak pressure.

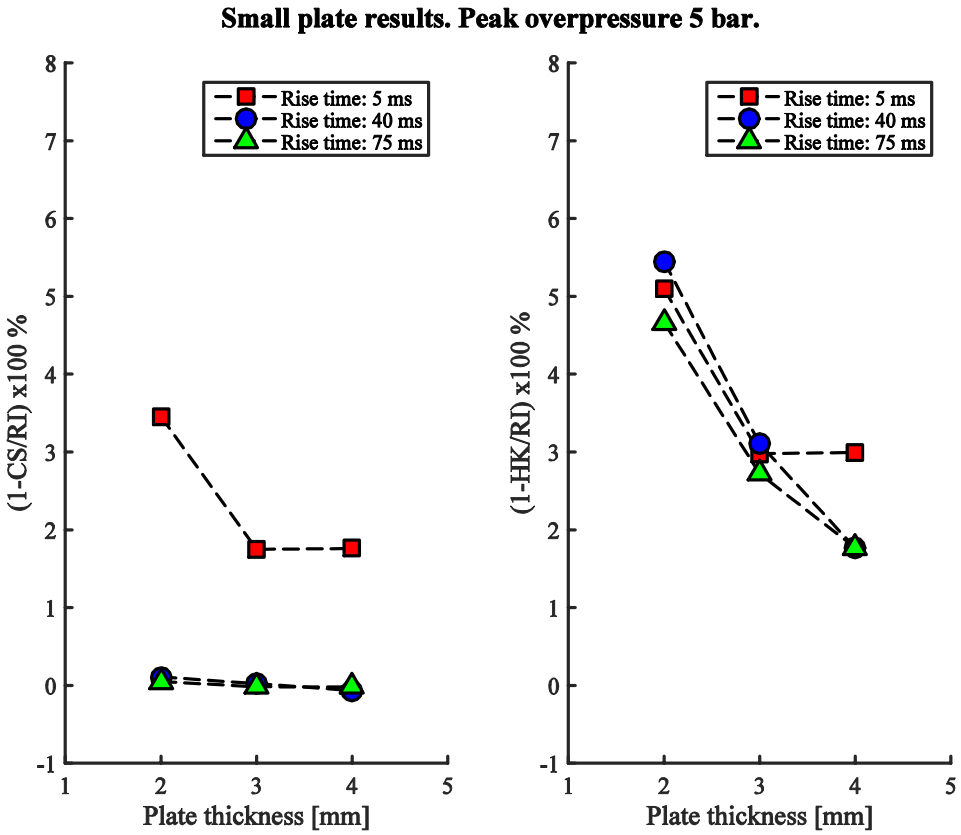

Figure 20. Results corresponding to the smaller plate and higher peak pressure.

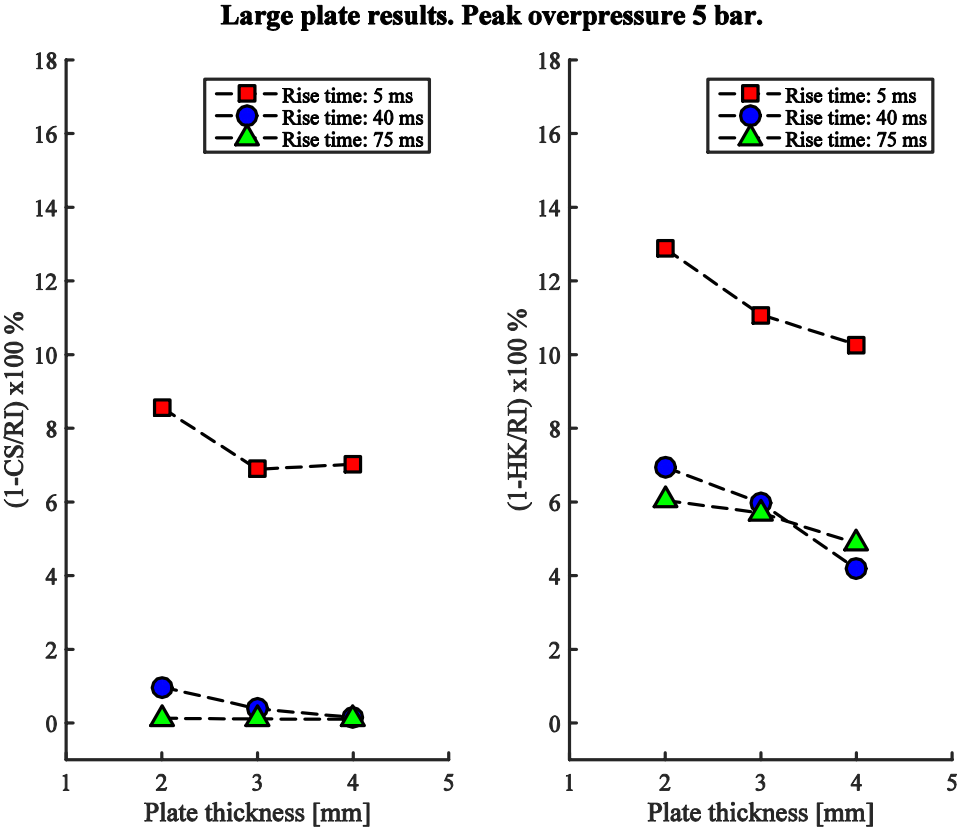

Figure 21. Results corresponding to the larger plate and higher peak pressure.

By inspecting the results it is evident that the rate independent material model predicts larger deformations compared to the rate dependent material models. The result occurs because the yield stress grows as the strain rate increases, as confirmed in Section 5.4. To conserve the momentum, a lower strain state is required when the rate dependent effects are taken into account. The lower strain state is in turn reflected in smaller deformations.

The Huh-Kang model stiffens the plates more than the Cowper-Symonds model, as the percentage difference to the rate independent model is constantly smaller for the Cowper-Symonds model. The result is expected, and follows from the larger increase in yield stress predicted by the Huh-Kang model compared to the Cowper-Symonds model for low to medium strain rates, as shown in Section 5.4.3.

As the plate thickness decreases, the relative importance of taking into account strain rate dependency increases. The result can most likely be attributed to the correlating decrease in inertia, which implies that the plates deform more as they are less capable of resisting the impulse load. Unfortunately the conclusion is not foolproof, as the relative importance of taking into account strain rate effects grows for the smaller plate and lower peak pressure, as the plate thickness increases. The same phenomenon was visible for both strain rate models. The counterintuitive result is likely explained by an eigenfrequency of the plate being close to the corresponding rate of loading for the corresponding setup. In turn, the deformations increase and thus the relative importance of taking into account strain rate effects becomes more crucial.

Strain rate effects become more influential as the plate size increases. The result occurs because larger plates are more prone to deform compared to smaller plates, as the edges are further apart.

The rise time also affects the results greatly. In fact, the Cowper-Symonds shows little to no effect of taking strain rate effects into account for pressure rise times of 40 milliseconds and higher. The effects become noticeable for slower pressure rise times when utilizing the Huh-Kang model. As the pressure increases, the relative importance of taking into account strain rate effects becomes more important, as the corresponding deformations grow larger.

When strain rate effects are taken into account in the computational model, the decrease in deformation implies that the equivalent plastic strain also decreases. The phenomenon was confirmed for the setup in which the largest relative difference was obtained between the central node displacements, seen in Figure 21 as roughly 13 %. The maximum equivalent plastic strain was found to drop from 0.04 to 0.03 when the Huh-Kang model was applied to the rate independent case.

All analyses were conducted using 4 noded, first-order reduced-integration elements denoted by S4R in ABAQUS® (2015a). The maximum equivalent plastic strain rate was computed by averaging the equivalent plastic strain rates at the respective integration points of the four elements connected to the central node. The computation produced an estimate for the maximum strain rate in the analyses as roughly 15 1/s. The maximum

equivalent plastic strain of 0.04 was smaller than the plastic strain corresponding to the ultimate strength of roughly 0.05 at the corresponding strain rate. Hence, confidence was obtained that no material failure took place.

In order to determine the mesh convergence of the solution, the maximum difference between the averaged von Mises stress and the unaveraged von Mises stress were compared at the central node. During the analysis time of 150 ms the difference was always less than 0.75 %, implying that sufficient convergence was achieved with the meshes used.

When performing computations using reduced integration elements in dynamic loading events, it is important to verify that zero-energy modes associated with hourglassing is negligible. For the analyses performed in this thesis the problem was not visible, however. This was confirmed partly by visually inspecting the deformed plates, and partly by confirming that the rate of artificial strain energy to the total energy of the system always remained less than one percent.

For an industry level design where the plates are fastened to the cabinet using screws, a thorough investigation into the stress levels at the fasteners would have to be conducted. Cabinet plates are can be found to separate from the cabinet if fastened improperly. As the goal of this analysis was only to quantify the strain rate effects, the correct modeling of fasteners was disregarded.

7.2 Example study of a realistic enclosure

The methods presented in this thesis were applied to a simplified enclosure geometry to estimate the structural response in an arc flash event, after which the results were compared to measured deformations from an analogous arc flash test. Both methods presented in this thesis used to estimate the pressure load were first applied deterministically. The implications of applying the probabilistic dimensioning approach presented in Section 6.1 was finally examined.

7.2.1 Problem setup

The enclosure used in the computations is shown in Figure 22, which was completely airtight apart from the opening where the relief disc was attached. The disc was fastened to structure using a spring mechanism. The opening pressure was known in advance. All corners of the backside were fixed in the arc flash test, and immediately yielded the appropriate boundary condition for the structural simulation.

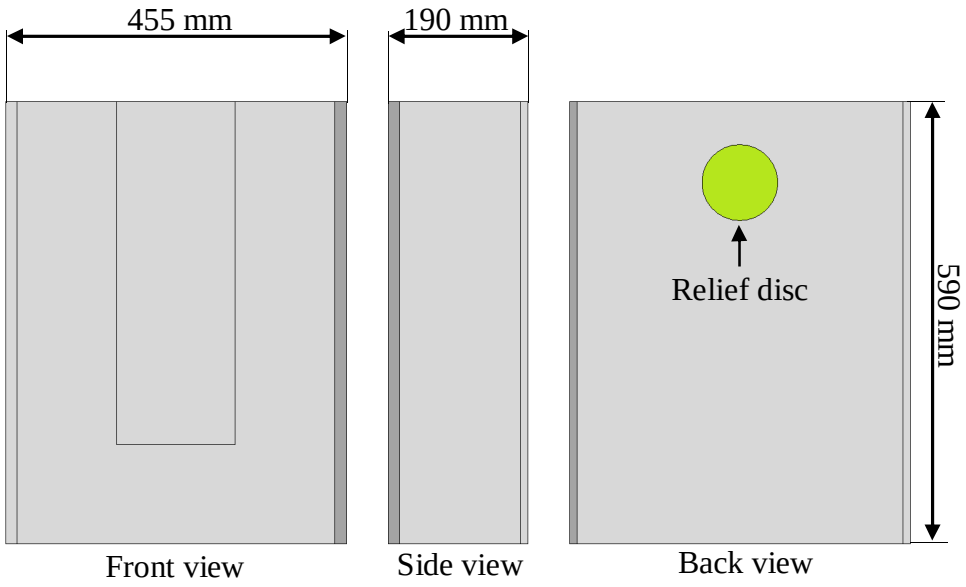

Figure 22. Simplified enclosure geometry used in the simulations.

The enclosure was built from AlSi10Mg through sand casting, and was not heat treated in any way. Mechanical properties for the alloy were obtained from Hydro (2015). Averaged material values computed from the lower and upper bounds were used for all properties. A bilinear isotropic material model was used.

Strain rate parameters for AlSi10Mg were not found in the literature. The corresponding parameters for aluminum as determined by Bodner and Symonds (1962) where used instead, as 85 % of the alloy mass composition consisted of aluminum. The Huh-Kang parameters were not found in the literature. The mechanical properties of the enclosure are shown in *Table 6*.

Table 6. Structural parameters used in the simulations.

Parameter	Value	Unit
Material	AlSi10Mg	N/A
Enclosure thickness	6	mm
Density	2680	kg/m^3
Young's modulus	74	GPa
Poisson's ratio	0.3	N/A
Yield stress (R_p = 0.2 %)	110	MPa
Ultimate tensile strength	185	MPa
Fracture strain	4	%
Tangent modulus	1.875	GPa
Cowper-Symonds parameter *C*	6500	1/s
Cowper-Symonds parameter *P*	4	N/A

The arc power was determined using the measured current and phase-to-earth voltage from the arc flash test. Strictly speaking the true arc voltage is always slightly lower than the measured voltage due to electrical resistance, but the difference is generally sufficiently small for the effects to be neglected. The measured current and voltage are shown in Figure 23.

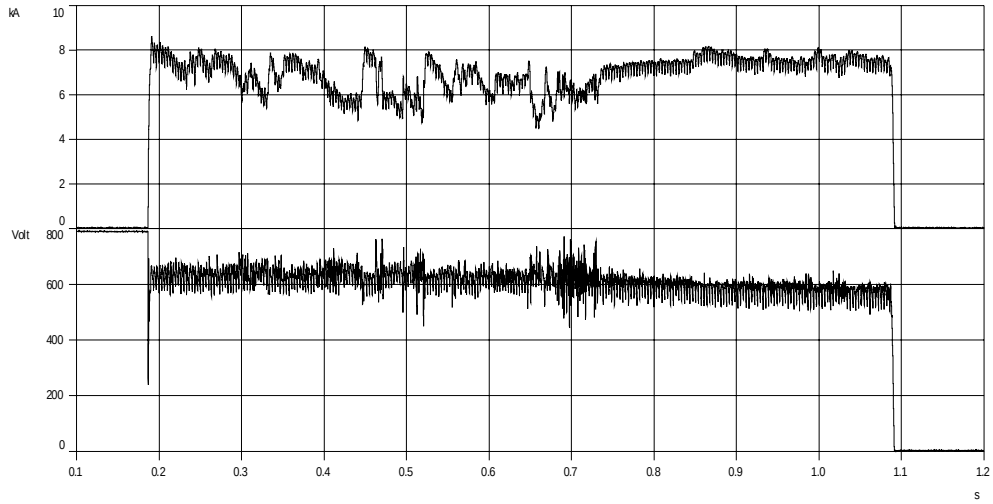

Figure 23. Measured current and voltage from the arc flash test, used to determine the arc power.

The arc power was computed as

$$P_{\text{el}} = UI = 650\,\text{V} \cdot 7\,\text{kA} = 4.55\ \text{MW}, \tag{2.41}$$

where U was the average measured voltage and I the average measured current during the initial 100 milliseconds, which was the time duration of most interest in the blast analysis. As mentioned in Section 5.2, the peak overpressure is generally observed several magnitudes in time before the arc is extinguished. Should the arc power be computed by averaging the values during the complete arc burn duration, the visible drop in the voltage shown in Figure 23 implies that the estimated arc power would have been significantly smaller than the true arc power during the time period of interest.

The SCM was first utilized to obtain the corresponding pressure rise based on the estimated arc power, after which the CFD method was employed. Two approaches were compared regarding the approach based on the SCM. First, the energy was assumed to discharge homogenously in the complete gas volume, which yielded a similar pressure distribution everywhere. The principle of chaining volumes was then applied as presented in Section 2.2.3, to resolve some spatial differences in the pressure distribution.

7.2.2 Pressure load results using the SCM

The amount of heat transferred from the arc to the air was estimated according to the enthalpy based approach presented by Becerra and Ostrowski (2014). The SCM presented in Section 2.2 was then applied to obtain the pressure rise in the enclosure. Two approaches for describing the arc volume were investigated as shown in Figure 24. In

relation to the second approach, the gas was only able to pass through the fluid volumes through the upper part in the enclosure.

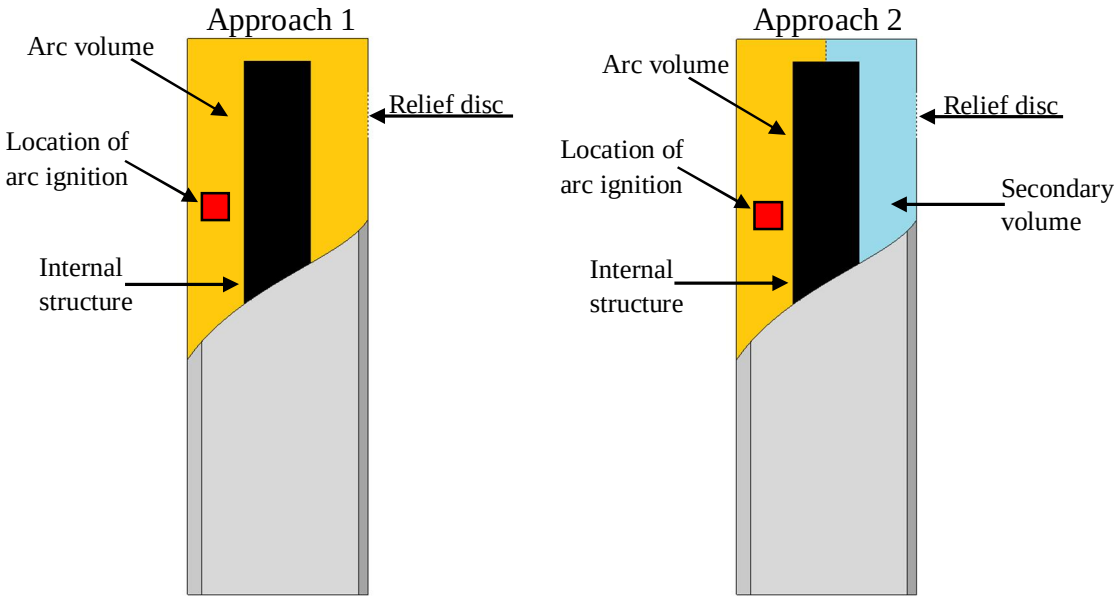

Figure 24. The two approaches used in relation to the SCM. Electrical components fastened to the internal structure were taken into account when estimating the fluid volume, although not visible in the figure.

The corresponding problem setups are visualized in Figure 25. The relief disc opening overpressure had previously been verified as 0.2 bar, with the corresponding opening area determined as $A_r = 0.003$ m^2. The discharge coefficient was set to $\alpha = 1$ as more accurate data was not available. The initial temperature and pressure in all fluid volumes was assumed to be 25 °C and 1 bar respectively. The opening area connecting the fluid volumes together in the second approach was sufficiently small for the results to be valid, as required in Section 2.2.2.

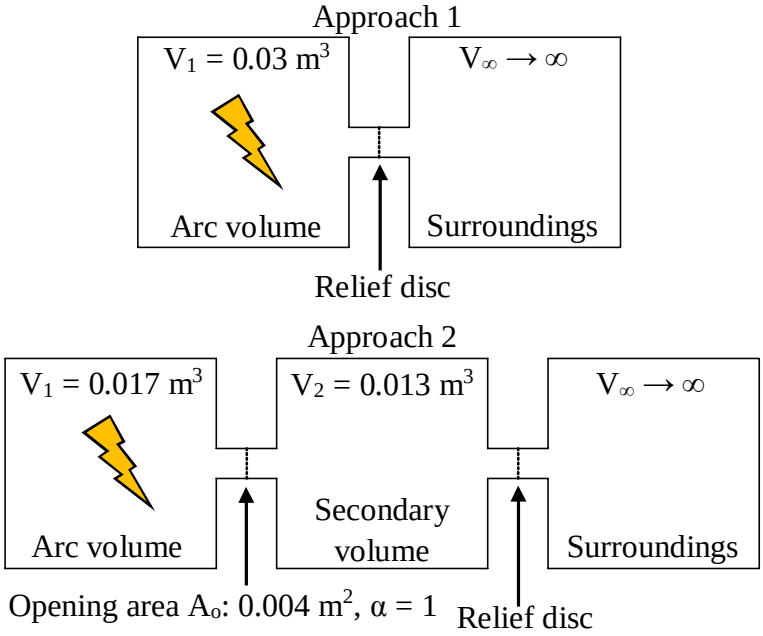

Figure 25. Schematic setup of arc pressure computation using the SCM.

The results from the pressure computations are shown in Figure 26, and summarized in Table 7.

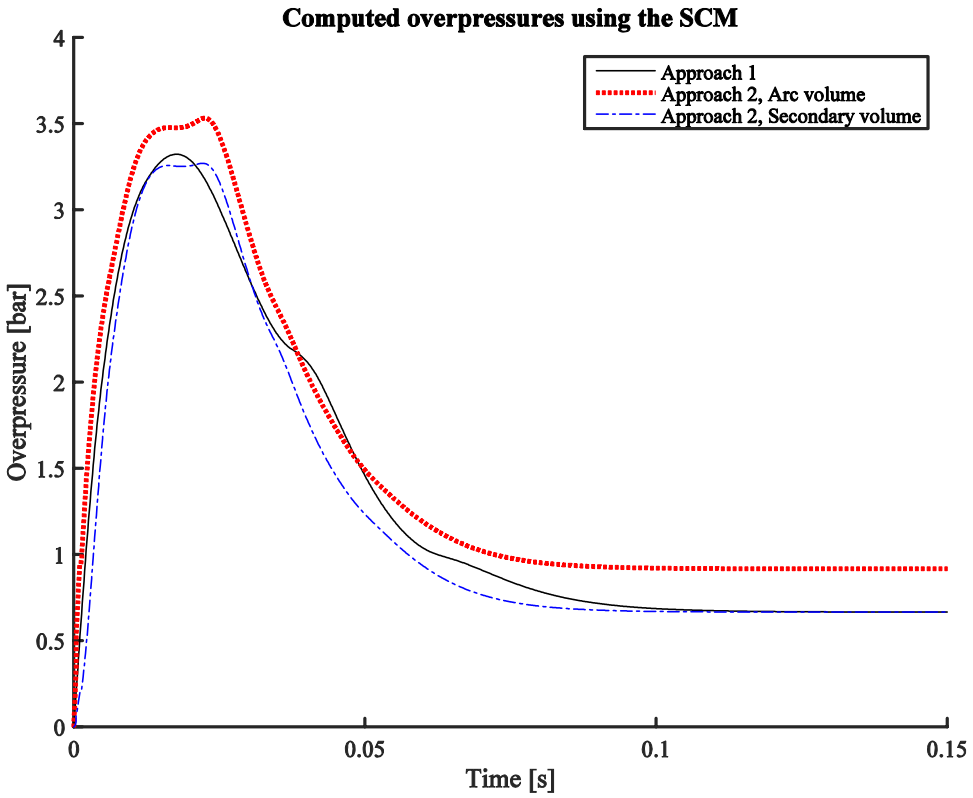

Figure 26. Computed overpressures in the enclosure using the SCM.

Table 7. Summarized results obtained using the SCM for the two compared approaches.

Approach	Volume	Peak overpressure [bar]	Time [s]
1	Arc volume	3.32	0.0176
2	Arc volume	3.53	0.0225
2	Secondary volume	3.27	0.0221

By assuming that the arc energy is released in a smaller fluid volume, the corresponding overpressure increases. The difference between the computed overpressures obtained using the second approach are small, however, and can be explained by the separate terms present in Eq. (2.6). The large cross-sectional area connecting the volumes combined with a large discharge coefficient, suggest that the mass flow through the opening is large. As the secondary fluid volume is small, the corresponding pressure rise is hasty. Generally larger pressure differences are obtained if the secondary volume is larger compared to the arc volume, and if the opening connecting the volumes is smaller.

The simulation results can generally be assumed valid until the air temperature grows beyond 6000 K, after which significant dissociation begins to take place in the molecules. For the computational results presented in this thesis, the temperature did not exceed the limit until after the pressure peaks had been observed. In relation to the blast analysis, the time period of interest is short in duration, and hence the effects of dissociation can often be neglected.

The apparent steady state pressures visible in Figure 26 arise because the computational estimates for the evaporated electrode material and the temperature increase of the remaining gas, increases the pressure at a rate which is compensated by the volumetric outflow of the gas. When analyzing the enclosure response to the blast load, the steady state is generally of no interest.

When analyzing the structural response, the pressure was assumed to drop linearly to zero at after the pressure peaks were obtained. The apparent steady-state pressure value shown in Figure 26 accounted for elastic deformations only, and was neglected in the analysis in order to observe the final deformed state of the enclosure.

7.2.3 Pressure load results using CFD

A simplified CFD solution was set up using the CFX transient flow solver in ANSYS (2015a). The k_p approach was used, as it was not in the scope of this thesis to attempt to implement the full modifications to the set of equations governing fluid flow discussed in Section 2.3.

The ideal gas law was used for the equations for state and enthalpy, as real gas data was not available. Only the energy equation discussed in Section 2.3.3 was modified to take into account the energy released by the arc. Turbulence effects were modeled with the standard k-ε approach discussed in Section 2.3.5. The advection scheme was set to high resolution, and the transient scheme was solved with the second order accuracy using the backward Euler –method. Turbulence numerics were solved with first order accuracy.

The fluid volume was extracted from the simplified enclosure shown in Figure 22. A cone shaped exhaust volume was added to the model to promote convergence due to the small size of the enclosure fluid volume. Without the exhaust volume the relief disc opening would have had to be assigned an outlet boundary condition corresponding to the atmospheric conditions directly. Enforcing a specific flow condition close to the arc volume where high temperatures and pressures were present was assumed to possibly cause a diverging solution. By adding the exhaust volume the flow was able to penetrate the relief disc opening freely. An atmospheric outlet boundary condition was assigned to the surface of the exhaust volume, and the solid interfaces were given a no-slip boundary condition. In total 482628 volume elements were used. Inflation layers were added at the solid boundaries to resolve the gradients more accurately. The extracted fluid volume from the cabinet is shown in Figure 27 along with the corresponding meshed model.

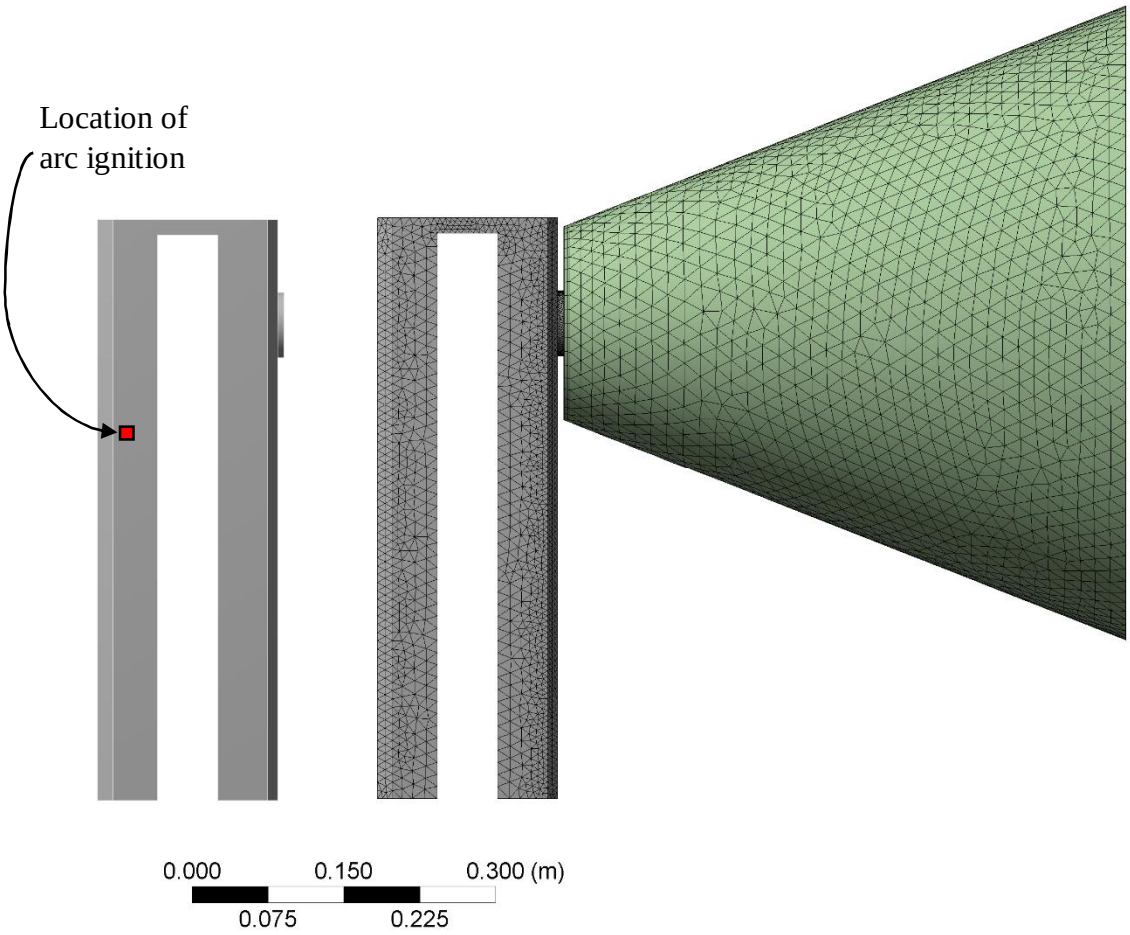

Figure 27. Extracted fluid volume on the left, and final meshed model with the added exhaust volume on the right.

The simplified k_p approach was used to estimate the thermal power. Implementing the full modifications to Eq. (2.9) and Eq. (2.10) would have required extensive further research not in the scope of this study. According to Anantavanich (2010, p. 13), k_p usually ranges between 0.4-0.65 for copper electrodes. Three analyses were performed by implementing the lower, upper and averaged value for the thermal transfer coefficient in turn.

The corresponding thermal powers were computed using Eq. (2.41) and the data provided by Anantavanich (2010, p. 13) as

$$\begin{aligned} P_{\text{therm,min.}} &= k_{\text{p,min.}} \cdot P_{\text{el}} = 0.4 \cdot 4.55\ \text{MW} = 1.82\ \text{MW} \\ P_{\text{therm,ave.}} &= k_{\text{p,ave.}} \cdot P_{\text{el}} = 0.525 \cdot 4.55\ \text{MW} = 2.39\ \text{MW} \\ P_{\text{therm,max.}} &= k_{\text{p,max.}} \cdot P_{\text{el}} = 0.65 \cdot 4.55\ \text{MW} = 2.96\ \text{MW}. \end{aligned} \tag{2.42}$$

The thermal powers were set to decrease to zero at 0.1 s when the peak overpressure was obtained. Maintaining a constant thermal transfer coefficient would not have described the physics of the arc flash event accurately, in accordance with the discussion presented in Section 2.1. As only the peak overpressure was of interest when analyzing the

structural response to the blast load, it was unnecessary to model the fluid behavior during the complete arc flash event.

The arc was assumed to discharge energy in the complete fluid volume. Computational models where the arc volume is modeled as a subvolume of the total fluid volume usually correspond to cases where the fluid volume is large. The enclosure gas volume investigated in this thesis was tiny. For small fluid volumes the overpressure front engulfs the complete volume almost instantaneously, which makes the simplification valid. By assuming that the energy is discharged in the complete fluid volume, a converging solution is also obtained with higher certainty.

Figure 28 illustrates the resulting pressure distribution in the fluid volume at two different instances of time, for the simulation corresponding to the averaged thermal transfer coefficient. Only small spatial variability in the overpressure was detected when analyzing the results. The averaged pressure distributions at the front and back surface of the enclosure are compared to the resulting pressure loads obtained using the SCM in Figure 29 and Figure 30, and summarized in Table 8.

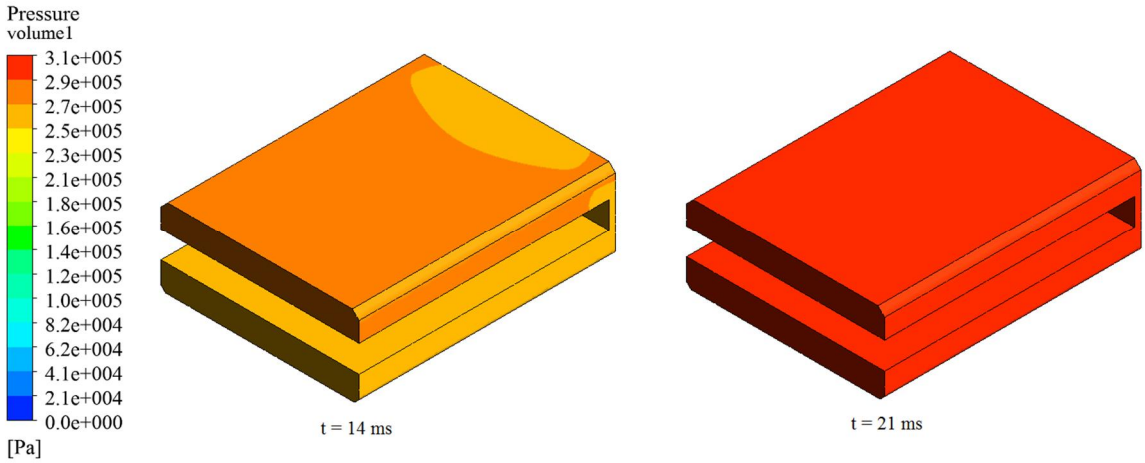

Figure 28. Obtained pressure distributions at two points in time for $k_{p,ave}$.

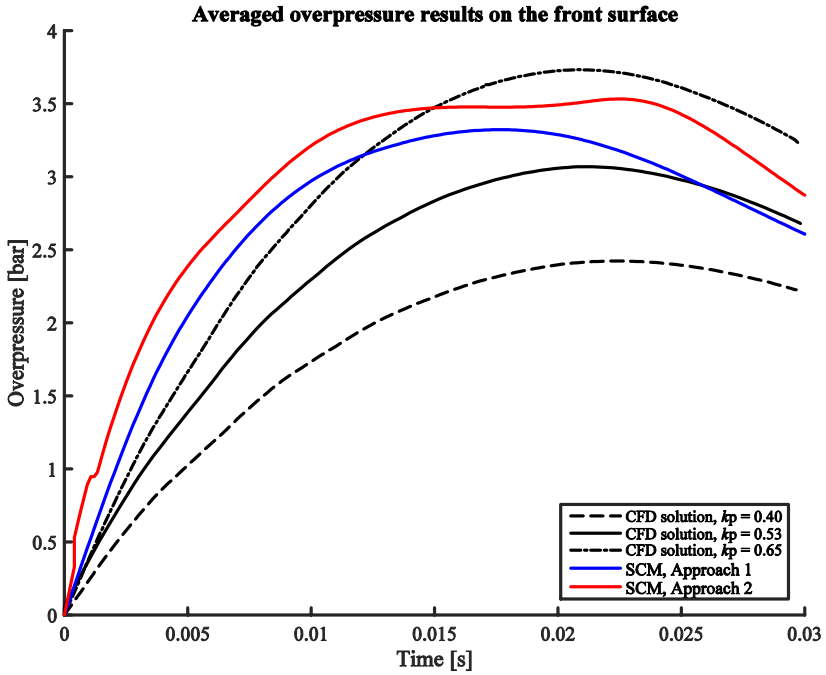

Figure 29. Averaged overpressure results on the front surface of the enclosure.

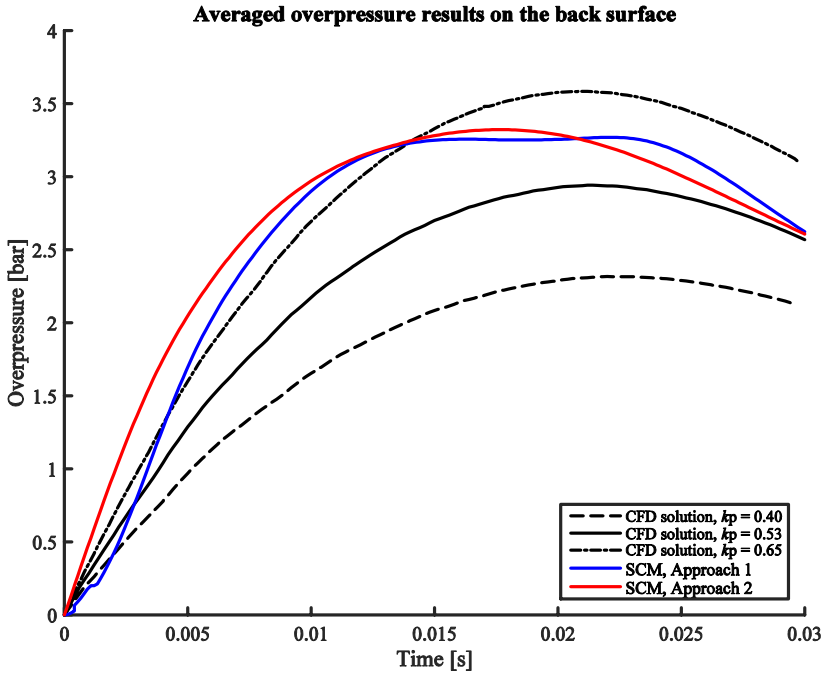

Figure 30. Averaged overpressure results on the back surface of the enclosure.

Table 8. Summarized results from the CFD simulations.

k_p	Averaged peak overpressure, Front [bar]	Front max. time [ms]	Averaged peak overpressure, Back [bar]	Back max. time [ms]
0.40	2.42	22.4	2.32	22.8
0.53	3.07	21.2	2.94	21.4
0.65	3.73	20.8	3.59	21.0

The peak overpressure averaged at the front surface of the enclosure was higher compared to the back surface for each flow case. The result can be explained by the relief disc opening, which increased the local fluid velocity at the vicinity of the opening. In turn, the pressure decreased slightly in the corresponding region. The fluid remained almost stationary in remaining parts of the enclosure, as temperature gradients inducing fluid movement were small. The phenomenon was a direct consequence of assuming that the arc energy was released homogenously in the complete fluid volume.

The averaged peak overpressures on the front and back surfaces of the enclosure are plotted as a function of the corresponding thermal transfer coefficients in Figure 31. The relationship is clearly linear.

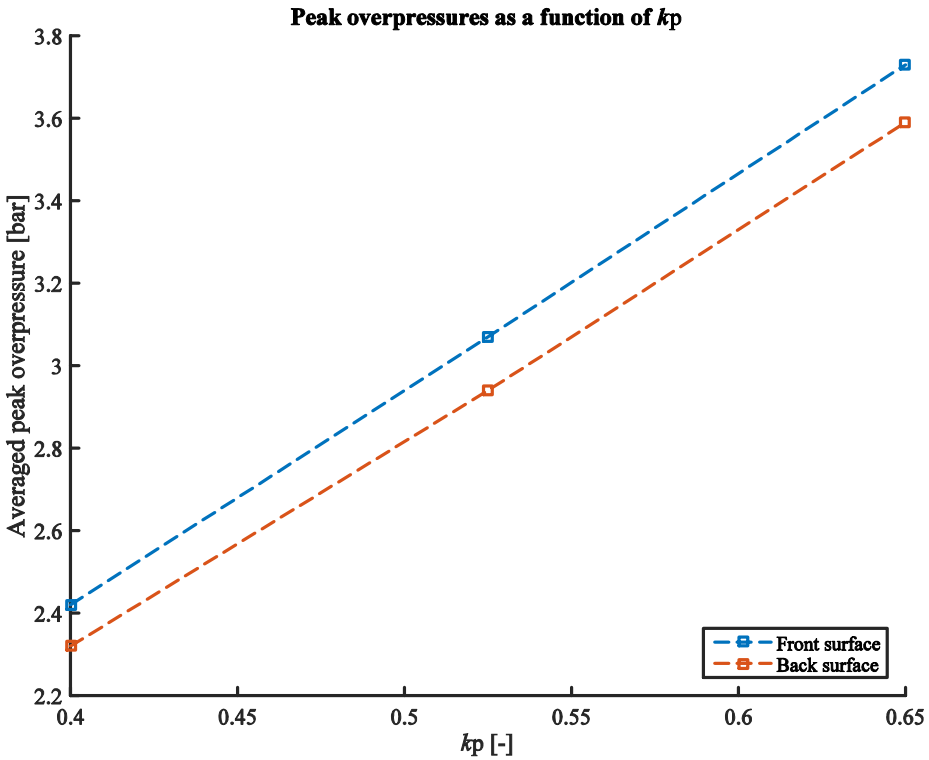

Figure 31. Averaged peak overpressures as a function of the thermal transfer coefficient.

The result can readily be explained by Eq. (2.7), applicable because the gas flow velocity was small. From the equation one can determine that the thermal transfer coefficient affects the gas temperature, and hence pressure rise in a linear fashion. The term describing the mass flow leaving the enclosure remained roughly constant between each flow case, as the maximum flow velocity at the throat of the opening was bounded, in accordance with the physics governing the flow motion.

The computational runtime for each CFD simulation was roughly 24 hours, when run on a computer cluster with 11 cores. In comparison, the computational results obtained using the SCM took less than a minute to solve.

Despite long computational times, the CFD approach should not be viewed as unnecessary. For complex fluid volumes the SCM cannot resolve the pressure loading

accurately, at least not without utilizing the concept of chaining volumes. Implementing a similar energy balance used in relation with the SCM in a CFD solver represents an interesting future research topic. For small fluid volumes often present in cramped industry level cabinets, it is uncertain how accurate spatial pressure results are resolvable even if a state of the art CFD solver would be available. The arcing volume has to be assumed large to obtain a converged solution for small fluid volumes.

Further development of the CFD approach was not in the scope of this thesis, as the focus was on understanding and modeling the structural response. Although the computational expense in this thesis seems reasonable, for larger enclosures the required effort would likely be several magnitudes longer.

7.2.4 Structural response

The enclosure was discretized with linear shell elements in order to create a computationally efficient model. Both 3 noded triangular elements and 4 noded quadrilateral elements were used, which yielded a total of 17867 elements in the model. Shear deformation was taken into account in the formulation of the shell elements. Initially all elements were assigned three integration points in their respective thickness direction, which was automatically increased to five if the von Mises stress exceeded the yield stress. Reduced integration with automatic hourglass control was used, and geometric nonlinearity was also taken into account. The resulting finite element mesh is shown in Figure 32, where the shell elements of the middle front region colored blue were offset to match the actual geometry. Two subparts were created by splitting the enclosure along the Y-plane, in order to impose a fixed boundary condition along the common bottom and side edges. The boundary condition was used to model the effects of the internal structure inside the enclosure.

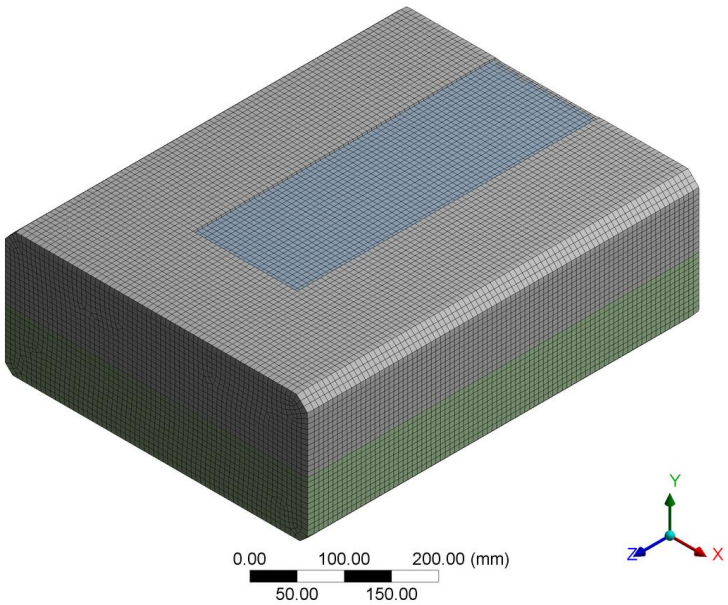

Figure 32. The resulting finite element mesh of the enclosure, where the colored regions indicate different subparts in the assembly. The corners of the back surface were fixed to the ground. More details on the structure can be found in Table 6.

A modal analysis was conducted to obtain the eigenfrequencies of the system. The results were used to determine the appropriate Rayleigh damping coefficients, and the initial time step to be used in the transient analysis. The ten first eigenfrequencies obtained from the modal analysis are shown in Table 9.

Table 9. Obtained eigenfrequencies from the modal analysis.

Eigenmode	Eigenfrequency
1	194.54
2	203.95
3	332.12
4	357.7
5	454.21
6	467.71
7	549.59
8	580.58
9	594.55
10	615.28

Determining the values for the damping coefficients accurately without experimental data is challenging. The issue is luckily not severe in relation to arc blasts, however, as damping is mainly added to ensure that unphysical excitations in the structure are not present. It is then sufficient to obtain approximate values. By comparing the damped approach to the undamped approach, it is possible to ensure that too much damping has not been added to the model. Inaccuracies relating to the damping effects are certainly insignificant compared to the uncertainty in arc power.

The Rayleigh damping coefficients were determined using Eq. (2.20) and Table 9 as

$$\alpha_{\mathrm{R}} = 92.87 \quad \& \quad \beta_{\mathrm{R}} = 1.97 \cdot 10^{-5}, \tag{2.43}$$

where $\xi_i = \xi_j = 0.05$ was used. The initial time step for the transient analysis was obtained using Eq. (2.27) as

$$\Delta t_0 = \frac{1}{20 f_{\max}} = \frac{1}{20 \cdot 615.28} = 8.13 \cdot 10^{-5}. \tag{2.44}$$

Automatic time stepping was used in relation with the pressure loads computed using the SCM. When transferring the pressure load from the CFD solver to the structural solver, the time steps were determined by the flow solution.

7.2.4.1 Structural response corresponding to the SCM, Approach 1

The pressure load corresponding to the first approach in Figure 26 was used to model the effects of the arc blast on the enclosure. Quantities of interest in the simulation were the maximum von Mises stress, equivalent plastic strain, and the deformed state of the enclosure in general. The effects or adding Rayleigh damping and the Cowper-Symonds strain rate model were also quantified.

In order to determine the mesh convergence of the solution, the averaged von Mises stresses were compared to the unaveraged von Mises stresses. Large differences generally implies that further mesh refinement is required, whereas small differences suggest that a converged solution is obtained. Stress singularities have to be taken into account, however, where the stresses will grow out of bound as the mesh is refined further. For large models where it is unfeasible to run the simulation with several meshes, the comparison of the von Mises stresses provides an excellent approach to determine the mesh convergence of the simulation.

The resulting unaveraged and averaged von Mises stresses obtained at the bottom integration points of the shell elements are shown in Figure 33. The largest stresses were obtained at the bottom section of the elements, which corresponded to the region in direct contact with the pressure load.

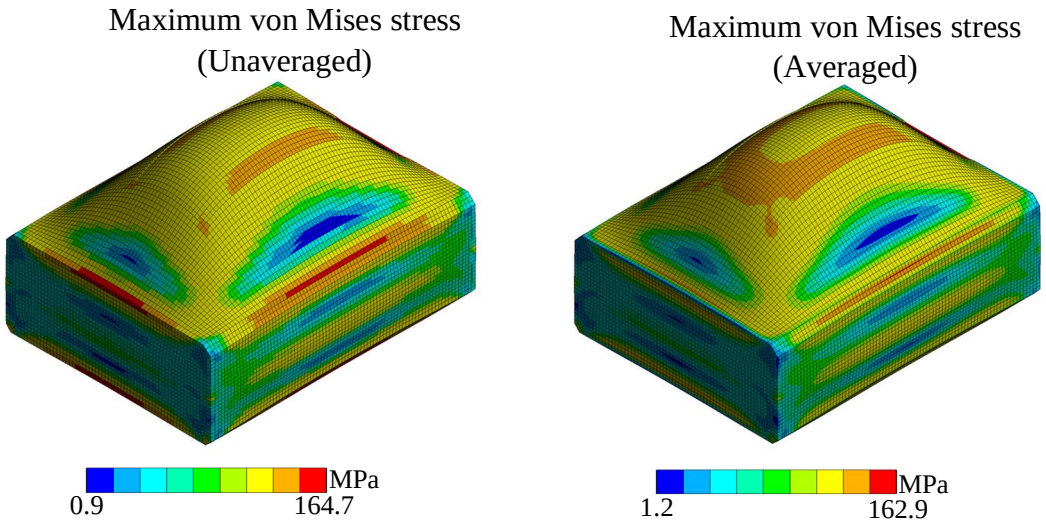

Figure 33. Comparison of averaged and unaveraged von Mises stresses in the simulation. The figure illustrates the stress distributions obtained at the bottom section points of the shell elements, in contact with the pressure load.

The unaveraged von Mises stress is always larger than the averaged von Mises stress. By inspecting the results shown in Figure 33, the difference between the maximum averaged and maximum unaveraged results was computed as roughly one percent, implying that a mesh convergent solution was obtained. Both peak values were obtained at the top edge of the front surface.

The maximum von Mises stress was obtained at t = 0.0179 s, slightly after the corresponding pressure peak at t = 0.0176 s. The result can be explained by the inertia of the enclosure, which ensured that the structure continued to deform despite the fact that the pressure had begun to decrease.

Plastic deformation was present as the computed von Mises stresses exceeded the yield stress of the material, determined in Table 6 as 110 MPa. The averaged von Mises stresses obtained at the top, middle and bottom sections of the front and back faces of the enclosure at t = 0.0179 s are shown in Figure 34.

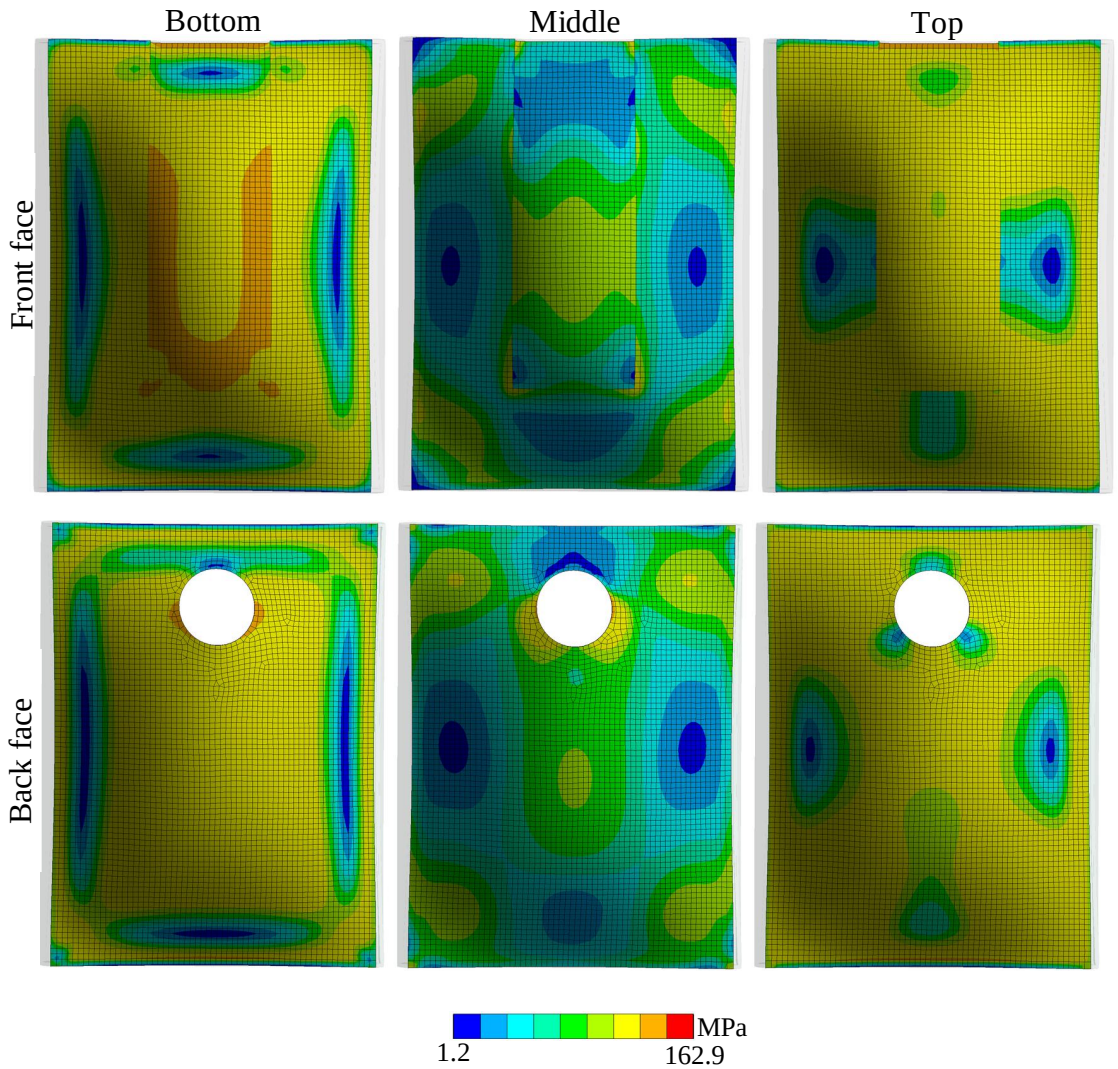

Figure 34. Averaged von Mises stress distributions at t = 0.0179 s of the front and back faces of the enclosure, obtained at the different integration points in the thickness direction of the shell elements. The bottom section was in contact with the pressure load.

The equivalent plastic strain distribution corresponding to the final time increment is shown in Figure 35, with the peak value obtained at the upper edge of the front cover of the enclosure. As discussed in Section 3.1, the equivalent plastic strain is mesh dependent, which makes it troubling for the analyst to determine the validity of the results. Since a mesh convergent solution was obtained based on comparing the averaged and unaveraged von Mises stresses, it was concluded that further mesh refinement was unnecessary. The maximum equivalent plastic strain was smaller than the fracture strain of the material provided in Table 6, implying that no material failure took place. Strictly speaking the conclusion is not foolproof, as the fracture strain dependency on stress triaxiality was not taken into account due to lack of material data. The computational result agreed well with the results obtained from the actual arc flash test, however, where no material failure was visible.

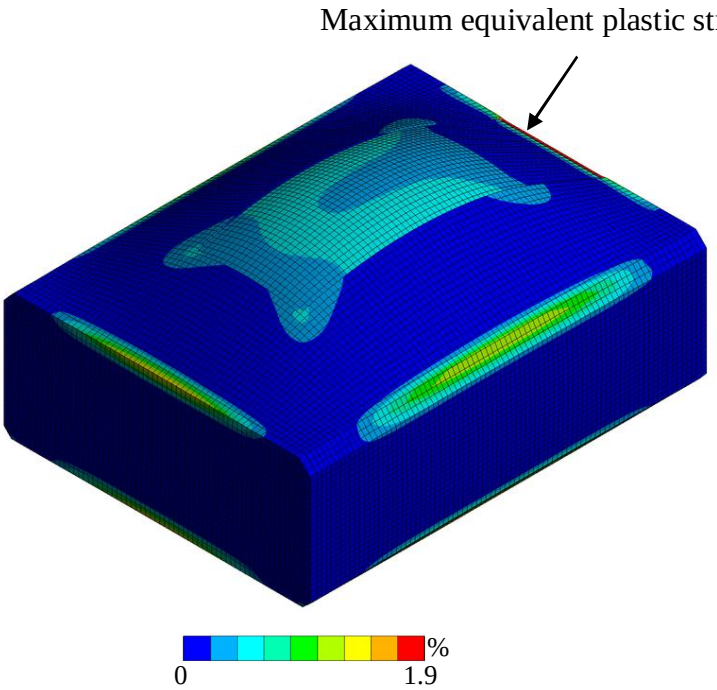

Figure 35. Equivalent plastic strain distribution corresponding to the final time increment of the analysis. The fracture strain of the material was 4 % according to Table 6, implying that structural integrity was maintained.

The final deformed shapes of the front and back faces are shown in Figure 36, where the deformation was quantified as the perpendicular nodal displacement in relation to the undeformed planar shape. The final central node displacement of the front and back faces were 10.3 mm and 7.3 mm respectively.

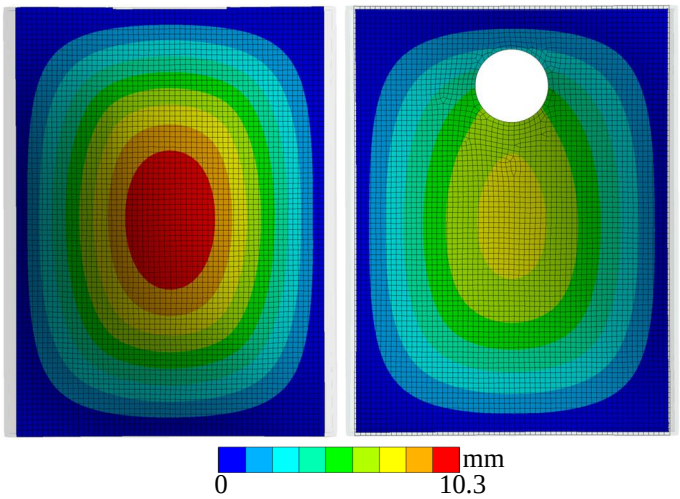

Figure 36. Final deformed shapes of front and back faces of the enclosure.

The central node displacement history for the front and back faces of the enclosure are shown in Figure 37. The addition of Rayleigh damping clearly removed unwanted vibration, without altering the final deformed state of the enclosure significantly. Hence the choice of 0.05 for the equivalent damping ratios was a reasonable choice for the specific enclosure under investigation. Large differences between the results would have implied that too much damping would have been implemented in the model. By taking

into account the strain rate effects of the material, the enclosure was found to stiffen to some extent, and resulted in smaller deformations in agreement with the results presented in Section 7.1. As the enclosure was relatively thick, the effects were small.

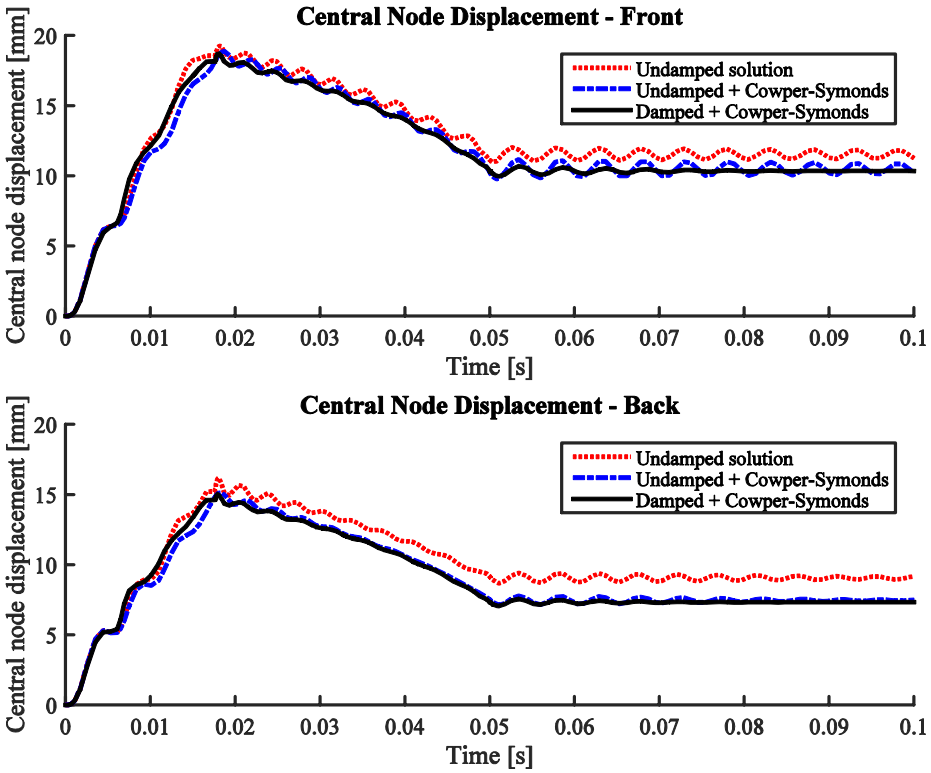

Figure 37. Central node displacements of front and back surfaces of the enclosure.

7.2.4.2 Structural response corresponding to the SCM, Approach 2

The structural response was next estimated using the second pressure distribution computed in Section 7.2.2. As the differences between the SCM approaches were small, only minor differences were expected to be present in the structural results. The results from the computation are summarized in the following sections.

The maximum unaveraged von Mises stress was observed at t = 0.0227 s, in good agreement with the results presented in Section 7.2.4.1 where the stress peak was not observed until after the corresponding pressure peak. According to Table 7 the pressure peak relating to the second approach was observed in the arc volume at t = 0.0225 s.

The maximum unaveraged von Mises stress was obtained at the same location as in relation to the first approach, and was computed as 168 MPa. The corresponding averaged von Mises stress was determined as 166.3 MPa, implying that a mesh converged solution was obtained. The von Mises stress distributions at the different sections of the shell elements obtained at the front and back surface of the enclosure are shown in Figure 38.

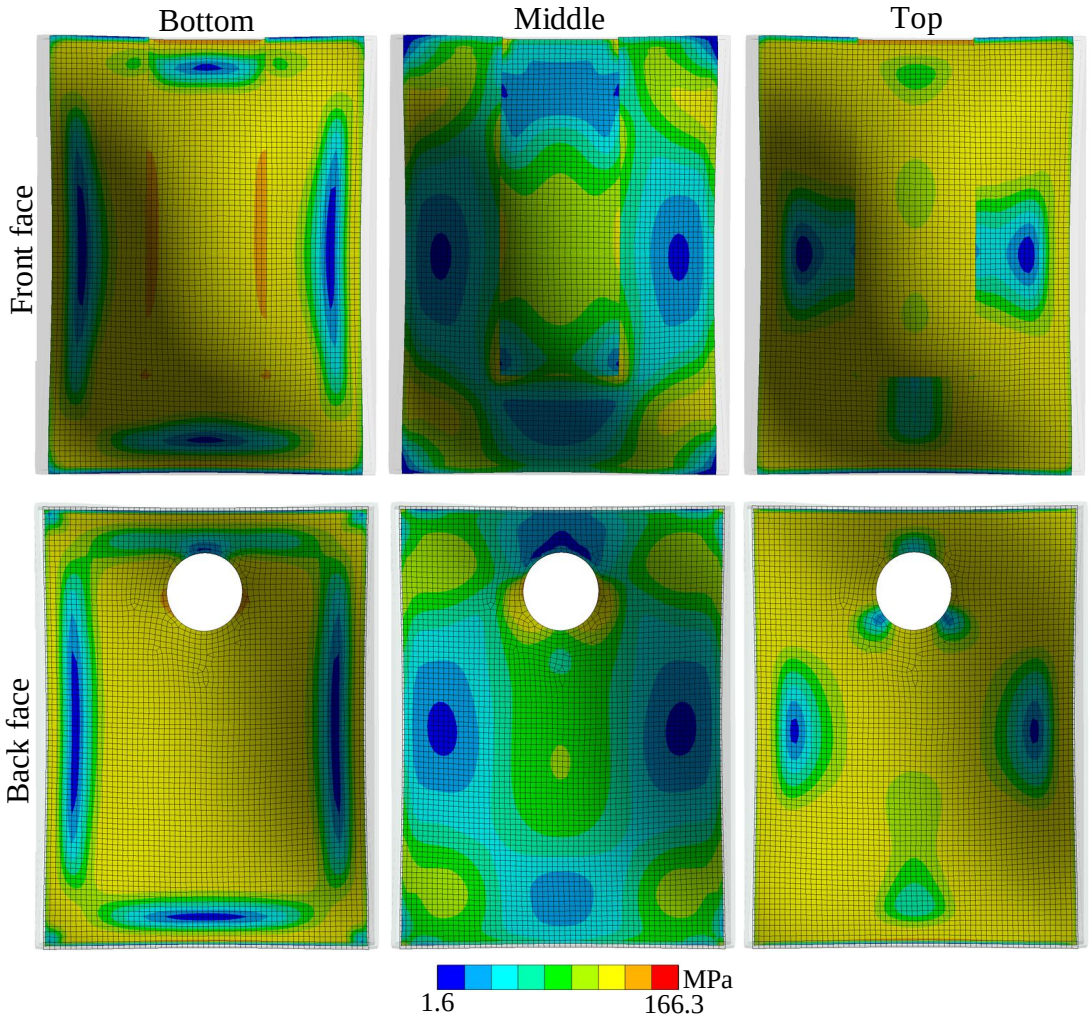

Figure 38. Averaged von Mises stress distributions at t = 0.0227 s obtained at the different sections of the front and back surfaces of the enclosure. The distributions are similar to those depicted in Figure 34.

The maximum equivalent plastic strain was determined as 2.1 %, well below the assumed fracture strain of the material determined as 4 % from Table 6.

The final central node displacement of the front and back were determined as 11.3 and 7.0 mm respectively, implying that the chaining of volumes did not affect the deformation substantially. The deformed shape was equivalent to the distribution depicted in Figure 37.

The effects of damping and the Cowper-Symonds strain rate model were finally investigated, and the results were practically equivalent to those portrayed in Figure 37.

Figure 39 illustrates the difference in central node displacement time histories between the SCM approaches for the full solutions which included damping and strain rate effects.

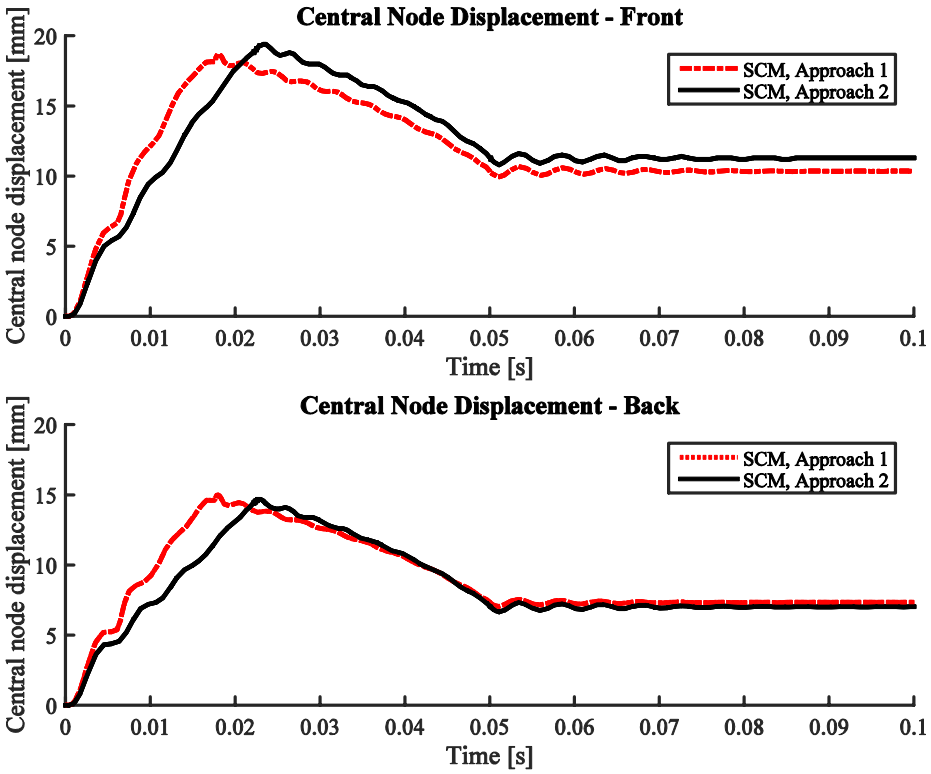

Figure 39. Comparison of central node displacements between SCM approaches used in the thesis, with damping and Cowper-Symonds strain rate sensitivity taken into account.

7.2.4.3 Structural response corresponding to the CFD pressure load

The structural response was finally computed using the loads obtained from the CFD simulations, which were transferred to the structural solver in ANSYS® (2015a) using the ACT toolkit.

The maximum averaged and unaveraged von Mises stresses corresponding to each flow case are summarized in Table 10.

Table 10. Maximum unaveraged von Mises stresses and their corresponding averaged results in MPa.

[MPa]	$k_{p,min.}$	$k_{p,ave.}$	$k_{p,max.}$
Max. unaveraged	139.6	157.8	173.4
Max. averaged	139.3	156.2	171.3
Difference	0.2 %	1 %	1.2 %

The small differences depicted in Table 10 illustrate that sufficient confidence in the results was achieved. As the peak pressure increased, the relative difference between the averaged and unaveraged von Mises stresses increased. The resulting maximum averaged von Mises stresses are illustrated in Figure 40 for each separate simulation.

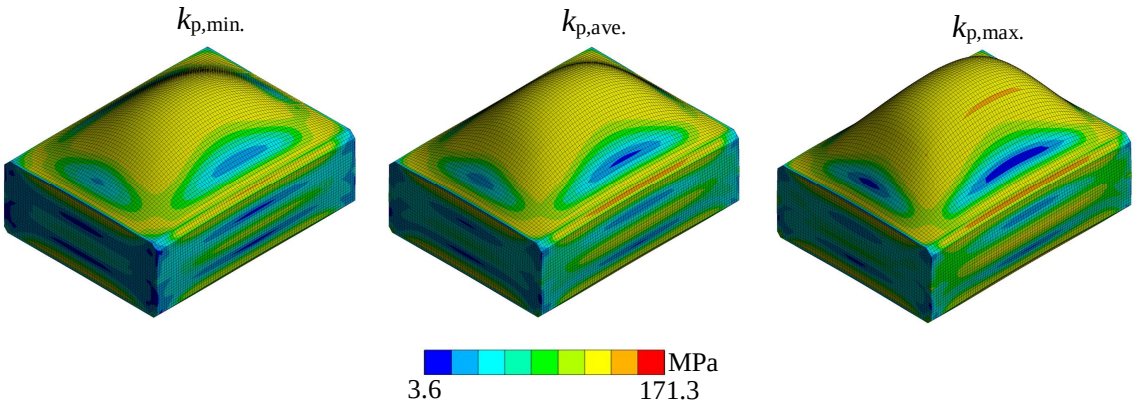

Figure 40. Averaged von Mises stresses corresponding to the peak value for each separate simulation.

The peak equivalent plastic strains are summarized in Table 11, and illustrated in Figure 41.

Table 11. Obtained peak equivalent plastic strains from the simulations in percent.

[%]	$k_{p,min.}$	$k_{p,ave.}$	$k_{p,max.}$
Max. equivalent plastic strain	0.89 %	1.56 %	2.23 %

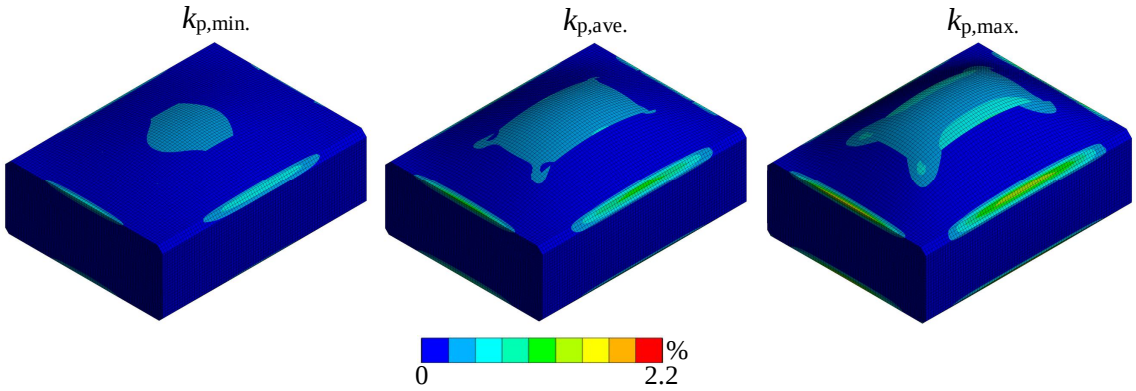

Figure 41. Equivalent plastic strain distributions obtained at the last time step of each structural simulation.

The final central node displacements at the front and back surfaces of the enclosure are summarized in Table 12. The deformed shapes were equivalent to those obtained in relation with the SCM.

Table 12. Final central node displacements of the front and back surfaces.

[mm]	$k_{p,min.}$	$k_{p,ave.}$	$k_{p,max.}$
Front central node displacement	2.5	5.5	8.3
Back central node displacement	4.7	8.9	12.2

7.2.5 Sensitivity analysis of structural simulation

A thorough sensitivity analysis was conducted to gain a better understanding of the system response. The sensitivity analysis was performed using the second approach in relation to the SCM, as it a good compromise between accuracy and computational effort. The sensitivity analysis was conducted by altering the value of each input parameter in turn by ±10 %, and recording the corresponding system response. The results are and summarized in Table 13, and illustrated in Figure 42 and Figure 43.

Table 13. Results from sensitivity analysis. The most sensitive input parameters are colored, and the initial reference case is shown at the top of the table.

		Max. central node displacement front [mm]	Final central node displacement front [mm]	Max. central node displacement back [mm]	Final central node displacement back [mm]	Max. averaged von Mises [MPa]	Equivalent plastic strain [%]
Initial case	N/A	19.4	11.3	14.7	7.0	166.3	2.1
Enclosure thickness t	+10%	21.4	13.5	16.8	9.3	173.1	2.5
	-10%	17.6	9.1	12.7	5.0	160.4	1.8
Density ρ	+10%	19.4	11.3	14.6	7.0	166.6	2.1
	-10%	19.3	11.2	14.7	7.0	165.7	2.1
Young's modulus E	+10%	19.8	10.9	15.1	6.7	165.5	2.1
	-10%	19.0	11.6	14.3	7.2	166.8	2.1
Poisson's ratio v	+10%	19.4	11.2	14.7	6.9	166.1	2.1
	-10%	19.4	11.3	14.7	7.1	166.5	2.1
Yield stress	+10%	20.5	13.4	15.6	8.8	158.2	2.4
	-10%	18.6	9.3	13.9	5.5	174.6	1.8
Tangent modulus	+10%	19.4	11.4	14.7	7.1	164.2	2.2
	-10%	19.3	11.2	14.6	6.9	168.2	2.1
C	+10%	19.4	11.2	14.7	7.0	166.5	2.1
	-10%	19.4	11.3	14.7	7.0	165.9	2.1
P	+10%	19.5	11.6	14.8	7.3	164.0	2.1
	-10%	19.2	10.9	14.5	6.7	168.5	2.1
Overpressure p_{max}	+10%	18.0	9.4	13.4	5.6	159.8	1.8
	-10%	20.8	13.0	15.9	8.5	172.4	2.5

Figure 42 and Figure 43 depict the relative sensitivities of the final central node displacement estimates, which were of particular interest as the structural simulation was to be validated by comparing the measured deformations with computed predictions. Parameters for which a bar appears to be missing in the figures implies that the computed variation was rounded to zero to the accuracy of one decimal point.

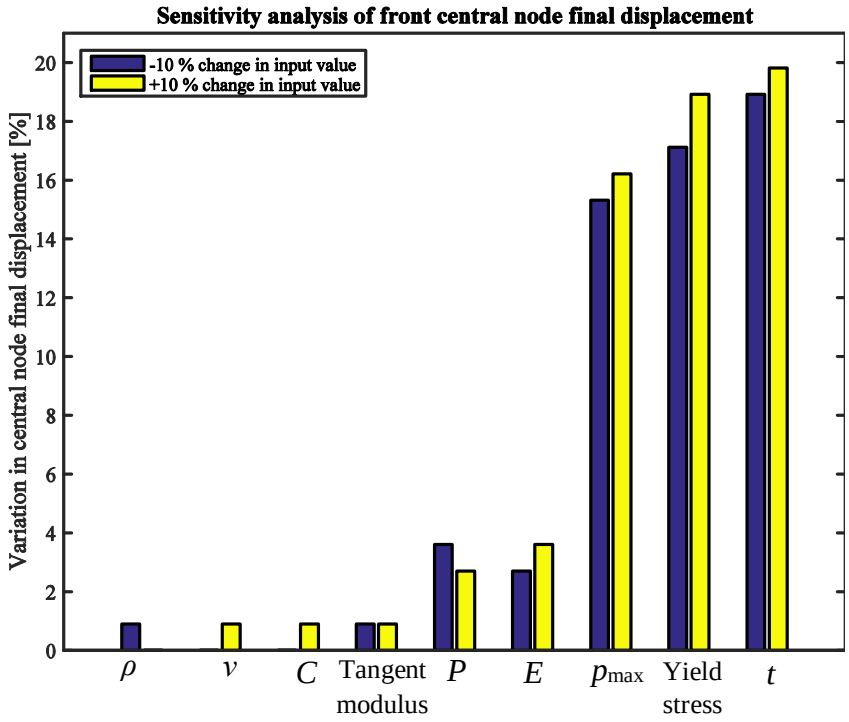

Figure 42. Sensitivity analysis results of the front central node final displacement.

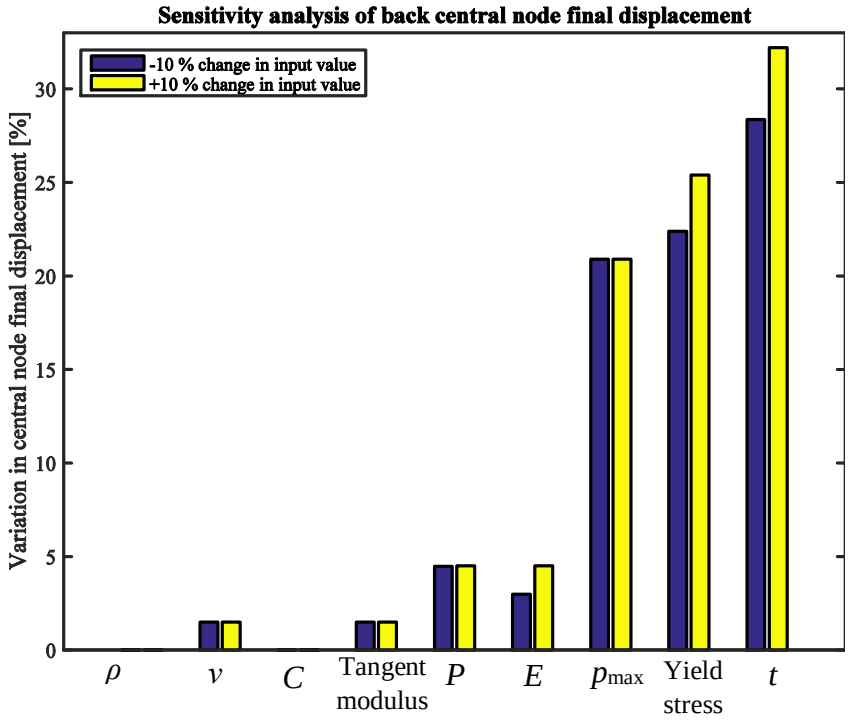

Figure 43. Sensitivity analysis results of the back central node final displacement.

Based on the results in Table 13, Figure 42 and Figure 43, the input parameters can clearly be distinguished into two sensitivity groups. The structural response is substantially more sensitive to variation in the maximum overpressure, yield stress and the thickness of the enclosure. Only little of the model sensitivity can be attributed to the other input parameters.

Distinguishing between absolute and relative sensitivity is important, however. From Figure 43 it is possible to determine that an increase of 10 % in the enclosure thickness causes the final central node displacement to decrease by 30 %. Although seemingly large, on an absolute scale the difference is only 2 mm. The maximum relative sensitivity in Figure 43Figure 43 is larger compared to Figure 42, as the absolute central node displacement on the back was smaller than on the front.

Figure 44 illustrates how the absolute variation in the maximum equivalent plastic strain remains small despite the high relative sensitivity. The concept of relative sensitivity is valuable when comparing the sensitivities between different input variables, however.

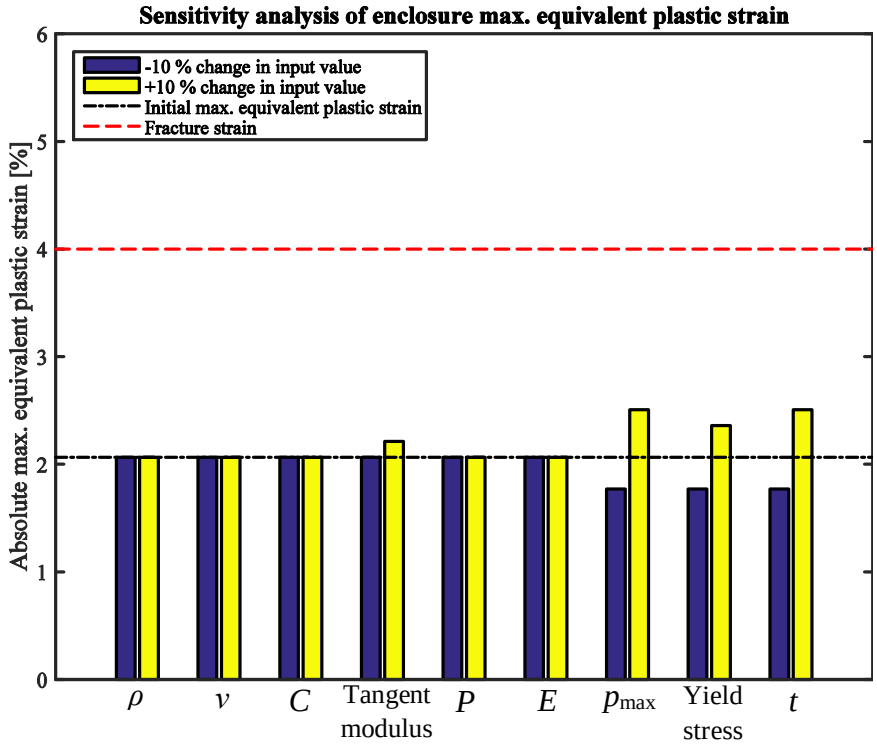

Figure 44. The absolute sensitivity of the maximum equivalent plastic strain remains small despite the large relative sensitivity.

The results in Figure 44 provides a valuable foundation for the stochastic analysis discussed further in Section 6.1.

The exact yield stress remained unknown as the enclosure used in the arc flash test was a prototype. By taking into account the bounding values for the upper and lower yield stress for the material used as presented by Hydro (2015), the central node final displacements could only be determined to an accuracy of ± 6 mm.

7.2.6 Comparison with experimental results

The deformations of the enclosure used in the arc flash test were measured using a TESA Micro Hite 3D-474 coordinate-measuring machine, which had a reported measurement accuracy of ± 10 µm. The permanent deformations measured from the front surface are shown in Figure 45 and Figure 46, and the deformations measured from the back surface are shown in Figure 47 and Figure 48.

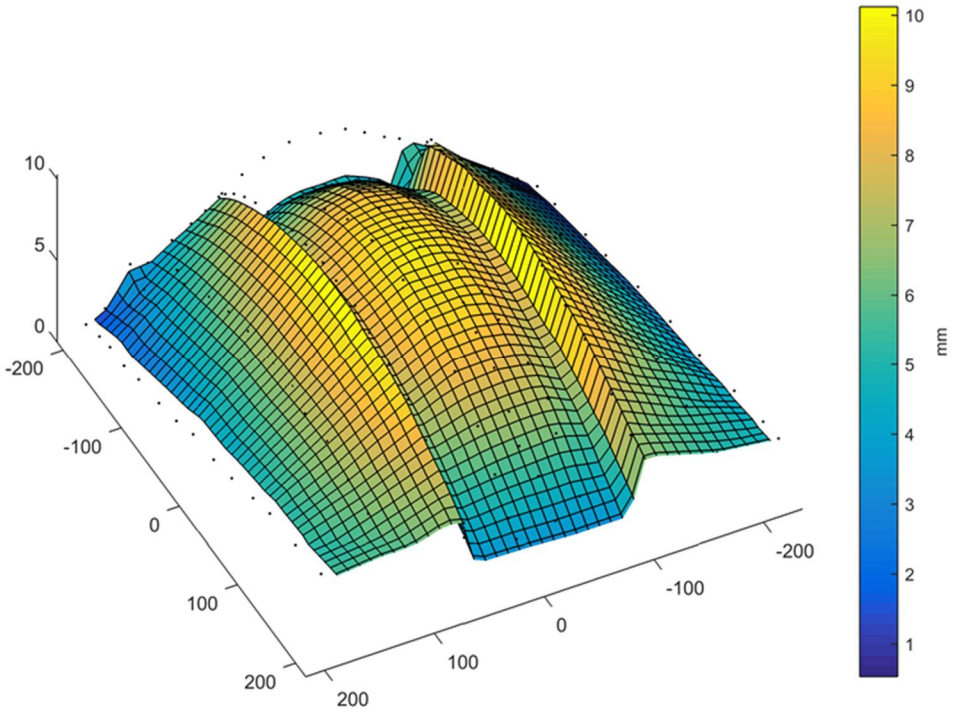

Figure 45. Isometric view of measured deformations on the front surface.

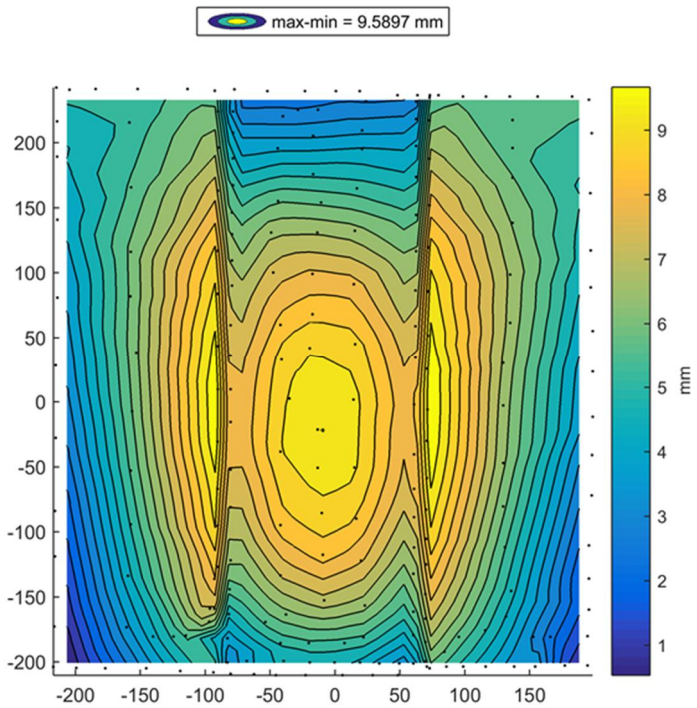

Figure 46. Top view of measured deformations on the front surface.

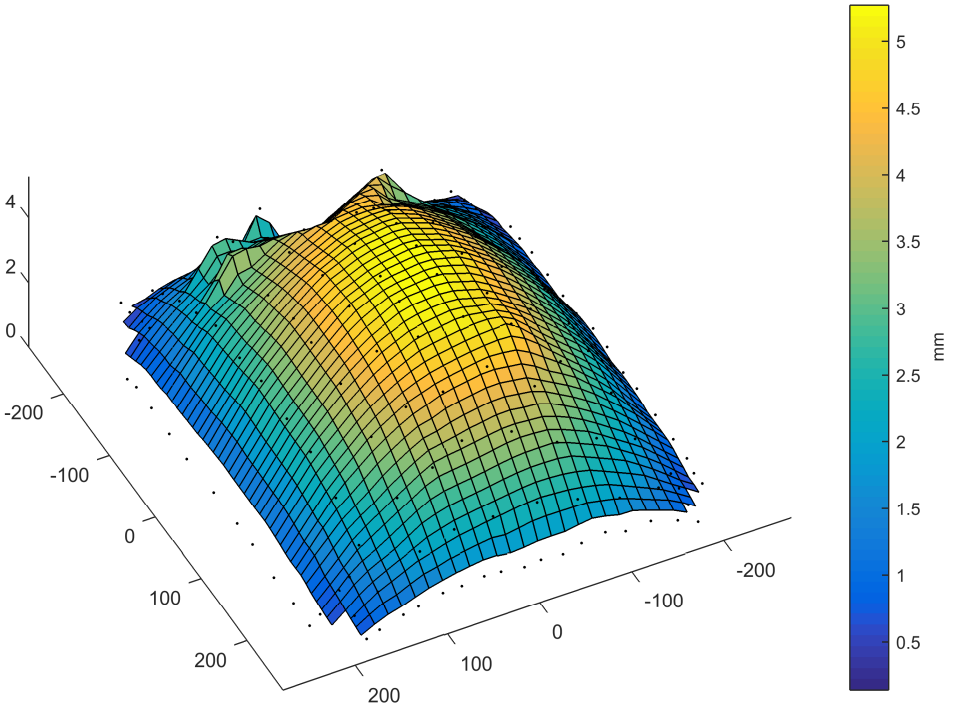

Figure 47. Isometric view of measured deformations on the back surface.

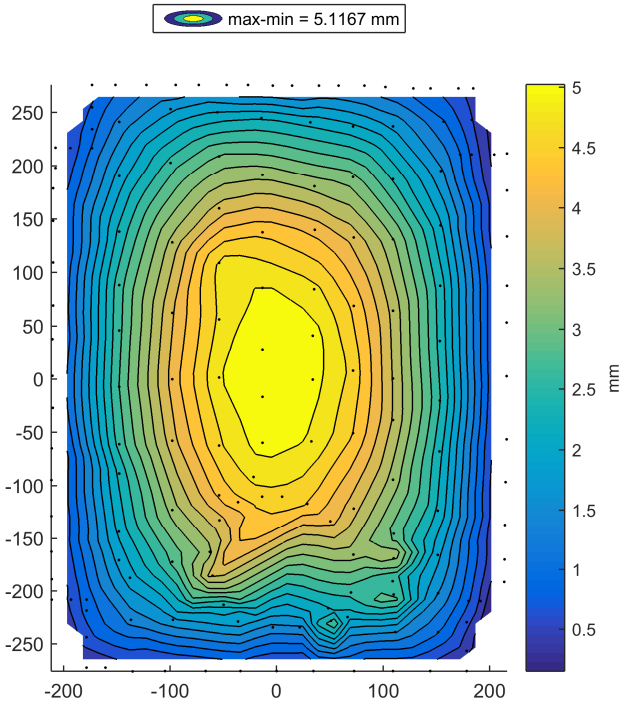

Figure 48. Top view of measured deformations on the back surface.

The computed deformations and the corresponding measured deformations are summarized in Table 14.

Table 14. Summarized results of the computed and measured deformations in mm. Uncertainty in the measured deformations was ± 10 µm.

[mm]	SCM, Approach 1	SCM, Approach 2	CFD $k_{p,min.}$	CFD $k_{p,ave.}$	CFD $k_{p,max.}$	Measured
Front	10.3 ± 6	11.3 ± 6	2.5 ± 6	8.9 ± 6	12.2 ± 6	9.6
Back	7.3 ± 6	7.0 ± 6	4.7 ± 6	5.5 ± 6	8.3 ± 6	5.1

Based on the results summarized in Table 14, the computed deformations agree with the measured deformations. All simulations predicted the deformation to be larger on the front surface compared to the back surface. The result can be explained by the different chamfer dimensions on the front edges compared to the back, and the slight offset of the middle front surface. By neglecting the offset the final central node displacement decreased by roughly one millimeter.

The predicted displacements differ from the measured results at most by roughly 30 %. As the absolute deformations are small, it makes little sense to compare the results in terms of relative values, however. The general shape of the deformed surfaces match well with the computations, with the central area of the front and back surface experiencing the largest displacement. The small local displacement peaks visible on the back surface shown in Figure 47 were most likely caused by measurement error.

Although reasonable confidence in the computational methods was gained, further validation and verification is recommended as only the final deformations were measured. Determining the displacement time history with an accelerometer or high-speed video camera would immediately provide information on the accuracy of the results depicted in Figure 37 and Figure 39. Measuring the overpressure inside the enclosure should also be considered vital, as it would confirm the accuracy of the approaches used to estimate the blast load. Conducting dynamic pressure measurements accurately are generally expensive and extremely challenging, however.

For the arc flash investigated in this thesis, it is possible that the pressure load was estimated wrong, but a possibly wrong estimate for the yield stress canceled the effect to produce seemingly accurate results. Determining the yield stress with less uncertainty would also improve the reliability of the results. Furthermore, the initial deformations of the enclosure should have been measured to quantify the relative final displacements more accurately.

When validating the computational approach in the future, larger deformations should be desired. For small absolute deformations the relative error introduced by simplifications in the computational model are more severe.

Finally, seemingly accurate results were obtained as the arc power was known. In actual arc flash accidents it can be impossible to determine the arc power beforehand.

7.2.7 Implications of a probabilistic analysis

Variation in the arc voltage induces uncertainty in the pressure load as discussed in Section 6, which the structural response is sensitive to. Furthermore, variation in both the yield stress and thickness play some role when determining the structural response according to the discussion in Section 7.2.5, although highly dependent on the manufacturing tolerances. For electrical switchgears the variation can be large, however, as the enclosure itself is generally not considered a vital part of the product. Considerable savings can then be attained by allowing for larger tolerances.

In accordance with Section 6, input variables which carry both uncertainty and large sensitivity are good candidates for the stochastic analysis. In this thesis, the enclosure thickness, arc pressure, and yield stress were assumed to follow probabilistic distributions instead of being assigned deterministic values based on the results in Section 6 and Section 7.2.5.

ANSYS® (2015d, p. 47) recommends the assumption of a uniform probability density function in relation to geometric tolerances. Hence, the enclosure thickness was assumed to follow a uniform probability density function with bounding values of 5.7 mm and 6.3 mm respectively, indicating a manufacturing tolerance of 0.6 mm.

The yield stress was assumed to follow a normal distribution as advised by ANSYS® (2015d, p. 47). The expected value of 110 MPa was determined in accordance with Table 6, and the corresponding standard deviation was chosen as 30 MPa.

The blast load was estimated using the second approach in relation to the SCM, which provided a normally distributed response where 95 % of the peak overpressures lied within 20 % of the expected values.

The resulting histograms from 39 individual samples are shown in Figure 49. As the emphasis was on illustrating the process of adapting the stochastic analysis principle, the number of samples was small.

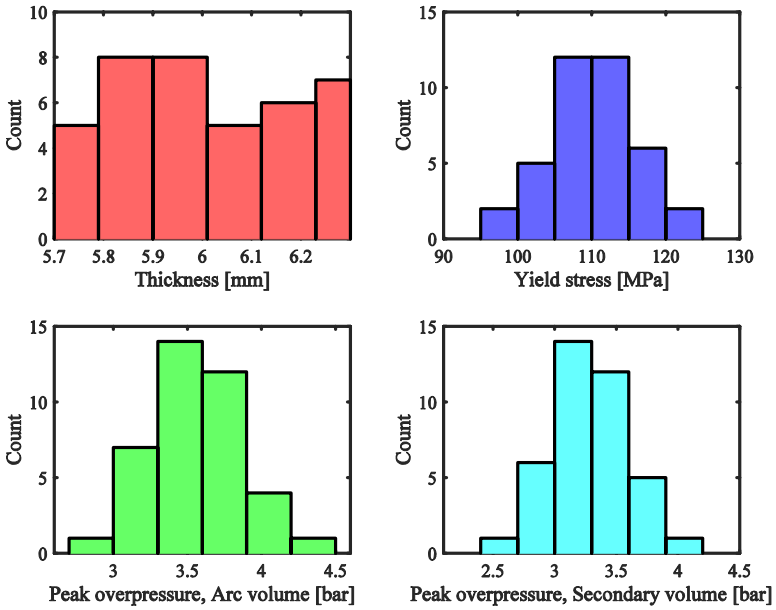

Figure 49. Obtained histograms from the sampling process, where the Latin Hypercube –sampling technique was used.

The principle of Monte Carlo simulation described in Section 6.1 was next applied, by repeating the structural FEM simulation for a total of 39 times. The maximum equivalent plastic strain, and the final central node displacements at the front and back surfaces of the enclosure were recorded for each simulation. The resulting histogram for the maximum equivalent plastic strain and the front and back central node final displacement estimates are shown in Figure 50 and Figure 51.

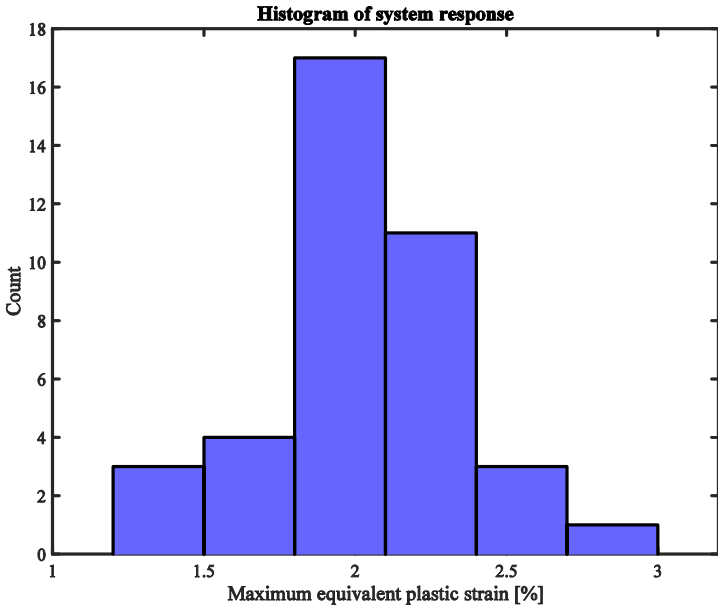

Figure 50. Histogram of maximum equivalent plastic strain obtained from the FEM simulations.

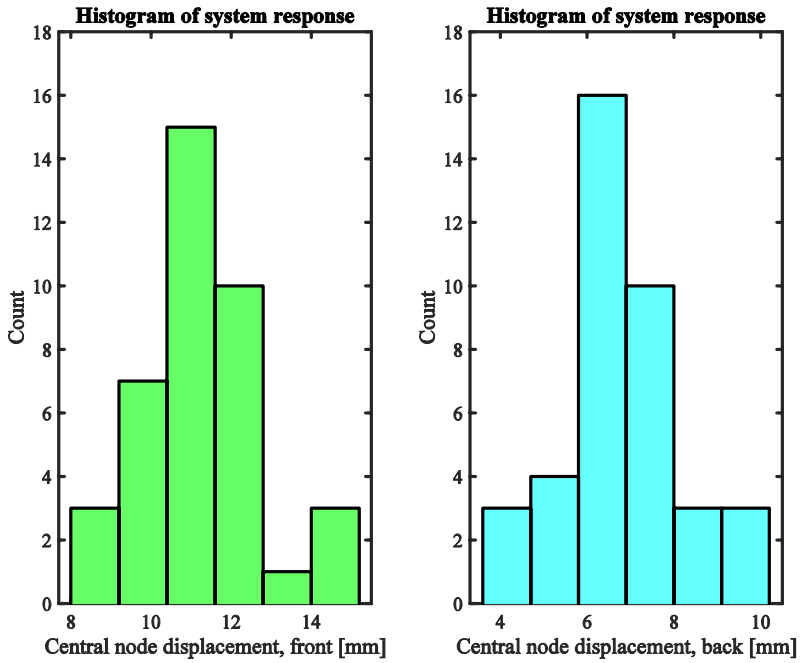

Figure 51. Histogram of the final central node displacements of the front and back surface, acquired from the FEM simulations.

A normal distribution was fitted to the histogram in Figure 50 based on the computed mean and standard deviation, determined as μ_{ep} = 2.05 % and σ_{ep} = 0.32 % respectively. By normalizing the resulting distribution with its corresponding area, the resulting probability density function was obtained. The fracture strain of the material was estimated to follow a normal distribution with a mean μ_f = 4 % and standard deviation σ_f = 0.20 %. The result from the stochastic analysis is shown in Figure 52.

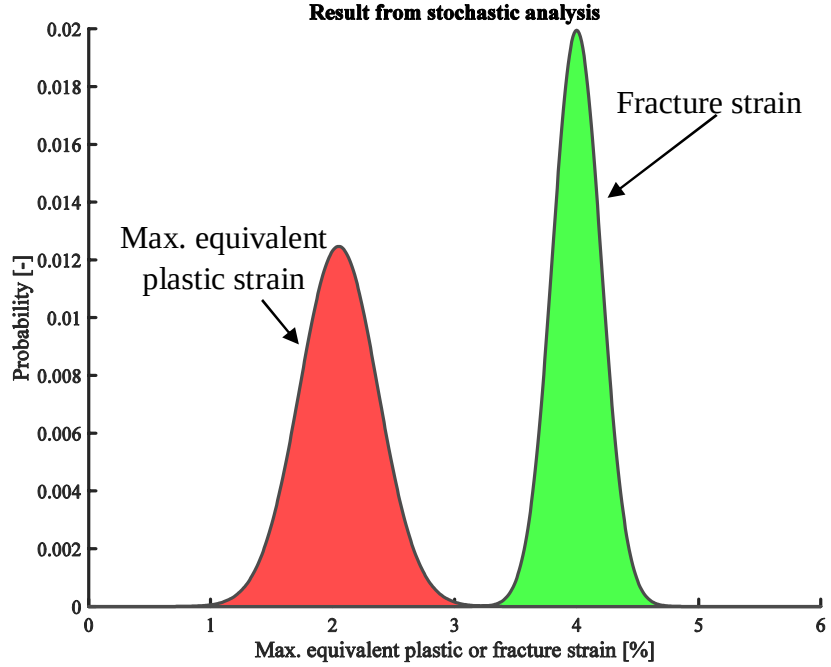

Figure 52. Result from the stochastic analysis with corresponding normalized probability density functions.

The corresponding probability of failure was computed using Eq. (2.40) and the known distributions as

$$p_{\mathrm{F}} = \int_0^{\infty} \left[1 - \frac{1}{2} \left(1 + \operatorname{erf} \left\{ \frac{x - \mu_{\mathrm{ep}}}{\sigma_{\mathrm{ep}} \sqrt{2}} \right\} \right) \right] \cdot \frac{1}{\sigma_{\mathrm{f}} \sqrt{2\pi}} e^{-\frac{(x-\mu_{\mathrm{f}})^2}{2\sigma_{\mathrm{f}}^2}} \, \mathrm{d}x = 1.04 \cdot 10^{-7}, \qquad (2.45)$$

which implies that roughly 1 enclosure in 9.6 million experiencing an arc flash shortcut will undertake material failure as a result of the blast load. The low probability is reasonable as the enclosure used in the arc flash test only suffered from small deformations.

In reality, the enclosure would likely experience a much larger failure rate due to the phenomenon of arc burn through discussed in Section 1.3, unless properly designed. Chu (1982) estimated that the probability of personnel injury due to the burn-through phenomenon to be between $1.5 – 3.3 \cdot 10^{-5}$ per each SF_6 insulated substation each year.
The stochastic dimensioning principle offers a delicate approach for taking into account the uncertainty, although its downside is that several analyses have to be performed in order to obtain reliable results. A fundamental requirement is therefore that the computational tool has to be sufficiently light for use in practical applications. The SCM offers a robust approach for obtaining the pressure load, thus suitable for the stochastic analysis. On the other hand, the structural model might be complex, which limits the application of the approach to some extent. By performing the stochastic analysis on only a part of the structural model the issue can be circumvented, however. For instance, the stochastic analysis could be performed on the relief disc to gain understanding what the probability is for the disc to open in a particular arc flash event.

In this thesis the main goal was to illustrate the process of adapting a stochastic dimensioning principle, hence the number of samples were small. In reality, substantially more samples might be required to obtain sufficiently reliable results. Estimating the number of samples beforehand can be difficult. In practice, the number of samples might be determined in accordance with the available computational time. For a good discussion relating to sample size requirements for Monte Carlo – simulations, the reader is encouraged to familiarize with Matala (2008). Finally, a good measure for the reliability of the results is to investigate how the probability of failure varies as a function of iteration count. For the enclosure investigated, the corresponding relation is shown in Figure 53. As can be seen, the probability of failure is appearing to converge as the number of analyses increases. The absolute difference in probability of failure are small despite the large relative variation.

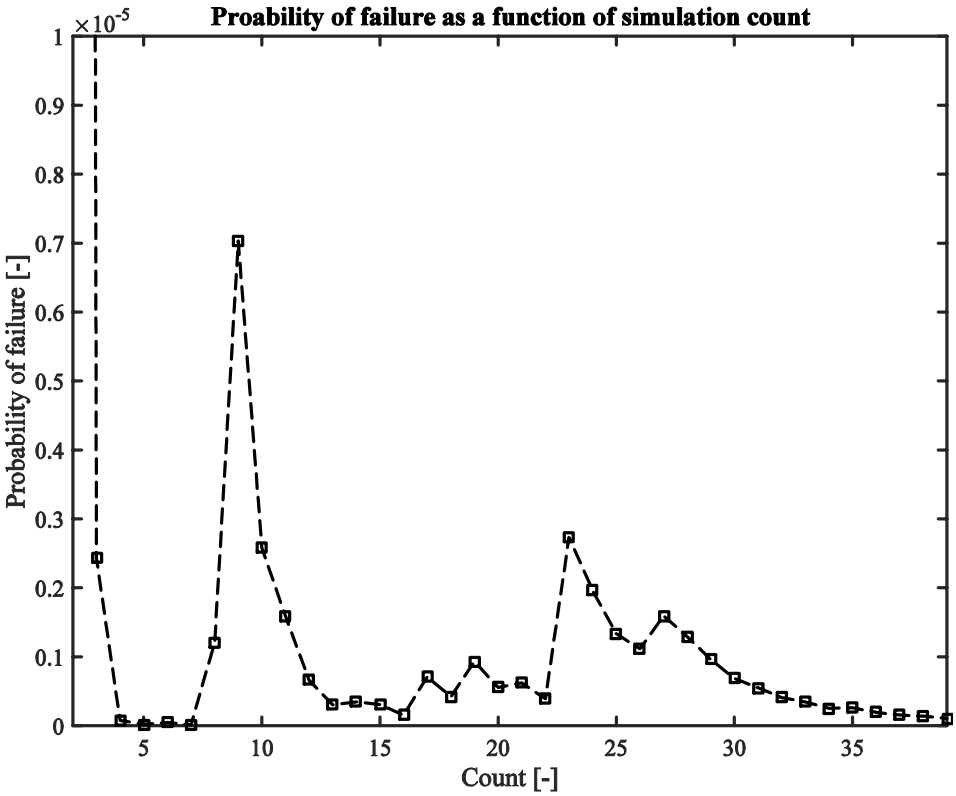

Figure 53. Probability of failure as a function of FEM simulation count.

8 Discussion and conlusions

The goal of this thesis was to develop a sensible approach for analyzing the structural response in an arc flash event, as no thorough investigation on the matter was documented in the literature. Previous research has mostly been focused on investigating the physics behind arc generation and the resulting pressure buildup. Developing and documenting the correct simulation methodology in relation to the structural response was considered important, as it would aid in reducing the number expensive arc flash tests in the future.

Two established methods for estimating the pressure load caused by the arc flash were first presented, based on the results from a thorough literary review. The first approach yields the averaged pressure rise in a system of subvolumes with little computational effort, and is denoted as the standard calculation method in this thesis. Although unable to predict the effects of pressure waves, the method is valuable especially during the initial dimensioning process of enclosures when design changes are frequent.

The second approach used to estimate the pressure load is based on computational fluid dynamics. Although able to capture the effects of pressure waves, the method is computationally expensive. Obtaining converged solutions is also demanding as the fluid temperature typically rises above several thousands of degrees kelvin. The approach is therefore best suited in the final stages of the structural dimensioning process, when only insignificant modifications in the design are expected.

Understanding the limitations of the two approaches was found to be important when taking into account the structural response. Ensuring that fluid does not escape the enclosure from unexpected locations is vital for both tools to be applicable, as coupled fluid-structure simulations are too time consuming for practical work. In fact, molten pieces of electrode material and fire protruding through small openings in the structure can often pose a more serious risk for nearby personnel compared to material failure in the enclosure. Considerable caution and vigilance is therefore necessary when analyzing the applicability of the results. In many cases, it can be challenging to determine if fluid escapes the enclosure at ill-favored locations. It is therefore proposed that enclosures should be completely sealed in directions where individuals might be present during operating conditions.

Dimensioning the cross-sectional area of the relief disc was found to be a straightforward task. The appropriate relief disc size is highly dependent on the expected overpressure and enclosure type, however, which makes it difficult to present general guidelines. Verifying that the relief disc functions correctly at the specified opening pressure is more challenging as described in Section 3.1. Fortunately, the computational tools presented in this thesis are capable of addressing the issue.

Aspects governing the structural response were next thoroughly considered, after which the implications of the methods were explored. A considerable amount of effort was put into quantifying the consequences of strain rate effects on the material behavior.The numerical deformations of a realistic enclosure were compared to measured values from

an analogous arc flash test to establish the accuracy of the methods. Finally, a novel dimensioning approach based on the probability of material failure was introduced, as the uncertainty relating to arc flash events is large due to the typical stochastic nature of the arc voltage.

Two strain rate models were extensively compared, namely the Cowper-Symonds model and the Huh-Kang model. The latter model provided a better agreement with experimental results as determined by Schwer (2007). In the strain rate region of interest, the Huh-Kang model predicted the stiffening effect of the material to be more severe compared to the Cowper-Symonds model.

For large structures where the enclosure thickness remains small, the strain rate effects were found to be considerable. By taking into account the effects on material behavior, the displacements were found to reduce at most by roughly 10 %. Simultaneously the probability of failure was reduced as the maximum equivalent plastic strain in the structure was lowered at most by roughly 1 %. Neglecting the strain rate effects therefore produces more conservative estimates. Strain rate parameters often remain unknown for enclosure materials of interest, as it is difficult to motivate the need to conduct tensile tests at elevated strain rates for electric switchgears and enclosures. Typically, the enclosure material itself is not considered a vital part of the product. On the other hand, variation in the strain rate parameters only had a limited influence on the structural response. Approximate values for the strain rate parameters therefore produce sufficiently accurate results. For thin enclosures where contact is used to describe the behavior between plates and fasteners, the structural simulation may fail to complete due to excessive deformations. By taking into account the strain rate effects the deformations decrease, which aids in addressing the issue.

The structural response of a realistic enclosure was next investigated, and the predicted deformations were compared to measurements obtained from an enclosure used in a corresponding experimental arc flash test. A thorough sensitivity analysis was also conducted to gain insight into the robustness of the structural simulation. Both approaches used to estimate the resulting pressure load were examined. The benefit of the standard calculation method was that an enthalpy based approach was available for the fraction of arc energy transferred to the surrounding gas, which made the use of a thermal transfer coefficient redundant. The reliability of the results were hence improved considerably. A similar approach was not available when estimating the pressure load using computational fluid dynamics.

The standard calculation method performed well compared to the approach based on computational fluid dynamics if the computational time was taken into account, as both methods resulted in similar pressure distributions as shown in Figure 29 and Figure 30. By applying the principle of dividing the fluid volume in a chain of subvolumes as presented in Section 2.2.3, more accurate pressure results were obtained without significantly increasing the computational time. For large complex fluid volumes which do not contain noticeable bottlenecks, the principle of chaining subvolumes is not applicable, however, which makes pressure estimates obtained using the standard

calculation method less reliable. According to Uzelac et al. (2014, p. 24) the cross-sectional area of the opening should not exceed 10 % of the corresponding surface area for the computational approach to be valid. In some cases then, computational fluid dynamics offers the only realistic approach to estimate the resulting blast loading.

As presented in Section 7.2.6, confidence in the computational methods was obtained by comparing numerical predictions for the structural deformations with measurements. Both the deformed shape of the enclosure and the numerical displacements were in agreement with the measurements. The absolute difference between the measured displacements and numerical estimates was in the order of a few millimeters. On an absolute scale the measured permanent deformations remained below 10 millimeters. The implication is then that the structural response in an arc flash event can be reproduced to a sufficient degree numerically, at least for small enclosures. Although the structure under investigation was simple, the methods presented in this thesis are immediately applicable to more complicated enclosures.

By implementing the computational approach for estimating the structural response, designs can be tested virtually before expensive arc flash tests are conducted. A convincing portfolio of sample cases which have been thoroughly validated and verified, might make expensive experimental arc flash tests redundant in the future.

Further testing where additional parameters are measured are recommended to boost the promising results obtained thus far. A thorough set of experiments where arc pressures are measured along with parameters quantifying the structural response should be considered important in the future. The use of high-speed video cameras, accelerometers and strain gauges would provide great insight into the accuracy of time varying simulation parameters, such as nodal displacement time histories.

A thorough sensitivity analysis was next conducted to gain further insight into the structural response. Understanding how large the variation in the system response was when each input variable was varied in turn, helped in quantifying the robustness and accuracy of the simulation. Based on the investigation, small variations in the resulting peak overpressure, enclosure thickness, and material yield stress resulted in the largest variation in the system response. For instance, a variation of ± 10 % in the enclosure thickness resulted the permanent displacements to vary at most by roughly ± 30 %. In relation to an equivalent variation in the peak overpressure and material yield stress, the permanent displacements varied at most by roughly ± 20 % and ± 25 %, respectively. The large relative variation in the response can mostly be attributed to the small permanent deformations of the enclosure. On an absolute scale the resulting variation was only a few millimeters.

The large uncertainty present in arc flash events makes efforts at describing the pressure load with high accuracy unnecessary, to some extent. Typically the variation in arc power is large between analogous events, as the arc voltage is often found to vary stochastically. Enclosures are often dimensioned by attempting to describe a worst-case arc flash accident, which produces a conservative estimate for the pressure load. For many cases

such a procedure is not feasible, as it would require an unrealistically robust enclosure design.

In this thesis an alternative dimensioning principle was presented, by addressing the uncertainty relating to the arc power appropriately as described in Section 6. Dimensioning a structure by requiring the probability of first material failure to be below some predefined threshold value is not only intuitive to understand, but also results in enclosures to not be dimensioned unnecessarily robust. The downside of the principle is that multiple simulations have to be run, which in practice requires the pressure load to be estimated using the standard calculation method. For many enclosures, this is not a serious limitation, however.

References

ABAQUS®. 2015a. Abaqus FEA Software, 6.14. Dassault Systèmes. Providence, Rhode Island, The United States.

ABAQUS®. 2015b. Abaqus Theory Guide, 6.14. Dassault Systèmes. Providence, Rhode Island, The United States.

Adams, V. 2008. A Designer's Guide to Simulation with Finite Element Analysis. 1st ed. Hamilton, The United Kingdom: NAFEMS.

Aldred, J. 1972. Manual of Sound Recording. 2nd ed. London, The United Kingdom: Fountain Press.

Anantavanich, K. 2010. Calculation of Pressure Rise in Electrical Installations due to Internal Arcs Considering SF_6-Air Mixtures and Arc Energy Absorbers. Ph.D. Thesis, RWTH Aachen University.

Ang, A.H.S and Tang, W.H. 1984. Probability Concepts in Engineering Planning and Design, Vol. 2: Decision, Risk and Reliability. 1st ed. Hoboken, New Jersey, The United States: John Wiley & Sons.

ANSYS®. 2013. Transient Analysis, Full Method, ANSYS Mechanical Linear and Nonlinear Dynamics. ANSYS Inc. Canonsburg, Pennsylvania, The United States.

ANSYS®. 2014. ANSYS Application Customization Toolkit, Transient Fluid-Structure Interaction, Release 15.0. ANSYS Inc. Canonsburg, Pennsylvania, The United States.

ANSYS®. 2015a. ANSYS, Release 16.0. ANSYS Inc. Canonsburg, Pennsylvania, The United States.

ANSYS®. 2015b. ANSYS Mechanical APDL Theory Reference, Release 16.0. ANSYS Inc. Canonsburg, Pennsylvania, The United States.

ANSYS®. 2015c. ANSYS Mechanical APDL Structural Analysis Guide Release 16.0. ANSYS Inc. Canonsburg, Pennsylvania, The United States.

ANSYS®. 2015d. ANSYS Mechanical APDL Advanced Analysis Guide Release 16.0. ANSYS Inc. Canonsburg, Pennsylvania, The United States.

Asanuma, G. & Onichi, T. and Isozaki, M. 2014. Numerical Simulation of Pressure Rising with Internal Arc Fault for a Medium Voltage Metal Clad Switchgear. Proceedings of the 20th International Conference on Gas Discharges and their Applications. Orléans, 6-11 July, 2014.

Babrauskas, V. 2010. Electric Arc Explosions. Proceedings of the 12th International Fire Science & Engineering Conference Interflam. Nottingham, 5-7 July, 2010. London: Interscience Communications Ltd, pp. 1283-1296.

Becerra, M. and Ostrowski, J. 2014. Internal Arc Simulation Platform, ABB CRC, Switzerland.

Besnard, C. 2009. Internal Arc Simulation in MV/LV Substations. Proceedings of the 20th International Conference on Electricity Distribution. Prague, 8-11 July, 2009.

Bodner, S.R. and Symonds, P.S. 1962. Experimental and Theoretical Investigation of the Plastic Deformation of Cantilever Beams Subjected to Impulsive Loading. Journal of Applied Mechanics, Vol. 29, No. 4, pp. 719-728. doi: 10.1115/1.3640660

Boyce, B.L. & Crenshaw, T.B. and Dilmore, M.F. 2007. The Strain-Rate Sensitivity of High-Strength High-Toughness Steels. Albuquerque: Sandia National Laboratories.

Bugelli, E.B. and Driemeier, L. 2010. Failure Models Evaluations on Structures Under Low Speed Crash – Experiments and Simulations. Proceedings of the IMPLAST 2010 Conference. Providence, 12-14 October, 2010.

Chen, J. & Young, B. and Uy, B. 2006. Behaviour of High Strength Structural Steel at Elevated Temperatures. Journal of Structural Engineering. Vol. 132, No. 12, pp. 1948-1854.

Chen, C.J. and Jaw, S.Y. 1998. Fundamentals of Turbulence Modelling. 1st ed. New York, New York, The United States: Taylor & Francis.

Cook, R.D. & Malkus, D.S. & Plesha, M.E. and Witt, R.J. 2001. Concepts and Applications of Finite Element Analysis. 4th ed. Hoboken, New Jersey, The United States: Wiley.

Cowper, G.R. and Symonds, P.S. 1958. Strain Hardening and Strain Rate Effects in the Impact Loading of Cantilever Beams. Brown University, Applied Mathematics Report No. 28.

Craig, R.R. and Kurdila, J. 2006. Fundamentals of Structural Dynamics. 2nd ed. Hoboken, New Jersey, The United States: John Wiley & Sons.

Chu, F. & Ford, G. and Law, C. 1982. Estimation of Burn-Through Probability in SF6 Insulated Substations. Power Apparatus and Systems, IEEE Transactions, PAS-101, pp. 1391-1399.

Dasbach, A. 1990. Calculation of Pressure Waves in Substation Buildings due to Arcing Faults. Power Delivery, IEEE Transactions, Vol. 5, No. 4, pp. 1760-1765.

Dimitrienko, Y.I. 2011. Nonlinear Continuum Mechanics and Large Inelastic Deformations. 1st ed. Houten, Utrecht, The Netherlands: Springer.

Drouet, M.G. and Nadeau, F. 1979. Pressure Waves Due to Arcing Faults in a Substation. Power Apparatus and Systems, IEEE Transactions, Vol. PAS-98, No. 5, pp. 1632-1635.

Franz, A. 2005. Störlichtbögen und ihre Auswirkungen. Bulletin Electrosuisse, No. 21, pp. 17-18.

Fletcher, C.A.J. 1991. Computational Techniques for Fluid Dynamics, Vol. 1: Fundamental and General Techniques. 2nd ed. New York, New York, United States: Springer.

Friberg, G. 1998. Berechnungsverfahren zur Bestimmung der Druckbelastung in elektrischen Anlagen im Störlichtbogenfall. Ph.D. Thesis, RWTH Aachen University.

Health & Safety Executive. 1999. The Behaviour of Carbon Steels at High Strain rates and Strain Limits. Berkshire: Bomel Limited.

Hencky, H.Z. 1924. Zur Theorie Plasticher Deformationen und der Hierdurch im Material Hervorgerufenen Nachspannungen. Zeitschrift für Angewandte Mathematik und Mechanik, Vol. 4, p. 323.

Huh, H. Kang, W.J. 2002. Crash-Worthiness Assessment of Thin-Walled Structures with the High-Strength Steel Sheet. International Journal of Vehicle Design, Vol. 30, No. 1/2, pp. 1-21. doi: 10.1504/IJVD.2002.002022.

Hydro. 2015. Technical Data Sheet AlSi10Mg(a). [online]. Available at: http://www.hydro.com/upload/Documents/Products/AlSi10Mga.pdf. [Accessed 9.7.2015]

Iwata, M. & Anantavanich, K. and Pietsch, G.J. 2008. Influence of Arc Current on Fraction Kp of Electric Arc Energy Leading to Pressure Rise in a Closed Container. Proceedings of the 17th International Conference on Gas Discharges and Their Applications. Cardiff, 7-12 September, 2008. Cardiff: IEEE, pp. 189-192.

Johnson, G.R. and Cook, W.H. 1983. A Constitutive Model and Data for Metals Subjected to Large Strains, High Strain Rates and High Temperatures. Proceedings of the 7th International Symposium on Ballistics. Hague, 19-21 April, 1983.

Johnson, G.R. and Cook, W.H. 1985. Fracture Characteristics of Three metals Subjected to Various Strains, Strain Rates, Temperatures and pressures. Engineering Fracture Mechanics. Vol. 21, No. 1, pp. 31-48.

Lampinen, M.J. 2010. Termodynamiikan Perusteet. 5th ed. Helsinki, Finland: Hakapaino Oy,

Lee, R.H. 1987. Pressures Developed by Arcs. Industry Applications, IEEE Transactions, Vol. IA-23, No. 4, pp. 760-763.

Li, F. and Xingwen, D. 2010. Mesh-dependence of Material with Softening Behaviour. Chinese Journal of Aeronautics, Vol. 23, No. 1, pp. 46-53.

Ljustina, G. & Fagerström, M. and Larsson, R. 2014. Rate Sensitive Continuum Damage Models and Mesh Dependence in Finite Element Analyses. The Scientific World Journal, Vol. 2014, Article ID 260571. doi: 10.1155/2014/260571.

McKay, M.D. & Beckman, R.J. and Conover, W.J. 1979. A Comparison of Three Methods for Selecting Values of Input Variables in the Analysis of Output from a Computer Code. Technometrics, Vol. 21, No. 2, pp. 239-245. doi: 10.2307/1268522.

Malvern, L.E. 1969. Introduction to the Mechanics of a Continuous Medium. 1st ed. Englewood Cliffs, New Jersey, The United States: Prentice-Hall.

Mansilla, A. & Regidor, A. & Garcia, D. and Negro, A. 2000. Dynamic Tensile Testing for Determining the Stress-Strain Curve at Different Strain Rate. Journal de Physique IV, Vol. 10, No. 9, pp. 695-700. doi: 10.1051/jp4:20009116.

Matala, A. 2008. Sample Size Requirements for Monte Carlo – simulations using Latin Hypercube Sampling. Technical Report. Helsinki University of Technology.

Melot, J. & Trépanier, J.Y. & Camarero, R. and Petro, E. 2011. Comparison of Two Models for Raditive Heat Transfer in High Temperature Thermal Plasmas. Modelling and Simulation in Engineering. doi:10.1155/2011/285108.

Murakami, S. 2012. Continuum Damage Mechanics. 1st ed. Houten, Utrecht, The Netherlands: Springer.

Nettleton, M.A. 1976. Explosions due to faults in electrical equipment. Electrical Review, pp. 116-119.

Oberthür, J. 1986. Dimensionierung von Druckentlastung in SF6-isolierten Anlagen bei Auftreten von inneren Störlichtbögen. Elektrie, pp. 92-94.

Oh, C.S. & Kim, N.H. & Kim, Y.J. & Baek, J.H. & Kim, Y.P. and Kim, W.S. 2011. A Finite Element Ductile Failure Simulation Method Using Stress-Modified Fracture Strain Model. Engineering Fracture Mechanics, Vol. 78, No. 1, pp. 124-137. doi: 10.1016/j.engfracmech.2010.10.004.

Ottosen, N and Petersson, H. 1992. Introduction to the Finite Element Method. 1st ed. Essex, The United Kingdom: Prentice-Hall.

Parnes, R. 2001. Solid Mechanics in Engineering. 1st ed. West Sussex, The United Kingdom: John Wiley & Sons Ltd.

Patankar, S.V. 1980. Numerical Heat Transfer and Fluid Flow. 1st ed. Hemisphere, New York, United States: Hemisphere Publishing.

Rice, J.R. 1975. Continuum Mechanics and Thermodynamics of Plasticity in Relation to Microscale Deformation Mechanisms, Constitutive Equations in Thermodynamics. 1st ed. Cambridge, Massachusetts, The United States: MIT Press.

Santaoja, K. 2012. Rasitusopin Käsikirja Lujuusopin Lukijoille. 2nd ed. Helsinki, Finland: Picaset Oy.

Schwer, L. 2007. Optional Strain-Rate Forms for the Johnson-Cook Constitutive Model and the Role of the Parameters $\dot{\varepsilon}_0$. Proceedings of the 6th European LS-DYNA Users' Conference. Gothenburgh, 29-30 May, 2007.

Singh, S. and Summer, R. 2011, Simplified Internal Arc-Structural Simulation. Proceedings of the 21st International Conference and Exhibition on Electricity Distribution. Frankfurt 6-9 June, 2011.

Sundararajan, C. 1995. Probabilistic Structural Mechanics Handbook: Theory and Industrial Applications. 1st ed. New York, New York, The United States: Springer.

Uzelac, N. et al. 2011. Tools for the Simulation of Effects of the Internal Arc in Transmission and Distribution Switchgear, Rev. 11.1. CIGRE, International Council on Large Electric Systems.

Walter, P.L. 2004. Air-Blast and the Science of Dynamic Pressure Measurements

White, F. 2005. Viscous Fluid Flow. 2nd ed. New York, New York, United States: McGraw-Hill.

Wilson, W.R. 1955. High-Current Arc Erosion of Electric Contact Materials. Power Apparatus and Systems, Part III. Transactions of the American Institute of Electrical Engineers, Vol. 74, No. 3, pp. 657-664.

Wu, H. & Xiaohui, L. & Stade, D. and Schau, H. 2005. Arc Fault Model for Low-Voltage AC Systems. IEEE Transactions on Power Delivery, Vol. 20, No. 2, pp. 1204-1205. doi: 10.1109/TPWRD.2005.844231.

Zhang, X. & Pietsch, G. & Zhang, J. and Gockenbach, E. 2006. Fundamental Investigation on the Thermal Transfer Coefficient due to Arc Faults. Plasma Science, IEEE Transactions, Vol. 34, No. 3, pp. 1038-1045.

Øyvang, T. & Fjeld, E. & Rondeel, W. and Hagen, S.T. 2011, High Current Arc Erosion on Copper Electrodes in Air. Proceedings of the 57th Holm Conference on Electrical Contacts. Minneapolis 11-14 September, 2011 Minneapolis: IEEE, pp. 1-6.